

# ABSTRACT

Title of Document: TAILORING PROPERTIES AND FUNCTIONALITIES OF  
NANOSTRUCTURES THROUGH COMPOSITIONS,  
COMPONENTS AND MORPHOLOGIES

Lin Weng, Ph.D., 2013

Directed By: Professor Min Ouyang, Department of Physics

The field of nanoscience and nanotechnology has made significant progresses over the last thirty years. Sophisticated nanostructures with tunable properties for novel physics and applications have been successfully fabricated, characterized and underwent practical test. In this thesis, I will focus on our recent efforts to develop new strategies to manipulate the properties of nanostructures. Particularly, three questions have been answered from our perspective, based on the nanomaterials synthesized: (1) How does the composition affect a novel nanostructure? We started from single-molecule precursors to reach nanostructures whose bulk counterparts only exist under extreme conditions.  $\text{Fe}_3\text{S}$  and  $\text{Fe}_3\text{S}_2$  are used as examples to demonstrate this synthetic strategy. Their potential magnetic properties have been measured, which may lead to interesting findings in astronomy and materials science. (2) How to achieve modularity control at nanoscale by a general bottom-up approach? Starting with reviewing the current status of

this field, our recent experimental progresses towards delicate modularity control are presented by abundant novel heteronanostructures. An interesting catalytic mechanism of these nanostructures has also been verified, which involves the interaction between phonons, photons, plasmons, and excitons. (3) What can the morphology difference tell us about the inside of nanostructures? By comparing a series of data from three types of CdSe/CdS core-shell structures, a conclusion has been reached on the CdS growth mechanism on CdSe under different conditions, which also may lead to a solution to the asymmetry problem in the synthesis of CdSe/CdS nanorods. Finally this thesis is concluded by a summary and future outlook.

TAILORING PROPERTIES AND FUNCTIONALITIES  
OF NANOSTRUCTURES THROUGH  
COMPOSITIONS, COMPONENTS AND  
MORPHOLOGIES

By

Lin Weng

Dissertation submitted to the Faculty of the Graduate School of the  
University of Maryland, College Park, in partial fulfillment  
of the requirements for the degree of  
Doctor of Philosophy  
2013

Advisory Committee:  
Professor Min Ouyang, Chair  
Professor John Cumings  
Professor Lourdes G. Salamanca-Riba  
Professor Oded Rabin  
Professor Janice Reutt-Robey

© Copyright by  
Lin Weng  
2013

Dedication

To

My Parents Tao Weng and Aiqin Lin

## Acknowledgements

I would like to thank my advisor, Professor Min Ouyang who guided me to achieve the successful completion of my thesis. He has been fully supportive of my research and has given me a lot of freedom, even when I seemed to be not as aggressive as he expected. The discussions with him that sometimes even escalated into intense debates will be great helpful for my future research career. His enthusiasm for science has always been invigorating me, and I feel that my success is directly linked to his guidance.

I would also like to thank Professor Michael A. Coplan, director of Chemical Physics Program. He has been always available and willing to help throughout my graduate study at UMCP.

I feel grateful that Dr. Yun Tang helped me at the beginning of my research. He taught me everything I need to know to maintain a lab and conduct experiments. I would also like to thank Dr. Jiatao Zhang, who is the most knowledgeable person on the colloidal chemistry I even know. I would also thank other members in Ouyang Group: Mr. Kwan Lee and Ms Huizhi Bai for their help whenever I needed. I would also like to thank Lady Five to amuse and comfort me in the past five years.

# Table of Contents

Dedication .....	ii
Acknowledgements.....	iii
Table of Contents.....	iv
List of Tables .....	vi
List of Figures .....	vii
Chapter I: Introduction .....	1
1. The background of Nanoscience and Nanotechnology.....	1
2. Nanomaterials in Our Research .....	5
2.1 Semiconductor Nanomaterials.....	5
2.2 Metal Nanomaterials .....	8
2.3 Magnetic Nanomaterials .....	10
3. Parameters to Tune the Properties of Nanomaterials .....	13
3.1 Size .....	13
3.2 Morphology.....	19
3.3 Component.....	23
3.4 Composition.....	25
4. General Characterization of Nanoparticles.....	28
4.1 Transmission Electron Microscopy and Its Associated Facilities.....	28
4.2 Ultraviolet-visible Spectroscopy.....	29
4.3 Fluorescence Spectroscopy .....	30
5. Summary .....	31
Chapter II: Unusual Compositions of Stoichiometric Iron-Rich Iron Sulfide NPs $\text{Fe}_3\text{S}$ and $\text{Fe}_3\text{S}_2$ : Synthesis and Magnetic Property.....	32
1. Introduction .....	32
2. Experimental Techniques.....	37
2.1 Synthesis of Single-Source Molecular Precursors.....	37
2.2 Synthesis of the Fe/S NPs.....	38
3. Result and Discussion.....	39
4. Conclusion.....	44
Chapter III: Modularity Control in Synthesis and Properties of Hybrid Nanooligomers Based on a General Approach.....	46
1. Existing Schemes.....	46
1.1 Processes based on Toposelective Surface Modification.....	46
1.2 Processes Based on Controlled Phase Separation.....	49
1.3 Processes Based on Controlled Surface Nucleation.....	51
2. Novel Chemical Synthetic Approach of Bottom-up Method.....	53
3. Experiment Section.....	55
3.1 Chemicals.....	55
3.2 Experimental methods.....	57
3.2.1 Synthesis of Au nanoparticles with various sizes.....	57

3.2.2 Synthesis of Au-Ag core-shell nanoparticles with various ratio of Au/Ag.....	58
3.2.3 Synthesis of Au-Ag <sub>2</sub> Se and Au-Ag <sub>2</sub> S heterodimers.....	58
3.2.4 Synthesis of Au-CdSe, Au-CdS, Au-PbSe and Au-ZnS heterodimers.....	59
3.2.5 Synthesis of FePt-CdSe heterodimers.....	60
3.2.6 Synthesis of Pt nanocubes.....	61
3.2.7 Synthesis of Pt-Ag dimers with controlled spatial arrangement.....	62
3.2.8 Synthesis of Pt-Ag <sub>2</sub> S, Pt-PbS, Pt-ZnS and Pt-CdS heterodimers.....	63
3.2.9 Synthesis of Pt-Ag <sub>2</sub> Se heterodimers.....	65
3.2.10 Synthesis of Pt-Au <sub>x</sub> Ag <sub>y</sub> -CdSe nanooligomers.....	65
3.2.11 Synthesis of Pt-CdSe-CdS and Pt-HgSe-CdS nanooligomers.....	68
4. Result.....	71
4.1 Hybrid Dimer.....	71
4.1.1 Au-CdSe Nanodimer.....	71
4.1.2 Pt-CdS Nanodimer.....	75
4.2 Hybrid Trimer and More Modules Incorporated in a Single NP.....	77
5. Properties and Measurements.....	82
6. Nanoscale Photocatalysis.....	85
6.1 Introduction.....	85
6.2 Photocatalysis Measurement.....	88
6.3 Theoretical Modeling of Energetic Hot Plasmonic Electrons Driven Photocatalysis by the Pt-Au <sub>x</sub> Ag <sub>y</sub> -CdSe Nanooligomers.....	89
6.4 Result and Conclusion.....	96
7. Conclusion.....	102
Chapter IV: Morphology Modulations on CdSe Seeded CdS Nanorods, Nanospindles, and Nanobullets.....	103
2. Experimental Techniques.....	106
2.1 The Synthesis of CdS/CdSe Nanorods.....	106
2.2 The Synthesis of CdS/CdSe Nanospindles/Nanobullets.....	107
2.3 The Growth of Au tips on CdSe/CdS.....	107
3. Result and Discussion.....	108
4. Conclusion.....	114
Chapter V: Summary and Future Outlook.....	115
References.....	117



## List of Tables

Table 1.1 Fundamental physical properties of some important metal-oxide semiconductors.....	7
Table 2.1 Synthetic conditions for Fe <sub>3</sub> S NPs.....	39
Table 3.1 Reaction rate by fitting to data presented in the Figure 3.18C.....	89

## List of Figures

Fig 1.1 A Lycurgus Cup.....	3
Fig 1.2 The evolution from the continuous conduction and valence band of bulk semiconductors to discrete size-dependent atomic-like energy levels.....	6
Fig 1.3 Schematic of localized plasmon oscillation of free electrons in a small spherical metal particle.....	9
Fig 1.4 The 3D assembly of FePt system.....	12
Fig 1.5 Size-dependent photoluminescent colors of colloidal CdSe NPs.....	15
Fig 1.6 The first successful synthesis of CdSe NPs.....	16
Fig 1.7 As the size of the Au NPs increases, the LSPR peak red-shifts in the absorption spectra and the full width at half maximum broadens.....	17
Fig 1.8 The variation of surface area/volume as a function of length for different Morphologies.....	18
Fig 1.9 TEM images of the growth of pine tree-shaped wurtzite CdSe NPs.....	20
Fig 1.10 Band-gap energy diagram of CdSe nanorods.....	21
Fig 1.11 Schematic diagrams illustrating the artificial shapes of NMNs.....	22
Fig 1.12 Schematic illustration of a nanooligomer with three distinct domains, possessing different functionalities.....	24
Fig 1.13 Fluorescence differences for doped CdSe NPs (in toluene) with specified amount of Ag <sup>+</sup> cations.....	26
Fig 1.14 JEOL JEM 2100 TEM (LaB6) and JEOL JEM 2100F TEM/STEM in the NISP Lab.....	29
Fig 1.15 Shimadzu UV2501PC UV-vis Spectrophotometer.....	30
Fig 2.1 Fe-S and (Fe,Ni)-S phase diagrams extrapolated from existing experimental data.....	33
Fig 2.2 The synthesis of Fe <sub>3</sub> S NPs from molecular precursors.....	36
Fig 2.3 Tuning the size of Fe <sub>3</sub> S NPs.....	41
Fig 2.4 The evolution of Fe <sub>3</sub> S NPs with extended reaction time.....	42
Fig 2.5 Size dependent magnetic property measurements.....	42
Fig 2.6 The synthesis of Fe <sub>3</sub> S <sub>2</sub> NPs starting from molecular precursor.....	44
Fig 3.1 Schematics of the gel trapping technique for replicating microparticle mono layers at oil water and the air-water interfaces.....	47
Fig 3.2 SEM images of heterodimer Au-PS particles fabricated by gold sputtering on a monolayer of 2.7μm sulfate PS latex particles embedded on the surface of PDMS.....	48
Fig 3.3 TEM images of Fe <sub>3</sub> O <sub>4</sub> FePt-Ag, and Ag-AuNPs.....	49
Fig 3.4 TEM images of evolution of a single Ag@SiO <sub>2</sub> particle to AgI-SiO <sub>2</sub> dimer.....	51
Fig 3.5 TEM of the dumbbell-like Au-Fe <sub>3</sub> O <sub>4</sub> NPs.....	53
Fig 3.6 Flowchart of the bottom-up method to build a complex nanooligomers starting from a single seed.....	55
Fig 3.7 Series of high and low-resolution TEM images highlighting different synthetic stages of Au-CdSe growth.....	72
Fig 3.8 High resolution TEM images of orientations of different crystalline domains at the boundary of individual Au-CdSe NPs.....	73

Fig 3.9 Low and high resolution TEM images of tuning the sizes of CdSe part in Au-CdSe NPs.....	74
Fig 3.10 Sets of high and low-resolution TEM images demonstrating different synthetic stages of Pt-CdS growth.....	76
Fig 3.11 Control over the number of Pt facets occupied by CdS.....	77
Fig 3.12 Different combinations of nanotrimers were synthesized by similar routines....	78
Fig 3.13 A nanooligomers consisting of four subunits.....	79
Fig 3.14 Schematic of the growing process for Pt-Ag/Au-Ag <sub>2</sub> Se-CdSe NP and a possible mechanism for Au <sup>+</sup> /Ag <sup>+</sup> substitution.....	81
Fig 3.15 The nanodumbbells system of CdSe rods with Au tips on the both sides.....	82
Fig 3.16 Comparison of normalized absorption spectra for different module sizes.....	84
Fig 3.17 Au@CdSe optical properties and explanations.....	84
Fig 3.18 Hot-plasmon driven photocatalysis of the Pt-Au <sub>x</sub> Ag <sub>y</sub> -CdSe nanooligomers.....	87
Fig 3.19 Summary of our model reasoning.....	92
Fig 3.20 Photocatalysis measurement with physical mixture of Pt-Au heterodimers and CdSe nanoparticles (1:1 molar ratio).....	92
Fig 3.21 Calculated extinctions for different subunits.....	95
Fig 3.22 Plasmon-mediated photocatalytic reduction of the MB molecule.....	97
Fig 3.23 Optical characterization of photocatalytic reduction of the MB molecules by nanooligomers.....	100
Fig 3.24 Low- and high-resolution TEM characterizations of Pt-Au <sub>0.80</sub> Ag <sub>0.20</sub> -CdSe nanooligomers before (A) and after (B) photocatalytic reactions.....	100
Fig 3.25 Excitation wavelength-dependent photocatalytic measurements of the Pt-Au <sub>x</sub> Ag <sub>y</sub> -CdSe nanooligomers.....	101
Fig 4.1 Schematic representation of energy-level alignment in the core-shell CdSe/CdS nanostructure.....	104
Fig 4.2 TEM images of synthesized CdSe/CdS nanostructures under different conditions, with schematic demonstrations of location of the CdSe core.....	109
Fig 4.3 The deposition of Au to the tips of CdSe/CdS nanostructures.....	111
Fig 4.4 Comparison of absorption spectra between CdSe/CdS nanostructures.....	113
Fig 4.5 Absorption spectra for Au tipped CdSe-CdS nanorods.....	113

# Chapter I: Introduction

*An invitation to enter a new field of physics*

*by Richard P. Feynman*[1]

## *1. The Background of Nanotechnology and Nanotechnology*

To scientists and engineers, terms starting with the prefix “nano,” like “nanoscience” and “nanotechnology,” indicate a manipulation of materials from one nanometer to a few hundred nanometers in one or more dimensions. Assemblies of atoms from tens to billions of nanomaterials (NMs) are the intermediaries between molecules and bulk materials. As far as scaling down the size, the collapse of the periodic boundary condition makes NMs behave differently from their bulk counterparts. Physicists predicted that nanoparticles (NPs) with a diameter of 1–10 nm would display atomic-like electronic band structures because of the quantum-mechanical rules[2]. Meanwhile, the increase in the surface-area-to-volume ratio would drive more NM atoms to the surface, which in turns can lead to a decrease in the melt point [3], enhanced catalytic abilities[4], and a shift in optical properties[5].

Over the last three decades, scientists have been attracted to the unique physics and diverse potential of nanoscience and nanotechnology. It has been said that these fields of study could form the foundation for the next “industrial revolution.” [6] Leaders in the field are consistently trying to gain a better understanding of the dominant quantum effect and the surface/interface effect at nanoscale. These are the key factors in the regulation

of properties of materials that lead to unique phenomena and novel applications. Those applications include but are not limited to energy[7], materials[8], health[9], and information technology[10].

The body of knowledge in the field of nanoscience has become increasingly comprehensive over the years. In ancient times, people were already manufacturing NMs for daily use. One common example is gold colloid, which artisans used to add a variety of vivid colors to other materials. Figure 1.1 shows a Lycurgus cup dating back to the fifth century BC. It has dispersed gold colloid in the glass, which appears ruby red in transmitted light and green in reflected light[11]. However, people did not recognize the connection between the shifting color and the form of gold for another two thousand years, when German chemist Johann Kunckels realized that “drinkable gold that contains metallic gold in a neutral, slightly pink solution . . . exert[s] curative properties for several diseases” and concluded that “gold must be present in such a degree of communitation that it is not visible to the human eye” [12].

Three centuries later, the physicist Richard Feynman proposed the full concept of the “bottom of physics” [1]. He sketched the framework of nanoscience and nanotechnology in his famous lecture at the Annual American Physical Society Meeting in 1959. From then on, scientists have made a massive effort to explore this “bottom”. Professor Norio Taniguchi introduced the term “nanotechnology” in 1974 when he addressed the scaling issues caused by the changing magnitude of various physical parameters[13]. He also designed a method to manipulate and characterize materials at nanoscale and predicted their potential applications. Gerd Binnig and Heinrich Rohrer’s

invention of the scanning tunneling microscope (STM) at IBM helped to realize Taniguchi's ideas. There was further progress in 1985 when Gerd Binnig, Christopher



Fig 1.1. A Lycurgus Cup, a Roman glass cage cup at the British Museum. It was made of a dichroic glass, which takes on different colors depending on whether light is passing through it. It is red when lit from behind and green when lit from the front. Au NPs embedded in the glass are about 70 nanometers across.

Gerber, and Calvin Quate developed an atomic force microscope (AFM) to overcome STM's major weakness, which is that it requires conducting surfaces for investigation. In the same year, Harold Kroto, Robert Curl, and Richard Smalley discovered buckminsterfullerene ( $C_{60}$ ), the first molecule in the fullerene family[14]. The van der Waals diameter of a  $C_{60}$  molecule is 1.01nm, which meets the criteria for NMs and it also possesses properties that resemble molecules. Nanoscience and nanotechnology have advanced in vast and far-reaching ways over the last 20 years. Notable milestones include

one-dimensional carbon nanotubes[15], graphene[16], and zero-dimensional colloidal semiconductor quantum dots[17]. Because of these groundbreaking discoveries, scientists have been inspired to delve deeper into the exciting fields of nanoscience and nanotechnology.

My four-year graduate research in Dr. Ouyang's group has focused primarily on the precise and tunable control of the composition, component, and morphology of nanostructures with considerable focus on their size distribution and monocrystalline features. Those nanostructures serve as model systems to explore fundamental aspects of science and are building blocks for practical applications.

The first chapter of this thesis begins with an overview of fundamental concepts and the current progress of nanoscience, including semiconductor, noble metal, and magnetic nanostructures. We briefly present their related key optical, electronic, and magnetic properties. We have also listed and discussed in detail the primary factors shaping the properties of different types of nanostructures. Chapter II covers an experimental strategy to achieve delicate control over the composition of novel nanostructures. This strategy starts with the synthesis of specific molecular precursors that contain the same ratio of elements as the target nanostructure. When the molecular precursor decomposes, its nonvolatile part forms a nanostructure with the same composition as the single molecule. The third chapter presents a combined strategy that utilizes a facile and general intermediate medium as the foundation of new components to existing NP seeds. We have also prepared and carefully tuned a set of nanostructures as model systems in order to investigate their nanoscale optics, plasmonics, and catalytic properties in an accurate way. We have defined these systems by studying the interactions between different

components like photons, phonons, excitons, and plasmons. Specifically, we have found an interesting catalytic mechanism that involves hot plasmons and excitons. The fourth chapter describes my control over the morphologies of a series of nanostructures and includes analysis of the crystal structure information of these morphologies and projections of possible growth mechanisms. Finally, this thesis concludes with a summary and a prediction for the future.

## *2. Nanomaterials in Our Research*

We are interested in exploring various emerging physical phenomena at nanoscale, such as light-matter-spin interactions. Certain NMs share common properties that are only available to their particular type. For example, the localized surface plasmon resonance (LSPR) only occurs in metallic NMs. Thus, for a more straightforward and efficient discussion, we will introduce each NM by type.

### 2.1 Semiconductor Nanomaterials

With the boom of the semiconductor industry, the research on semiconductor NMs has grown extensively over the past few decades. Semiconductor NMs inherit some properties from the bulk semiconductor, like the concept of an “electron-hole pair,” as they develop unique and fascinating properties. Unlike the pure bulk semiconductor that has a fixed band structure, which can be only adjusted by limited means like doping, the semiconductor NMs have gained additional modulations in size (Fig 1.2), morphology, composition, and surface status so that it is possible to adjust the band structure according to need.



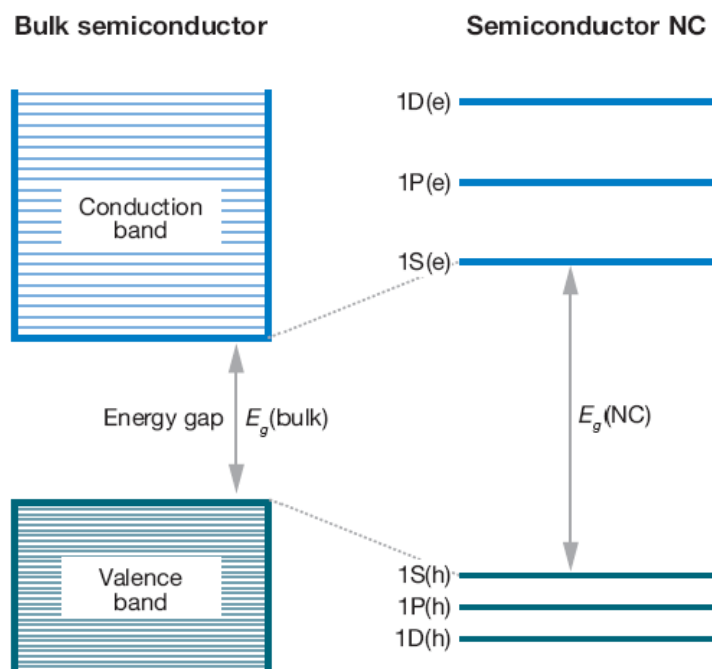


Fig 1.2. The band structure in semiconductors. It evolves from the continuous conduction and valence band of bulk semiconductors to discrete size-dependent atomic-like energy levels. Reprinted from Ref. [18].

Varieties of semiconductor NMs have been proposed and synthesized. They can be sorted into few categories by the element group: II–VI semiconductors including metal oxides, III–V semiconductors, I–VII semiconductors, and Group IV, which includes semiconductors and multiple-component alloys.

The most common semiconductor NMs in research are the II–VI semiconductors, whose prototypes are salts of cadmium and chalcogens. Among them, CdSe has been extensively studied due to its band gap in the visible range [19] and chemical stability[20]. Most of the usefulness of CdSe stems from NPs, whose size are below 100 nm and depend on quantum confinement. CdSe can be utilized in opto-electronic devices and for nanosensing, biomedical imaging[21], and to create high-efficiency solar

cells[22][23]. The manufacture of CdSe-based laser diodes allows us to cover a large part of the electromagnetic spectrum because of its size- dependent fluorescence spectrum[24]. Similarly, when CdSe NPs are tuned to a size at which they can emit far infrared light that can permeate human tissue, doctors can then inject the CdSe NPs into injured tissue to produce an image[25].

Metal Oxides	Crystal	Conductive Type	Band Gap/eV as bulk	Sensing Light
ZnO	Hexagonal	n	3.37	UV
SnO <sub>2</sub>	Tetragonal	n	3.6	UV
Cu <sub>2</sub> O	Cubic	p	2.17	Visible
β-Ga <sub>2</sub> O <sub>3</sub>	Monoclinic	n	4.2–4.9	UV
α-Fe <sub>2</sub> O <sub>3</sub>	Rhombohedral	n	2.1	Visible
In <sub>2</sub> O <sub>3</sub>	Cubic	n	3.6(direct)/2.5(indirect)	UV
CdO	Cubic	n	2.77(direct)/0.55(indirect)	Visible
CeO <sub>2</sub>	Cubic	n	3.2	UV

Table 1.1. Fundamental physical properties of some important metal-oxide semiconductors [26].

Metal oxides are another large group of semiconductors that has had a long technological history and been a subject of interest for many scientists. This is because of metal oxides' hardness, thermal stability, and chemical resistance. Transition metal oxides are particularly popular because they can be used in pigments, electronic ceramics,

and cosmetics, and they can provide support in catalysis and as photocatalysts[27]–[29]. The large electronegativity of oxygen broadens the band gap of metal-oxide NMs (Table 1.1), making it wider than other semiconductors with  $S^{2-}$ ,  $Se^{2-}$ , or  $Te^{2-}$ . ZnO is a good example of a metal-oxide NM that can be synthesized into a variety of morphologies including nanowires, nanorods, tetrapods, nanobelts, nanoflowers, and nanoparticles. ZnO is a wide-band-gap compound semiconductor with large exciton binding energy (60 meV) at room temperature, and so scientists consider it to be the most suitable material for UV devices when it is compared to the thermal energy of room temperature (26 meV) [27].

III–V semiconductor NMs possess similar electronic and optoelectronic properties. However, because of their difficult synthetic chemistry, studies of these NMs are much less advanced than the research on II–VI semiconductor NMs[30]. III–V semiconductor NMs are more covalent and generally require a high temperature for synthesis, which means that both the stabilizer and the solvent need to pass checks for thermo stability.

## 2.2 Noble Metal Nanomaterials

Noble metal nanomaterials (NMNs) form another major category. Atoms of these elements readily lose electrons to form a cation frame, and the delocalized electrons form an electron cloud. The overlap of the conduction band and valence band makes these metals intrinsically different from semiconductor NMs. Unless the temperature is extremely low ( $<1K$ ) [31], the energy spacing between NMN discrete “electrons-in-a-box” energy levels is still less than the thermal energy factor, even with

several nanometers. This means that NMNs maintain many properties as their bulk, like high electron mobility.

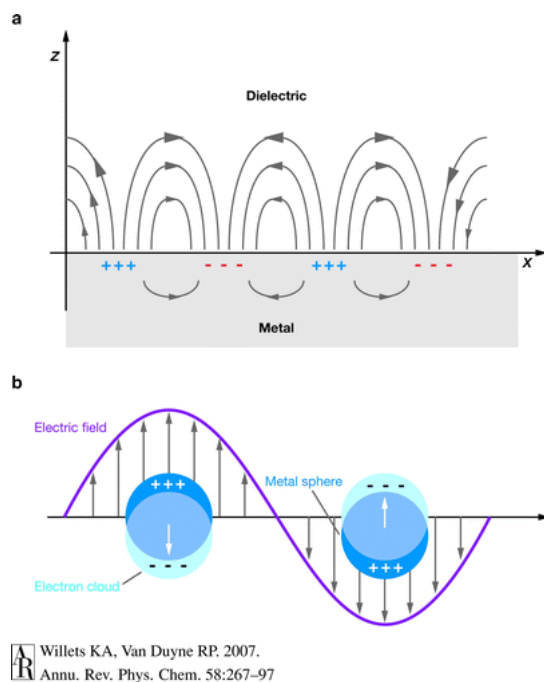


Fig 1.3. Schematic of localized plasmon oscillation of free electrons in a small spherical metal particle. Source: Willet KA, Van Duyne RP, 2007, Annu. Rev. Phys. Chem. 58:267–97

Delocalized electrons yield other interesting size-dependent electrical[32], optical[33], magnetic[34], and chemical properties[35]. For example, artists throughout history have taken advantage of the localized surface plasmon resonance (LSPR) by using NMNs as decorative pigments in stained glass and other forms of art[36]. Collective electron charge oscillations in the metallic NMNs are excited by light and exhibit enhanced near-field amplitude at the resonance wavelength (Fig 1.3). The field is highly localized at the NMNs, so it has spatial dependent resolution limited only by the NMNs' size and shape. Among NMNs, scientists most commonly study Au and Ag for their LSPR

because their nanostructures generally exhibit visible SPR absorption, whereas Au nanorods, Au nanocage, and hollow Au nanospheres present strong near-infrared absorption[37]. Both Au and Ag are biocompatible. An easy surface modification allows their nanostructures to attach to biomolecules, polymers, or other ligands. Therefore, they can be useful for drug delivery, tissue/tumor imaging, and photothermal therapy.

At nanoscale, the increased surface-area-to-volume ratio enhances the performance of the traditional noble metal catalysts. Pt NMs with high-index facets, complex morphologies (e.g., dendritic structure) or multi-compositions exhibit higher electrocatalytic activities toward small molecule oxidation and oxygen reduction reactions than the commercial catalysts[38][39].

When comparing the size of certain noble nanoclusters (Au, Ag, and Pt in particular) to the Fermi wavelength of electrons, the nanoclusters exhibit a strong size-dependent fluorescent emission[40].

## 2.3 Magnetic Nanomaterials

In recent years, the focus on developing new magnetic materials has moved from the microcrystalline to the nanocrystalline regime. This is now the most popular basis for data storage in the future computer[41], but is also applicable to many other fields of science and technology including engineering[42], medicine[43], and biotechnology[44].

Magnetic NMs have many unusual magnetic behaviors in comparison to bulk materials. The reduced size in one or more dimensions of the magnetic system drastically changes the electronic properties by reducing the symmetry of the system, which

heightens the changes in the electronic environment, charge transfer, and magnetic interactions.

This downscale has many positive results. Because the ligands bind to the surface, it is possible to control the magnetic properties of magnetic materials. This control is instrumental to improving performance, which in turn contributes to developments in electronic motors and generators. In the area of magnetic storage media, future progress will also rely on the ability to develop control over microstructure because smaller size scales allow for increased storage densities. By using appropriate interstitial materials, the scientist can arrange magnetic building blocks in an ordered high dimensional array (Fig 1.4) [45]. The array allows for externally tunable inter-particle interactions that in turn, modify properties of the macroscopic materials for future applications as superior performance magnetic memories, sensors, and in the architecture of ultra-high speed large- scale devices[46].

For example, the FePt alloy has controlled sizes and compositions, and is part of an important class of materials that have permanent magnetic applications [47] due to their large uniaxial magnetocrystalline anisotropy ( $K_u \cong 7 \times 10^6 \text{ J/m}^3$ [48]) and relatively good chemical stability. As the magnetic stability of individual particles scales with the anisotropy constant,  $K_u$ , and the particle volume,  $V$ , small FePt NPs may be suitable for application in ultrahigh-density magnetic recording media devices[49].

Currently, however, magnetic NMs present a few troubling limitations. The thermal stability of the magnetic dipole moment of fine particles has become a critical issue. The superparamagnetic limit in magnetic NMs is a result of fluctuations in the magnetization direction due to the reduced size [50]. Meanwhile, most of the atoms located on the

surface mean that the magnetic properties are dominated by phenomena that take place at the interface, makes precision control difficult. Additionally, the quantum limitations produce tiny “magnets” with poor magnetic densities.

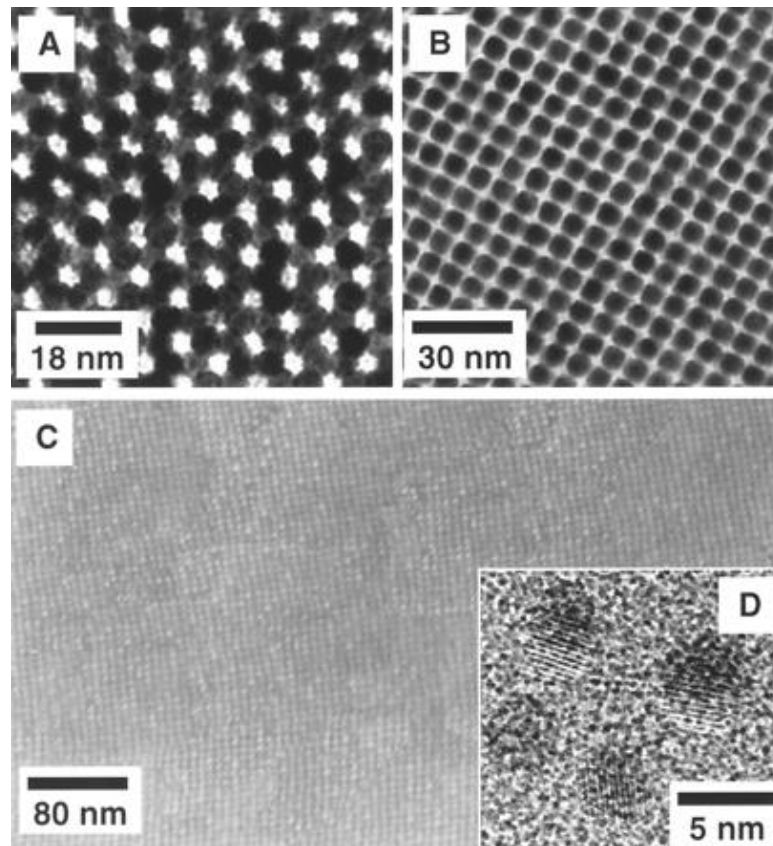


Fig 1.4. The 3D assembly of FePt system. (A) A TEM image of a 3D assembly of 6-nm as-synthesized Fe<sub>50</sub>Pt<sub>50</sub> NPs. (B) A TEM image of a 3D assembly of 6-nm Fe<sub>50</sub>Pt<sub>50</sub> sample after replacing oleic acid/oleyl amine with hexanoic acid/hexylamine as capping ligands. (C) A HRSEM image of a ~180-nm-thick, 4-nm Fe<sub>52</sub>Pt<sub>48</sub> nanocrystal assembly. (D) High-resolution TEM image of 4-nm Fe<sub>52</sub>Pt<sub>48</sub> nanocrystals annealed at 560°C for 30 min. Reprinted from Ref. [47].

### *3. Parameters to Tune the Properties of Nanomaterials*

Well-controlled, high quality NMs are essential for both characterization and practical application. Over the last three decades, scientists and engineers have made significant progress towards determining, revealing, and enhancing the functionalities and possible applications of NMs with their controlled size, composition, component, morphology, and surface[51]–[54].

The physics of these major modulation methods are similar. All of the methods change the electric potential that electrons and nucleuses form in the space occupied by NMs and their affiliations. Varying the size of NMs is the same as a homogenous adjustment in the existing electric potential, while altering the morphology of NMs reorganizes the spatial distribution of the original electric potential. Introducing extra components adds heterogeneous electric potential to the previous one, and tuning the composition of NMs adjusts the electronic potential. Physical and chemical properties of NMs can be tuned over any one of these parameters, but the flexibility and scope of change are highly sensitive to some specific parameters. Thus, it will be incisive and helpful to view the change parameters by the order of size, morphology, module, and composition.

#### 3.1 Size

Size is the factor that differentiates the NMs from the bulk materials. Size has such a large impact on the properties that narrow the size distribution of NMs that it is a crucial aspect of any high-profile research on the subject.



For semiconductor NMs, size affects the energy band gap width between the conduction band and valence band. However, size does not create a sufficient change in the properties of bulk semiconductor materials, so the gap is a fixed parameter that depends on the nature of the materials. Frequently, theorists apply the same periodic boundary condition regardless of the exact size of bulk materials. However, when the size of semiconductor materials is reduced to a certain scale, new physics surface, invalidating the periodic boundary condition.

When bulk semiconductor materials absorb a photon, the action promotes an electron from the valence band into the conduction band, leading to the emergence of “electron-hole” pair emerges. When the size of semiconductor NMs is comparable to or smaller than the natural length scale of the electron-hole pair (Bohr radius), the “electron-hole” pair is confined by the boundaries of the NPs. This condition leads to interesting atomic-like (or molecular-like) optical behavior. This phenomenon is known as “quantum size effect” and arises only because of the finite size of NPs. Quantum dot is named for the semiconductor NPs, especially those with a size smaller than Bohr radius.

It is possible to express the relationship between the electron energy band gap and the size of semiconductor NPs in a simple function of sphere radius with a series of approximations[18][55]. This process treats electrons and holes as quasi-particles, ignores the atoms, and assumes the NP as a bulk. Meanwhile, the Coulomb attraction between electron-hole pairs is justified in the strong confinement regime. Thus, the energy of the electron and hole quantum-size levels, characterized by angular momentum quantum number  $l$ , can be expressed as a parabolic [56] approximation

$$E_{l,n}^{e,h} = \frac{\hbar^2 \phi_{l,n}^2}{2m_{e,h} a^2} \quad (1)$$

where  $m_{e,h}$  is the electron and hole effective mass respectively,  $a$  is the radius of the NP, and  $\phi_{l,n}$  is the  $n$ th root of the spherical Bessel function of order  $l$   $j_l(\phi_{l,n})=0$ . The energy of the lowest electron and hole quantum-size level increases with the decreasing radius. Therefore, the total energy of the band edge optical transitions increases (Fig 1.6). For example, by varying the size of CdSe NPs, its energy gap ranges from 1.2 eV to 1.8 eV, covering almost the whole visual part of the optical spectrum (Fig 1.6) [57].

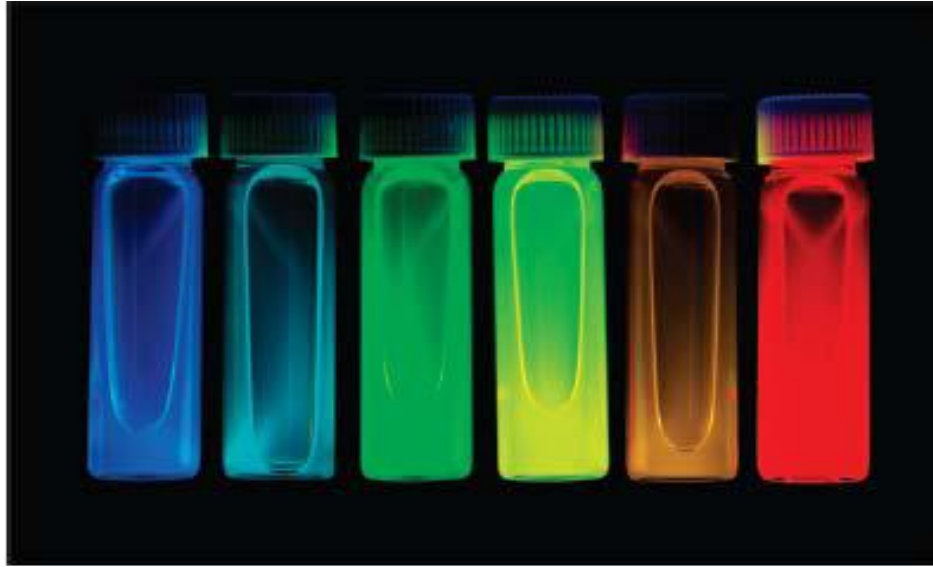


Fig 1.5. Size-dependent photoluminescent colors of colloidal CdSe NPs dispersed in hexane. (Source: <http://nanocluster.mit.edu/>)

Size also affects the LSPR peaks of NMNs[58]. The LSPR of an NMN is determined by its light absorption through the coherent oscillation of conduction band electrons. If the dipole absorption process is isolated, the Mie theory predicts that

$$\frac{\gamma}{NV} = \frac{18\pi\epsilon_{\alpha}^{3/2}}{\lambda} \frac{\epsilon_2}{(\epsilon_1 + 2\epsilon_{\alpha})^2 + \epsilon_2^2} \quad (2)$$

where  $\gamma$  is the extinction coefficient,  $NV$  is the volume concentration of the assembled NPs ( $N$  is the number of spheres per unit volume and  $V$  is the volume of each sphere),  $\epsilon_{\alpha}$

is the dielectric medium constant, and  $\varepsilon(\omega) = \varepsilon_1 + i\varepsilon_2$  is the dielectric function of the NPs[59][60]. As a result of changes in the modulus of  $\varepsilon(\omega)$ , the LSPR band of the NMNs is dependent on its size[61].

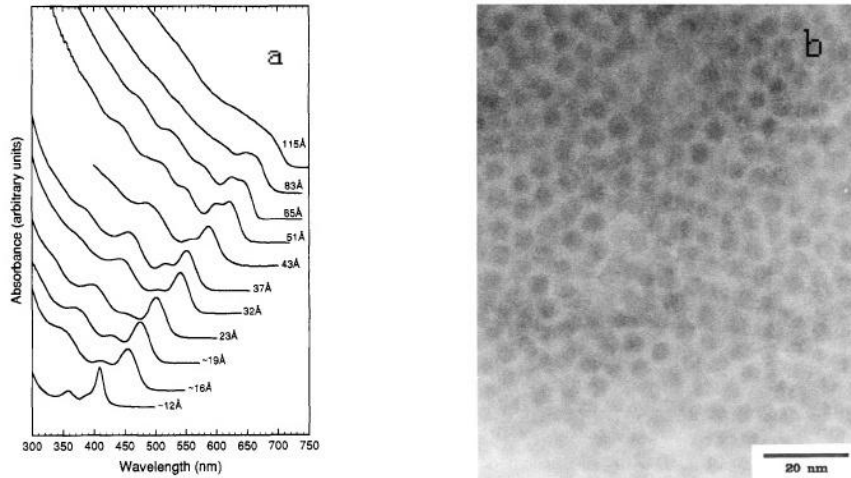


Fig 1.6. The synthesis of CdSe NPs with tunable sizes and narrow size distributions. It was first demonstrated by Christopher Murray et al. by high temperature colloidal synthesis. (a) CdSe NPs ranging from 1.5 nm to 12 nm in diameter have absorption in the visible light range. (b) 8nm CdSe forms closing-pack pattern to indicate a narrow size distribution. Reprinted from Ref. [57].

The size causes changes in the atoms' coordination numbers, the population of the facets, and the concentration of defects for NMN catalysts[62][63], which have both positive and negative effects on the NMNs' catalytic capabilities. The change in the electronic factors modifies the work function of the catalyst surface, depending upon the size of the NMNs. For example, Nørskov tried to elucidate the common notion of

chemisorption energy as a function of the size of Pt NPs via a d-band center model[64]. Mukerjee further demonstrated that the number of d-band holes in catalysts affects their electrocatalytic surface activity towards organic molecules[65]. Minimizing Pt NPs leads to an increase in their surface-area-to-volume ratio (Fig 1.8), which, in turn, reduces the amount of Pt

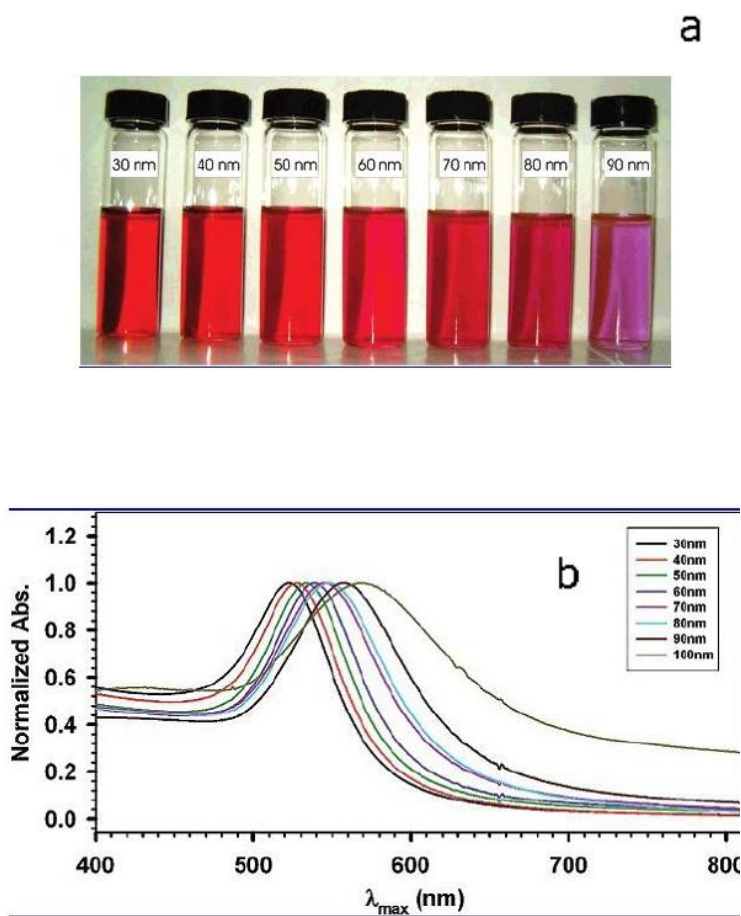


Fig 1.7. The size effect on the LSPR of Au NPs. As the size of the Au NPs increases, the LSPR peak red-shifts in the absorption spectra and the full width at half maximum broadens. (a) A photo showing colors of Au NPs with different sizes. (b) Corresponding UV-vis spectra (normalized). Reprinted from Ref. [58].

consumed economically. On the other hand, when Pt NPs are too small, they show degraded catalytic activity[66]. Thus, one of the most important objectives in the study of nanocatalysis is a greater understanding of the interplay between catalytic activity and the particle size effects, both of which are essential in the development of high-activity catalysts and a reduction in the catalyst load[67].

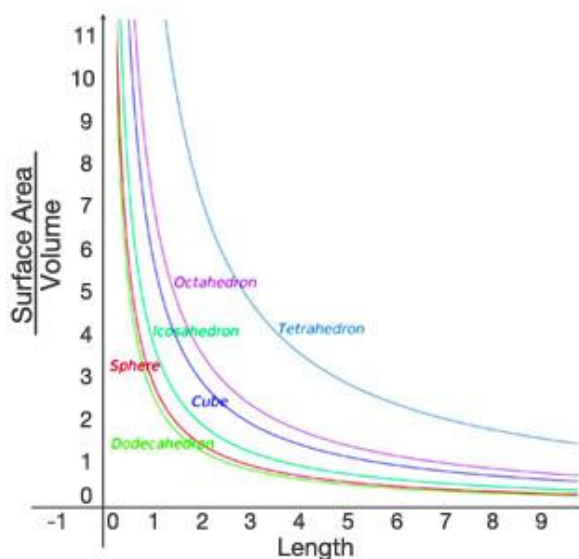


Fig 1.8. The variation of surface area/volume as a function of length for different morphologies. The length has been normalized to be dimensionless. Source: [http://en.wikipedia.org/wiki/Surface-area-to-volume\\_ratio](http://en.wikipedia.org/wiki/Surface-area-to-volume_ratio)

One of the greatest revolutions in the study of magnetic materials is the refinement of synthetic methods that allow the preparation of particles at nanoscale[68]. However, when there is a decrease in the volume of the bulk magnetic system with multidomain structures, it inevitably leads to continuous oscillation in the size of magnetic domains, the width of the domain walls, and their inner structure. Eventually, NPs can possess only one single domain structure, the size of which is defined as a critical size ( $D_c$ ) because the

energy required to create a domain wall of the single domain is greater than the energy needed to support the external magnetostatic stray field. The critical size is determined by the saturation magnetization of particles and the exchange interactions between individual spins, especially the anisotropic energy. High anisotropy may lead to a  $D_c$  above a few hundredths of a nanometer, while most magnetic materials have a  $D_c$  in the tens of nanometers. For spherical particles, the critical diameter falls within 10–800 nm[69]. Typical values for Fe and Co metallic particles are 15 and 35 nm, respectively, while for  $\text{SmCo}_5$  it can be as large as 750 nm[70]. One important parameter in the single domain regime is magnetic coercivity ( $H_c$ ), which determines the actual application of magnetic NMs.  $H_c$  can be calculated by using a function related to the NP volume ( $V$ ) [71]

$$H_c = 2 \frac{K_u}{m_s} \left[ 1 - 5 \sqrt{\frac{k_B T}{K_u V}} \right] \quad (3)$$

where  $K_u$  is the magnetic anisotropic constant,  $m_s$  is the saturation magnetization, and  $k_B T$  is a factor for the thermal energy.

### 3.2 Morphology

NMs frequently require sophisticated nanostructures with non-spherical morphologies. One such example is the bulk heterojunction solar cell, in which scientists predict that nanowires result in an improved performance over spheres[72]. There have been recent developments towards new synthetic methods for the preparation of nanocrystals with elongated (e.g., nanorods, nanowires) and branched (e.g., tetrapods, arrow) (Fig 1.9) morphologies[73][74].

However, the morphology dependence refers to and should contain the aforementioned size dependence, taking into account all three dimensions (meaning both volume and shape should be included). Usually, these two measurements are examined separately in order to follow the diverting mechanisms that are essential to controlling both size and volume in the synthesis.

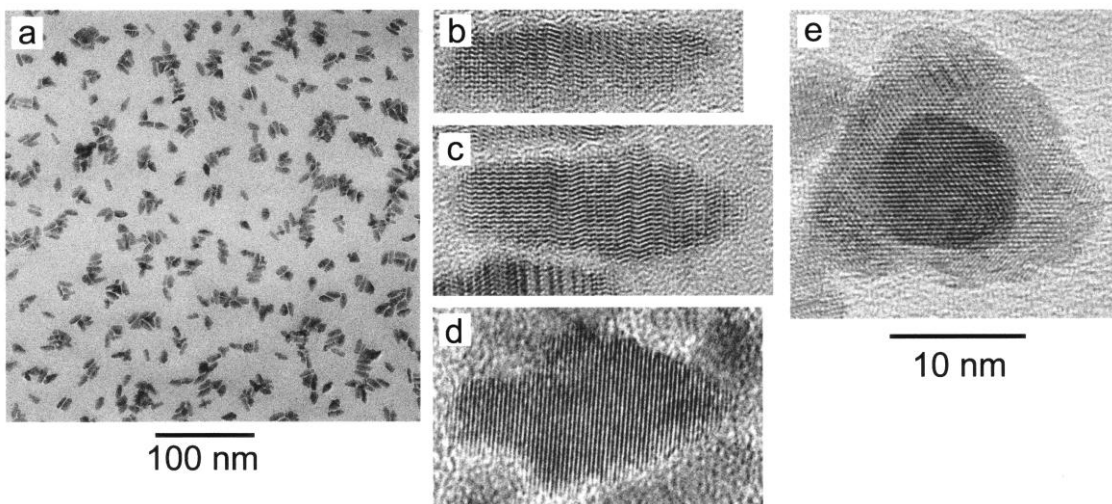


Fig 1.9. TEM images of the growth of pine tree-shaped wurtzite CdSe NPs. (a) A low resolution image of the final product. (b)(c)(d) Pencil/arrow/pine tree at different stages of growth. (e) A pine tree-shaped nanocrystal looking down the  $\{001\}$  direction (or long axis). Reprinted from Ref. [74].

Amplifying the size of NMs requires a higher concentration of precursors and an extended growth time, which falls more under the umbrella of thermodynamics. However, it is not uncommon for scientists to resort to manipulating the growth kinetic in order to drive the product toward unfavored morphologies, which are determined by the thermal equilibrium[75].

Rod- or wire-shaped semiconductor NMs clearly possess different optical properties than their dot-shaped analogues, whose quantum confinement only exists in the radial direction. When a sphere evolves into an anisotropic shape, the quantum confinement extends in more than one dimension. Peng has successfully developed a route to acquire CdSe nanorods with an aspect ratio as large as 10:1[75]. By the length of their short-axis, the CdSe nanorods exhibit electronic and optical features that differentiate them from quantum dots of a similar size. While the absorption peaks of nanorods and quantum dots are quite similar, nanorods have a red shifted photoluminescence peak. Meanwhile, the nanorods aligned on the polymers substrates shows photoluminescence spectra with polarization anisotropy (Fig 1.10b).

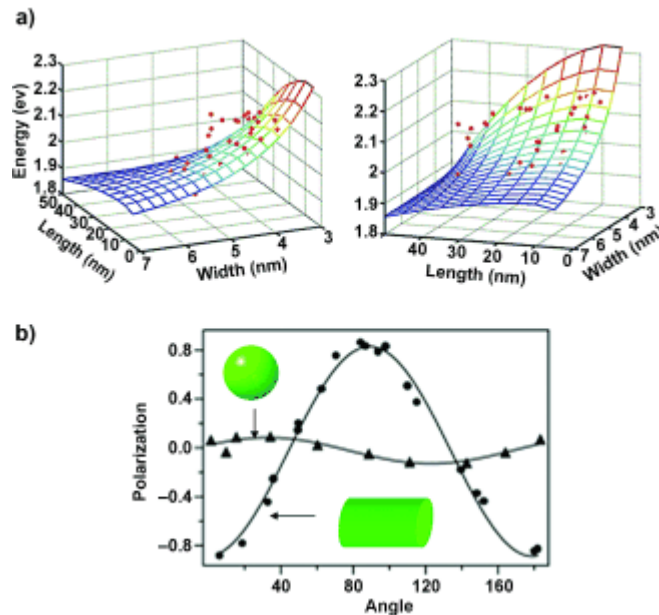


Fig 1.10. The morphology effect on the band structure of the CdSe nanorod. (a) Band-gap energy diagram of CdSe nanorods viewed from different directions. (b) Shape-dependent polarized emission of CdSe. CdSe nanorods have linearly polarized emission properties, while circularly polarized emission is observed from spherical CdSe nanoparticles [76][77].



Scientists discovered a similar anisotropy feature on NMNs long before it was associated with semiconductor NMs. For example, it has been demonstrated theoretically and experimentally that the morphologies of Au or Ag NMs play key roles in determining the feature of LSPR modes, as well as creating the spectral region or polarization dependence necessary for effective molecular detection by SERS (surface enhanced Raman spectroscopy) [52][78]. Another case in point is the LSPR peak of Au nanorods, which is split into two bands because of the difference in the mode of oscillations on the long axis and short axis[79].

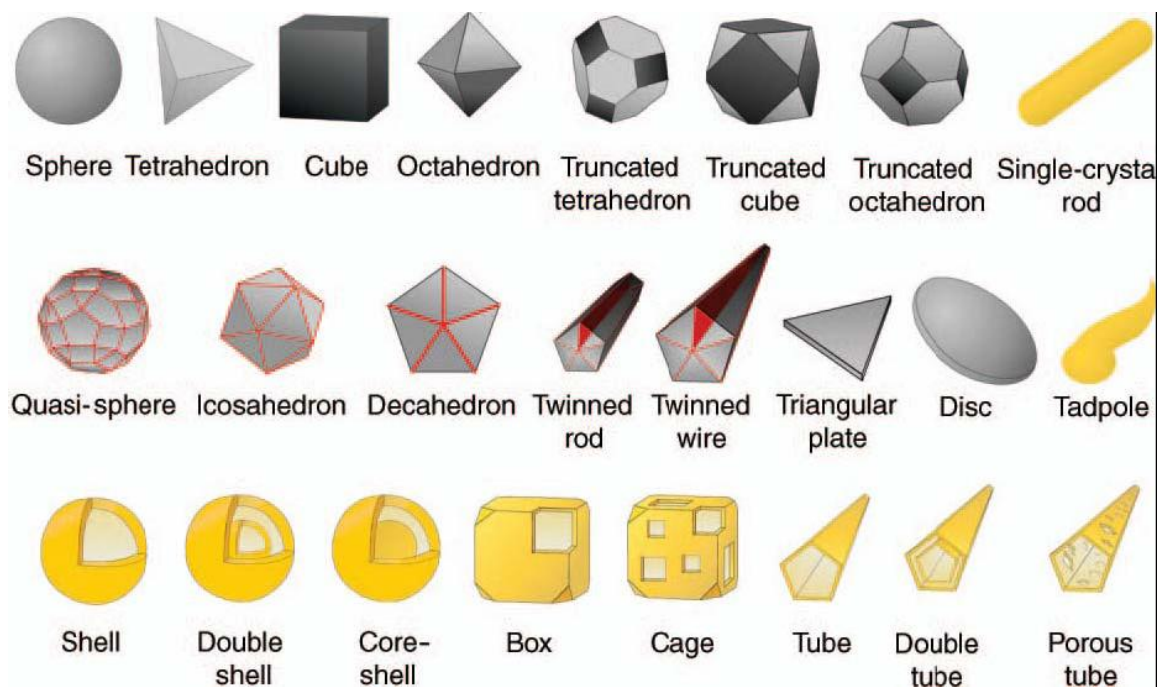


Fig 1.11. Schematic diagrams illustrating the artificial shapes of NMNs. Reprinted from [52].

In the case of catalysis, scientists propose that the catalytic properties of various types of NMNs are dependent on their morphologies, which determine the facets that will be exposed. The up-shift in the d-band center differs from site to site and facet to facet,

leading to catalytic selectivity[80]. One example of this pattern is the catalytic ability of Pt[81], which selectively catalyzes different types of chemical reactions, with {100} and {210} facets being most active for reactions involving H<sub>2</sub> and CO, respectively.

Magnetic properties of NMs are very sensitive to their morphologies because of the anisotropy's dominant role in magnetism. Zhang has demonstrated that cubic CoFe<sub>2</sub>O<sub>4</sub> NPs form a magnetically ordered assembly more easily, while the spherical NPs suffer from disordered magnetization in a 2-D assembly[82]. Therefore, the latter NPs are not desirable for magnetic information storage.

### 3.3 Component

Currently, a single NP can extend itself from mono-component and mono-functionality to multiple-component and multiple-functionality[82][83]. The addition of extra components, besides the size and shape controls, allows for a higher degree of freedom, and thus has unlocked the doors to many possibilities for this field. Scientists have already proposed and realized multiple-component NPs of complex structures, resulting in the emergence of bicompartamental[85], dumbbell-like[86], snowman-like[87], and acorn-like NPs[88]. In our work, we established a topological restriction so that each composition in a multiple-component NP occupies a continuous space. We defined two typical categories of multiple-component NPs which are (1) core-shell structures (NPs with any component wrapped up by others), and (2) "Nanooligomers" (each component has an exposed surface) (Fig 1.12).

Topological differences have unique advantages. For structures with a core-shell, the isolation of the core from the outside environment allows it to remain inert, a requirement

for chemically reactive materials with normal function. High symmetry allows for theoretical modeling although the shell blocks interactions between the inside component and the environment. If extra component-environment interactions are necessary, then the use of nanooligomers is more appropriate. In this paper, we focus on nanooligomers and their advantages.

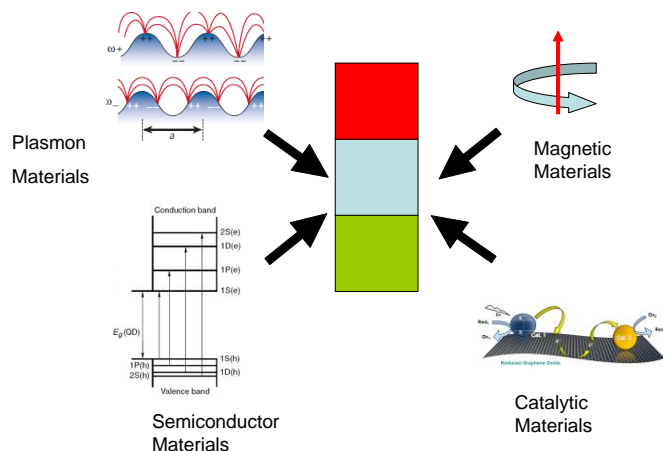


Fig 1.12 Schematic illustration of a nanooligomer with three distinct domains, possessing different functionalities.

The first advantage of nanooligomers is that they integrate different existing functionalities into one single NP in which the properties of individual components are independently optimized. One such example is the CdS-FePt bifunctional heterodimer that Xu's group reported on[89]. Both components of these nanooligomers retain their magnetic and optical properties. Hao investigated this system further and suggested potential biological applications in which the magnetic domain can be used for magnetic detection or navigation and the fluorescent domain utilized for optical detection[90].

Optical detection comes from the enhancement of existing properties and lifting the natural limitations on mono-component materials. For instance, integrating photocatalytic active TiO<sub>2</sub> and noble metals at the nanoscale leads to efficient catalytic oxidation of methanol to formaldehyde[29]. This is because the oxide particles have a significantly larger Helmholtz doublelayer capacitance than space charge capacity, and it makes metal-NP a good photogenerated electron sink to impede electron-hole recombination[28].

Another advantage of nanooligomers is that novel functions are not available in a single-component material or structure. For example, Jonker has identified a new concept called spinpolarized light-emitting diode (spin-LED) [91]. He placed a semimagnetic semiconductor Zn<sub>1-x</sub>Mn<sub>x</sub>Se on a GaAs-based light-emitting diode and injected polarized carriers into the quantum well structure formed by this semiconductor heterostructure and recombined with holes radiatively to emit circularly polarized photons. The resulting spin-LED has the potential to serve as a modulator, encoder, decoder, and quantum bit for quantum computation and communication.

### 3.4 Composition

The composition of NMs plays a vital role in determining their properties. For example, adjusting the amount of dopant replacing cations or anions in semiconductors or alloys eventually leads to a change in charge distributions and relaxation of the lattice. Though this practice can lead to uncontrolled and unintentional defects, it also can reveal many unexceptional properties.

The sensitivity of NMs to the change of composition allows us to observe macroscopic property changes after introducing a single impurity. Experimentally, David Norris's group demonstrated that replacing  $\text{Cd}^{2+}$  in the CdSe nanocrystalline with a few  $\text{Ag}^+$  cations led to detectable changes in the absorption spectra and a dramatic enhancement of the fluorescence efficiency (Fig 1.13) [92].

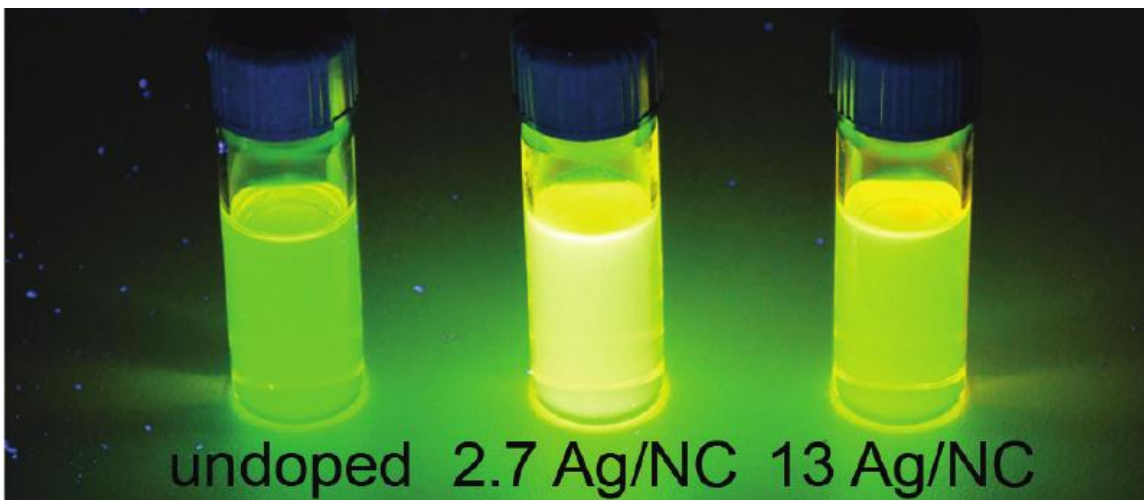


Fig 1.13. Fluorescence differences for doped CdSe NPs (in toluene) with specified amount of  $\text{Ag}^+$  cations [92].

Doping is a common way to introduce impurities to semiconductor NMs. This process involves the incorporation of dopant ions into the NMs crystals lattice structure by direct substitution of constituent anions or cations. The type and amount of ions that participate in this process yield tunable results. Scientists have used either magnetic ions, ions with extra electrons (n-type doping) or ions with extra holes (p-type doping) for doping. The magnetic ions exert an sp-d exchange interaction between the host and the dopant in the semiconductors, making them dilute the magnetic semiconductors (DMSs) [93]. The presence of a magnetic dopant exerts an effective magnetic field, so this

interaction results in unique magnetic and magneto-optical properties. It is possible to achieve additional control on DMSs through enhanced carrier spatial confinement. This control offers extra carriers and enables electrical transport through otherwise poorly conducting materials. There has been a great deal of research on this subject.  $\text{Mn}^{2+}$  and  $\text{Co}^{2+}$  have been proven to modify the photoluminescence of CdSe, ZnSe, and CdS with higher quantum yields[94].

Tuning the composition of an alloy is another way to introduce impurities into semiconductor NMs. In Ag/Au NPs, it is possible to tune the plasmon absorption between 400nm and 500 nm by varying the ratio of Au/Ag in the alloy. Combined with the morphology control, it is possible to extend the plasmon absorption to a longer wavelength[95]. This control is usually achieved by controlling the ratio of precursors participating in the synthesis. In fact, Murray has demonstrated the composition control over the magnetic materials of  $\text{Fe}_x\text{Pt}_y$ [67]. In the high temperature solution phase, the decomposition of  $\text{Fe}(\text{CO})_5$  and reduction of  $\text{Pt}(\text{acac})_2$  in the presence of the stabilizers oleic acid and oleylamine produced 4nm FePt NPs in diameter. Murray tuned the Fe and Pt percentage in the alloy NPs by adjusting the molar ratio of  $\text{Fe}(\text{CO})_5$  to  $\text{Pt}(\text{acac})_2$ . He obtained compositions ranging from  $\text{Fe}_{30}\text{Pt}_{70}$  to  $\text{Fe}_{80}\text{Pt}_{20}$ . Another example can be seen in Au/Ag alloy NPs where the Au/Ag ratio is modulated by the simultaneous reduction in different amounts of  $\text{NaBH}_4$  in a mixture of Au and Ag metal salts[97].

## *4. General Characterization of NMs*

The size, morphology, component, and composition of as-synthesized NPs need to be confirmed and characterized. Current technology enables us to obtain a direct view of those materials and explore their electronic structure via different scientific instruments.

In this section, three widely used techniques for basic characterizations of NPs are introduced briefly.

### 4.1 Transmission Electron Microscopy and Its Associated Facilities

Transmission electron microscopy (TEM) is a powerful microscopy technique that shares a similar mechanism as optical microscopy. It employs a beam of electrons instead of visible light to transmit through an ultra thin specimen. The short de Broglie wavelength of electrons lifts the resolution limit of visible light and a great detail of the materials, as small as a single column of atoms, can be examined as magnified images projected to a fluorescent screen or a CCD camera. Besides the regular mode based on absorption of electrons, alternative modes of TEM and associated facilities allow users to check chemical identity, crystal orientation, electronic structure and sample induced electron phase shift. These techniques are consisted of the “diffraction mode” of TEM, scanning mode (STEM), combined energy dispersive x-ray spectrometer (EDS), electron energy loss spectrometer (EELS), etc. TEM functions as a primary analysis method in multiple scientific fields, especially in physical and biological science. Nanotechnology and semiconductor research benefit from it to advance swiftly in the past years.

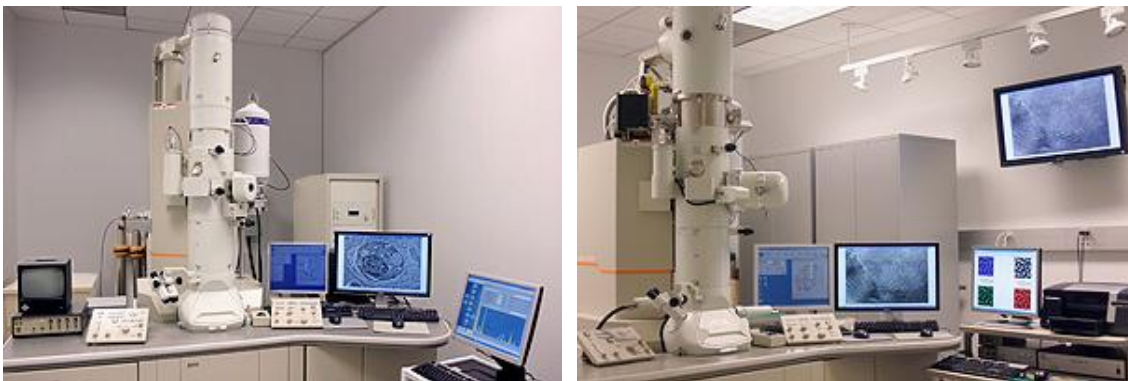


Fig 1.14. JEOL JEM 2100 TEM (LaB<sub>6</sub>) and JEOL JEM 2100F TEM/STEM in the NISP Lab.

We used EDS in STEM mode frequently to investigate samples to collect information not included in images, for instance, to acquire the chemical composition of materials from a small point or a line profile, or to draw elemental distribution maps.

## 4.2 Ultraviolet-visible Spectroscopy

Ultraviolet–visible spectroscopy (UV-vis spectroscopy) refers to absorption spectroscopy or reflectance spectroscopy in the ultraviolet to visible spectral region. This technique measures the absorption of photons by the sample from the ground state to excited states, either in the forms of excitons or plasmons. In practice use, the monochromatic beams of light is generated by a prism or diffraction grating and then split into two equal intensity beams by beam splitter. One beam, i.e., the sample beam, passes through a cuvette containing a solution of NPs in a transparent solvent. The other beam, the reference beam, passes through an identical container containing only the solvent. Both the intensities of these light beams are then measured by light detectors and compared.



When the morphology including the shape and the size distribution of semiconductor NPs is already known, the UV-vis spectroscopy is an economic alternative for TEM to collect information about the size and size distribution information of NMs from the peak position and its full width at half maximum. Also, this spectroscopy can be used to calibrate an unknown concentration of a NP solution by Beer's law.



Fig 1.15. Shimadzu UV2501PC UV-vis Spectrophotometer. The working wavelength for this machine is from 200nm to 900nm.

### 4.3 Fluorescence Spectroscopy

Fluorescence spectroscopy is a complementary technique to absorption spectroscopy, which analyzes fluorescence from a sample. It employs a beam of light (laser in our laboratory), usually ultraviolet light, to excite the electrons in the sample NPs and cause them to emit light; typically, but not necessarily, visible light.

Fluorescence spectroscopy is primarily concerned with energy levels of semiconductor NPs as. In fluorescence spectroscopy, the NPs first absorb photons to be excited from their ground electronic state to one of the excited electronic states. The electrons then return to the ground electronic state, emitting a photon in the process. Due to the discrete energy levels, the emitted photons will have distinctive frequencies. By analyzing the frequencies of light emitted in fluorescent spectroscopy, along with their relative intensities, the structure of the different energy levels can be revealed.

In a typical experiment, either the excitation light or the emission light can be hold at the constant wavelength, while the other has been scanned through different wavelengths. The form is called an emission spectrum and the later called excitation spectrum. An emission map is measured by recording the emission spectra resulting from a range of excitation wavelengths and combining them all together. It will be a three dimensional surface data set: emission intensity as a function of excitation and emission wavelengths, and is depicted as a contour map.

## *5. Summary*

In this chapter, we reviewed fundamental concepts of semiconductor, noble metal, and magnetic NMs. Their synthesis, characterization, and application have also been covered, as well as the parameters needed to harness their properties. The following chapters will focus on more specific NP topics with different modulations.

## Chapter II: Unusual Compositions of Stoichiometric Iron-Rich Iron Sulfide NPs $\text{Fe}_3\text{S}$ and $\text{Fe}_3\text{S}_2$ : Synthesis and Magnetic Property<sup>1</sup>

*Genius, is about 2% inspiration and 98% perspiration.*

*by Thomas Edison*

*I am 98% inspiration and 2% perspiration.*

*by Lin Weng*

### *1. Introduction*

Experts in science and technology have become significantly more interested in magnetic NPs over the past several years. This trend is because nanoscale magnetic materials can offer model systems to understand nanoscale magnetism and also provide exciting opportunities for various applications in ferrofluids or biomedical and magnetic storage[98]–[103], for example. Among all of the magnetic NPs reported so far, the most common species are the iron based magnetic nanostructures such as iron oxides (maghemite and magnetite), with well-controlled size and morphology. However, the inert nature of an oxide surface typically makes it difficult for surface functionalization, thus limiting related applications of iron oxides. Another important class of iron- based magnetic materials is the iron sulfides with stoichiometric compositions. Bulk iron

---

1. This part was adapted from: Lin Weng, Yun Tang, and Min Ouyang, Stoichiometric Iron-Rich Iron Sulfide Nanoparticles ( $\text{Fe}_3\text{S}$  and  $\text{Fe}_3\text{S}_2$ ): Synthesis and Magnetic Property, unpublished.

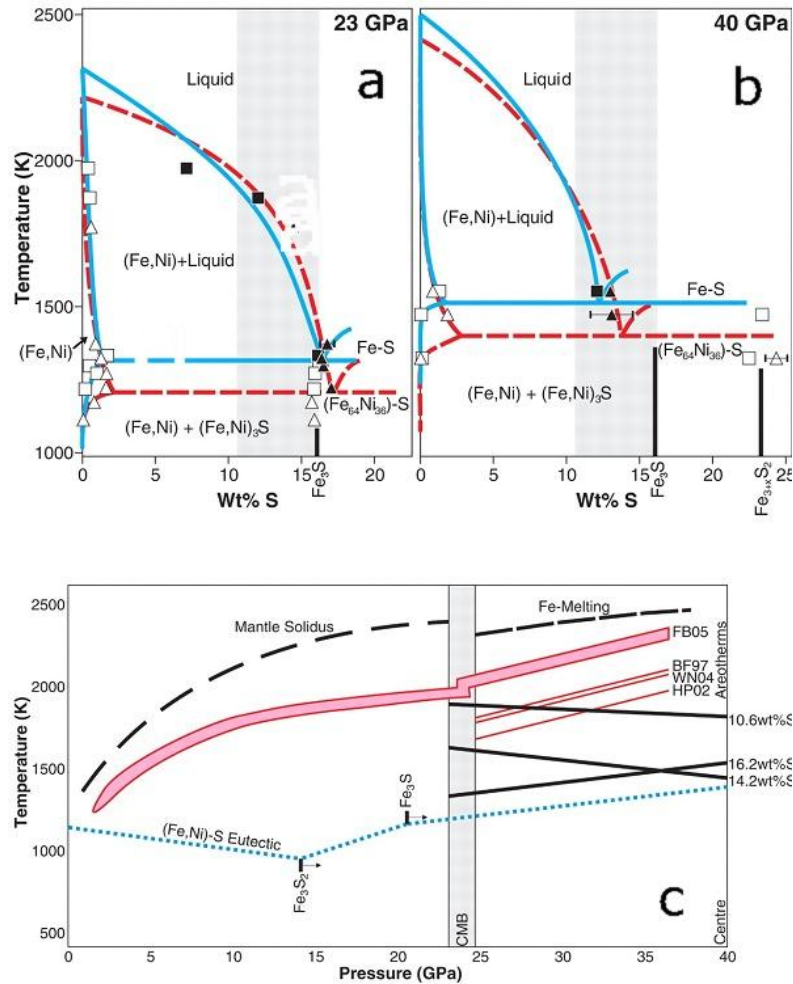


Fig 2.1. Fe-S and (Fe,Ni)-S phase diagrams extrapolated from existing experimental data. (a)/(b) Fe-S and (Fe,Ni)-S phase diagrams at 23/40GPa. Fe-S results, squares; (Fe,Ni)-S results, triangles; liquid phases, black symbols; solids, white symbols. The resulting phase boundaries for Fe-S are shown in solid blue lines. Thick black vertical lines indicate the composition of stable sulfide phases, as indicated along the x axis. (c) Effect of pressure on the Fe-S and (Fe,Ni)-S systems. Eutectic temperature inflections around 14 and 20 GPa are due to the stabilization of Fe<sub>3</sub>S<sub>2</sub> and Fe<sub>3</sub>S above these pressures. Below the blue dotted line, these two compounds will dissociate into Fe and pyrrhotite phase, Fe<sub>1-5</sub>S [104]. The pressure of the core/mantle boundary (CMB), the mantle solidus, and the melting curve of pure Fe are given for reference. Reprinted from Ref.[105].

sulfides display rich structural motifs and phases, and have been used for catalysis, batteries and solar cells[106]–[109]. As compared with the vast information available on iron oxide NPs, experimental studies of iron sulfide nanostructures are rare and mainly limited to sulfur-rich compounds. To date, there is no report on iron-rich iron sulfide nanostructures[110]–[113]. This is because of the inherent challenge in the synthesis and control of the stoichiometry of these materials. The Fe-S system possesses a complex phase diagram with extremely high eutectic temperature (e.g.,  $\sim 1000^\circ\text{C}$  with 31 wt% of S at one atmosphere), and the only way to increase the iron ratio in the eutectic composition is to increase pressure[114][115]. For example, even though the  $\text{Fe}_3\text{S}$  is the most iron-rich stoichiometric iron sulfide known to date in the Fe-S system, it was found to be an intermediate phase at pressures between 14-18 GPa (Fig 2.1c), and could only be synthesized and investigated under extreme condition achieved by the diamond anvil cell, or it could be found naturally existing in the planetary core under extremely high pressure and high temperature[114][116][117]. Another iron-rich compound,  $\text{Fe}_3\text{S}_2$ , behaves similarly by appearing as an intermediate phase at 14GPa[114][115]. Due to such inherent challenges in the synthesis and control of stoichiometry of iron-rich compounds, their properties can only be obtained by extrapolation of these properties measured with a low iron compound or under these rare extreme conditions[118]–[121].

Scientists believe that sulfur is the light-alloying element in the iron-rich cores of planets like Mars and Earth[122]. It is thus crucial that we develop a more complete understanding of the properties (structures, magnetism, phase relationships, etc) and formations of nanoscale stoichiometric iron-rich compounds under normal synthetic conditions because they may play a significant role in understanding the evolution and

the physical properties of planetary cores that are governed by the mineralogy of these compounds and have unfortunately been very challenging to explore[105][115][123].

Herein we report for the first time a facile controlled synthesis of two different stoichiometric  $\text{Fe}_3\text{S}$  and  $\text{Fe}_3\text{S}_2$  NPs under low temperature and ambient pressure by using single-source molecular precursors possessing a pre-defined ratio of Fe and S. In particular, we were able to control the size of the  $\text{Fe}_3\text{S}$  and  $\text{Fe}_3\text{S}_2$  NPs with near mono-dispersed distribution ranging from 2 to 12nm. We investigated the details of the structural and compositional change of the Fe/S ratio during the synthesis, which shed light on the phase evolution of such iron-rich compounds. We further characterized size-dependent magnetic properties of  $\text{Fe}_3\text{S}$  to reveal that  $\text{Fe}_3\text{S}$  NPs can display superparamagnetism with two intriguing magnetic transition temperatures. Successful synthesis of these two stoichiometric iron-rich NPs under regular lab conditions provided a valuable opportunity to further explore their physical and chemical properties that cannot be achieved otherwise.

Due to the complex phase diagram of the Fe-S system (Fig 2.1), conventional nanoscale synthetic methods, such as co-injection of Fe and S sources with pre-defined iron-rich ratios, have typically led to phase separation instead of NPs with specific stoichiometry. On the other hand, single-source molecular precursors have been applied as organometallic sources to prepare different compound thin films and nanostructures with well-defined stoichiometry in solution phase or gas phase[124]–[128]. While exist many iron-sulfur clusters exist that can potentially be used as single-source molecular precursors for an iron-sulfur compound[129][130], we chose  $(\text{OC})_9(\mu\text{-CO})\text{Fe}_3\text{S}$  as the single source molecular precursor for  $\text{Fe}_3\text{S}$  NPs based on following considerations: (1) it

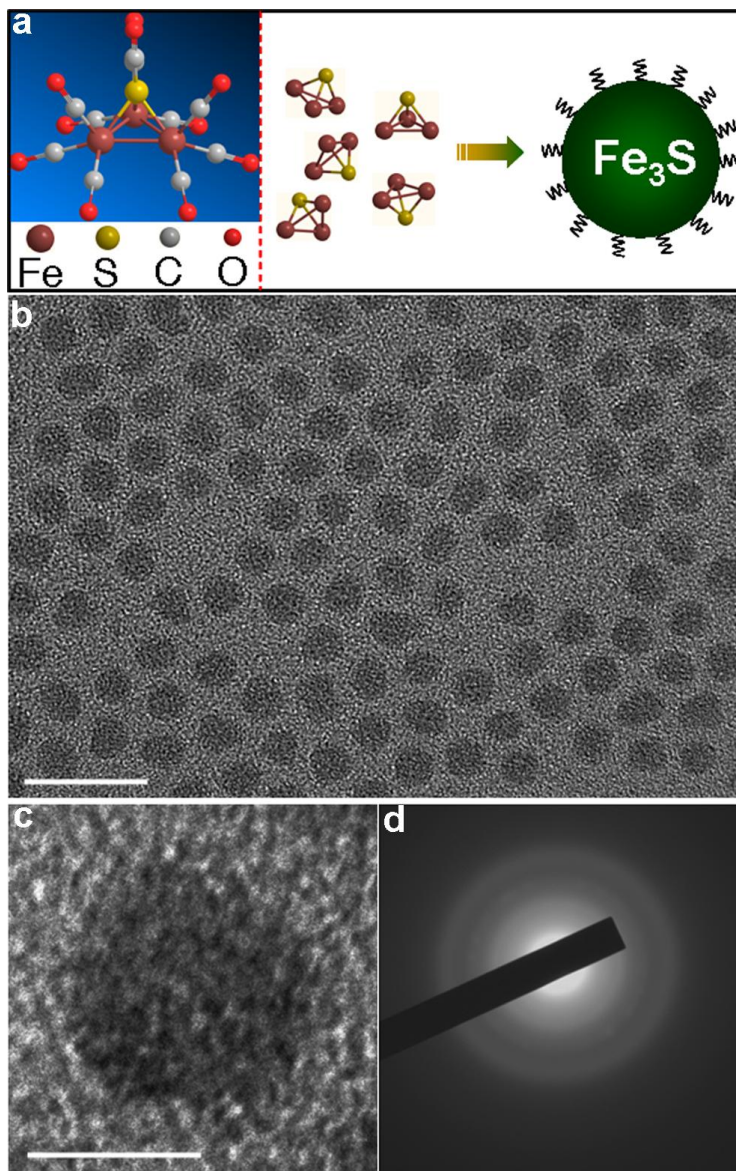


Fig 2.2. The synthesis of  $Fe_3S$  NPs from molecular precursors. (a) Left: The molecular structure of  $(OC)_9(\mu-CO)Fe_3S$ . Bond lengths are drawn in a ratio according to X-ray data. Right: Schematics of the formation of  $Fe_3S$  when carbonyl groups dissociates and  $Fe_3S$  cores nucleate by the aid of capping ligands. (b) A TEM image of 7nm  $Fe_3S$  NPs of a narrow size distribution. Scale bar, 20nm. (c) A typical high resolution TEM image of a single  $Fe_3S$  NP. Scale bar, 5nm. (d) The diffraction patterns of  $Fe_3S$  NPs acquired by TEM.

possesses a precise stoichiometric 3:1 ratio of Fe to S with well-defined chemical bonding between Fe and S (Fig 2.2a); (2) compared with other coordinate groups, the bond strength of Fe-(CO)<sub>x</sub> is much weaker (32-160KJ/mol) than that of Fe-S (300KJ/mol). Therefore, with careful control of the thermal decomposition condition, the Fe-CO bond can break first while keeping the Fe<sub>3</sub>S unit intact (Fig 2.2b) [131]–[133]; (3) The carbonyl group has been proven to be a clean coordinating group after thermal decomposition because of the formation of gas phase CO[134]–[137]; and (4) iron-sulfur clusters with various stoichiometric ratios can be available with similar coordinating groups and molecular structures[129]. Therefore our synthetic strategy can be readily extended for other stoichiometric iron-sulfide nanostructures, therefore providing an opportunity for future systematic study of the structural and physical properties of the iron-sulfur nano-family.

## *2. Experimental Techniques*

### *2.1 Synthesis of Single-Source Molecular Precursor*

The (OC)<sub>9</sub>(μ-CO)Fe<sub>3</sub>S was synthesized via a modified process[138][139]. The single-source molecular precursors were synthesized using standard air-free Schlenk and glove box techniques. In a typical synthesis, a 150mg of Fe<sub>3</sub>(CO)<sub>12</sub> (#381411, Sigma) was dissolved in 150ml of hexane (#296090, Sigma). The solution was heated to reflux, and 0.05ml of (CH<sub>2</sub>)<sub>2</sub>S (#128252, Sigma) was added. The solution was refluxed under nitrogen for 30mins. Then the mixture was moved into the glovebox. The solvent was removed in vacuum, and the residue was chromatographed by thin layer chromatography, with solvent mixture of CH<sub>2</sub>Cl<sub>2</sub> (#270997, Sigma) and hexane (9:1 volume ratio). This



process yielded in order of elution: reddish brown- $\text{Fe}_3\text{S}_2(\text{CO})_9$ ; green- $\text{Fe}_3(\text{CO})_{12}$ ; brown- $\text{Fe}_3\text{S}(\text{CO})_{10}$ ; The obtained precursors were filtered and dried in vacuum to form needle-shape crystal, whose composition were verified by NMR. In order for synthesis of NPs, the molecular precursor crystals were dissolved in o-dichlorobenzene (DCB) (#240664, Sigma).

Chromatography was run in a 0.5" ID  $\times$  12" L column with Teflon stopcock and fritted disc. Silica gels with particle size (32~63) was purchased from Selecto Scientific Inc. (#152824). The loading method is dry load.

## 2.2 Synthesis of the Fe/S NPs

In a typical synthesis of 7 nm  $\text{Fe}_3\text{S}$  NPs, certain amount of oleylamine was dissolved in DCB as passivation ligands of NPs and the solution was heated up to 150°C under an atmosphere of inert He gas. At 150°C, 1ml 5 mg/ml  $(\text{OC})_9(\mu\text{-CO})\text{Fe}_3\text{S}$  molecules pre-dissolved in DCB was quickly injected into the hot solution, and the reaction continued for 5 minutes and was quickly stopped and cooled down to room temperature (by removing the heating apparatus) to form a black clear suspension. The  $\text{Fe}_3\text{S}$  NPs solid was collected by adding ethanol to the resultant solution, followed by centrifugation at 6000rpm for 20mins. Figure 2.2b shows a typical TEM image of nearly monodispersed spherical 7nm  $\text{Fe}_3\text{S}$  NPs. The NPs powder can be well re-dispersed in various organic solvents such as toluene and is air stable. The 3:1 stoichiometric ratio of as-synthesized NPs was consistently determined by different techniques including EDS, inductively coupled plasma atomic emission spectrometry (for Fe) and combustion (for S) by LECO SC-432DR sulfur analyzer (Galbraith Laboratories, Inc., TN). We also carried out detail

structural characterization by high resolution TEM imaging as well as selected area electron diffraction pattern (SAED). Figure 2.2c reveals the amorphous nature of Fe<sub>3</sub>S NPs synthesized under our current condition, which is consistent with observation of amorphous electron diffraction ring patterns as shown in Figure 2.2d.

<b>Iron-Sulfides</b>	<b>Size (nm)</b>	<b>DCB (ml)</b>	<b>Oleylamine (ml)</b>	<b>Precursors in DCB (ml)</b>	<b>T(°C)</b>	<b>Reaction Time (mins)</b>
Fe <sub>3</sub> S	3	13.81	0.19	1	125	60
	5	13.81	0.19	1	150	5
	7	12.63	0.37	2	150	5
	12	12.63	0.37	2	150	30

Table 2.1. Synthetic conditions for Fe<sub>3</sub>S NPs

The size of Fe<sub>3</sub>S NPs can be monotonically tuned up to 12nm by simply changing the concentration of precursor and reaction time while maintaining stoichiometric ratio. Figure 2.3 shows three more selected sizes of NPs with narrow size distribution. However, for larger sized NPs (>12nm) we always observed phase separation of iron element with clear lattice structures. This observation is consistent with previous report of stoichiometric iron-rich compounds synthesized under extreme condition, showing the size less than 40nm[115].

### *3. Result and Discussion*

Across the board, all the Fe<sub>3</sub>S NPs of various sizes are air stable at room temperature. In comparison with the existing Fe-FeS phase diagram, this stoichiometric iron sulfur compound is supposed to be the intermediate state and can only be grown under extreme conditions, which was far from our current synthetic condition. In order to further

understand the structural evolution, we used 7nm sized Fe<sub>3</sub>S nanoparticles as an example and carried out a more detailed study of a time dependent experiment during the synthesis, as shown in Figure 2.4. We observed that under same 150°C temperature, the crystalline phase starts appearing within NPs at a longer synthetic time, and is accompanied by the change of the EDS ratio because of a continuous increase of non-stoichiometric iron content. Therefore, we concluded that this process corresponds to the breakdown of Fe<sub>3</sub>S NPs and the phase separation between Fe and Fe<sub>3</sub>S. The crystalline phase shown in Figure 2.4 corresponds to either pure iron lattice or iron oxide lattice (we can not make a conclusion at this stage because iron NPs have been shown to oxidize once they are exposed to the air for TEM characterization). This observation is also consistent with our experiment on size control (Fig 2.3), where we have not been able to achieve Fe<sub>3</sub>S NPs with a size greater than 12nm while maintaining stoichiometry.

We carried out size-dependent magnetic property measurements of as-synthesized Fe<sub>3</sub>S NPs by using a superconducting quantum interference device (SQUID), and showed that Fe<sub>3</sub>S NPs behave as superparamagnetic NPs. Figure 2.5 shows the temperature-dependent hysteresis loop measurement of 7nm Fe<sub>3</sub>S NPs. At a low temperature (below the blocking temperature,  $T_B$ ) the Fe<sub>3</sub>S NPs manifest ferromagnetic behavior, whereas they were paramagnetic at room temperature. Zero- field cooling (ZFC) and field cooling (FC) magnetization measurements clearly revealed  $T_B$  for different sized Fe<sub>3</sub>S NPs, as presented in Fig 2.5b. Qualitatively, our observation of monotonically increase of  $T_B$  with the size of Fe<sub>3</sub>S is consistent with theoretical Stoner-Wohlfarth model with linear relationship between NPs volume  $V$  and  $T_B$  as

$$T_B = \frac{KV}{\ln(\tau_m / \tau_0) k_B} \quad (4)$$

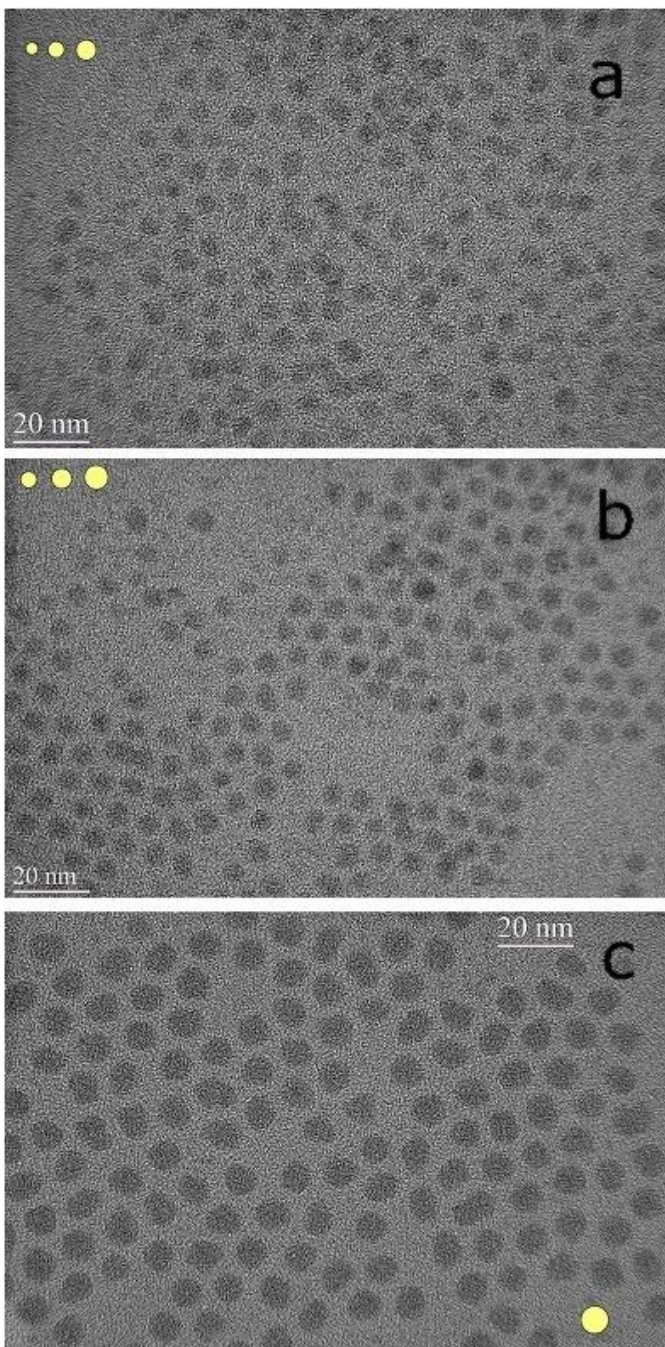


Fig 2.3. Tuning the size of  $\text{Fe}_3\text{S}$  NPs by changing the concentration of precursors and the reaction time. (a) 3nm  $\text{Fe}_3\text{S}$  NPs. (b) 5nm  $\text{Fe}_3\text{S}$  NPs. (c) 7nm  $\text{Fe}_3\text{S}$  NPs. Scale bar for all figures, 20nm.

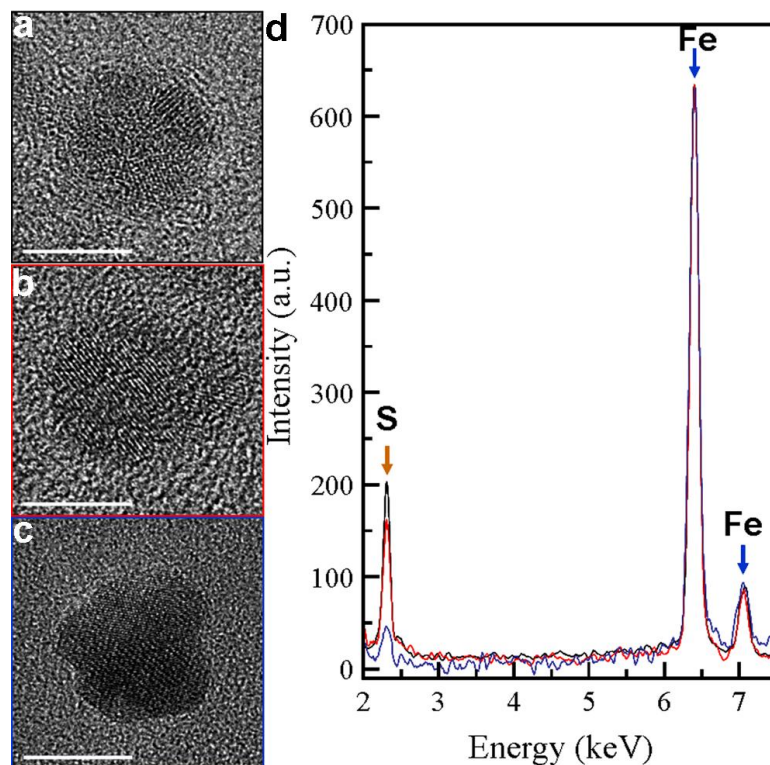


Fig 2.4. The evolution of Fe<sub>3</sub>S NPs with extended reaction time. (a)-(c) Fe<sub>3</sub>S NPs show different crystalline domains. Scale Bar, 10nm. (d) EDS show that Fe:S ratio is 81:19 when the reaction time was extended to 24 hours.

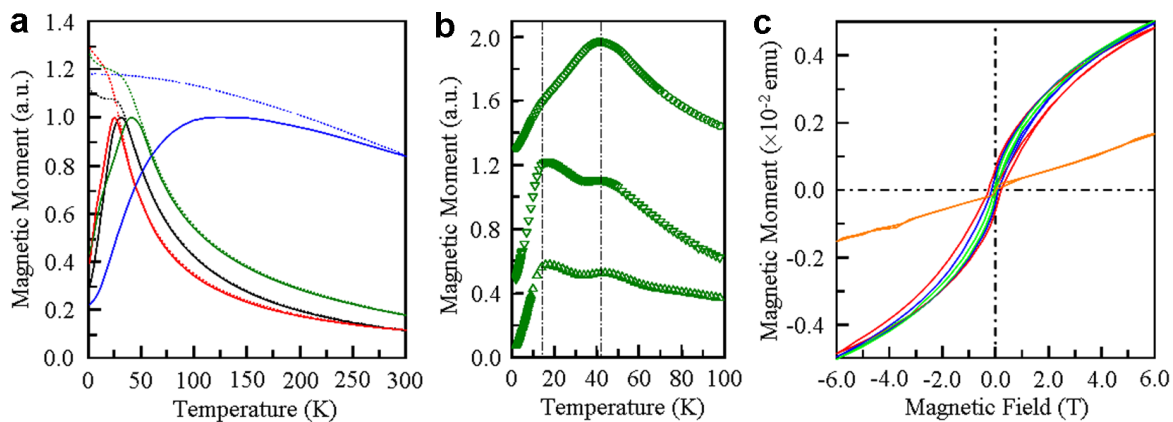


Fig 2.5. Size dependent magnetic property measurements. (a) Field cooling (dashed line) and zero-field cooling (ZFC) (solid line) measurement of Fe<sub>3</sub>S NPs: Blue – 10nm; Green – 7nm; Red – 5nm; Black – 3nm. (b) Novel ZFC feature of 7nm-Fe<sub>3</sub>S NPs. Three curves were obtained from three different 7nm- samples. (c) Hysteresis in 7nm-Fe<sub>3</sub>S NPs: Orange-300K; Green- 10K; Blue-5K; Red -2K.

where  $K$  is the anisotropy constant,  $k_B$  is the Boltzmann's constant,  $\tau_m$  is the measuring time and  $\tau_0$  is a characteristic constant of NPs related to gyromagnetic precession[140]. We also observed the occurrence of  $T_B$  with the variation of size in other magnetic NPs, such as Fe,  $\text{Fe}_3\text{O}_4$  and FePt[98]. However, a more detailed magnetic measurement at low temperature showed intriguing features of  $\text{Fe}_3\text{S}$  NPs. Figure 2.5c shows the ZFC curve of 7nm  $\text{Fe}_3\text{S}$  NPs in the vicinity of  $T_B$ , which reveals another magnetic transition below  $T_B$ . We consistently observed this anomalous feature of two magnetic transitions in NPs of different sizes and did not find them to be dependent on the magnetic field, which thus can be attributed to an intrinsic property of  $\text{Fe}_3\text{S}$  NPs. The similar behavior has been observed from stoichiometric and cation-deficient ( $\text{Fe}_{3-\delta}\text{O}_4$ ) magnetite NPs and it was attributed to the mechanism of a Verwey-type transition (related to metal-insulator transition). However, the nature of the Verwey transition originates from charge disorder of the crystalline lattice[141]–[145]. Considering the amorphous nature of as-synthesized  $\text{Fe}_3\text{S}$  NPs, this mechanism seems unlikely to result in our observation. More experiments (such as frequency dependent ac susceptibility measurements) and theoretical investigation of our stoichiometric  $\text{Fe}_3\text{S}$  is necessary to gain more insight into the physics of two such transition features in amorphous magnetic NPs.

To demonstrate the versatility of our synthetic strategy for such iron-rich stoichiometric NPs, we synthesized another iron- rich NPs,  $\text{Fe}_3\text{S}_2$ , which we also believed to be an intermediate phase and could only exist under extreme conditions[115]. Figure 2.6a shows a molecule model of single molecule precursor applied for the synthesis of  $\text{Fe}_3\text{S}_2$  NPs[138][139]. A typical TEM image of a 10nm  $\text{Fe}_3\text{S}_2$  NPs is shown in Figure 2.6.

The high-resolution TEM images of these stoichiometric NPs also confirm that they have an amorphous structure similar to that of Fe<sub>3</sub>S NPs.

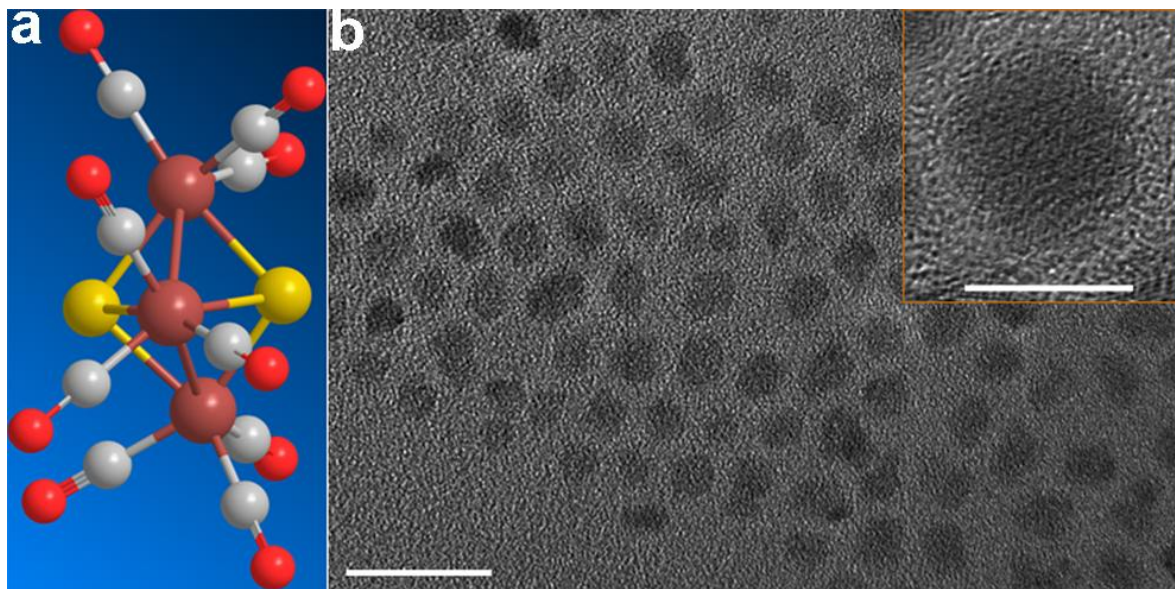


Fig 2.6. The synthesis of Fe<sub>3</sub>S<sub>2</sub> NPs starting from molecular precursors. (a) Left: The molecular structure of (OC)<sub>9</sub>Fe<sub>3</sub>S<sub>2</sub>. Bond lengths are drawn in the ratio based on X-ray data. (b) TEM images of Fe<sub>3</sub>S NPs with 7nm size and good size distribution. Scale bar for the low resolution image, 20nm; the high resolution image, 5nm.

#### 4. Conclusion

In summary, we have synthesized two stoichiometric iron-rich iron sulfide NPs, Fe<sub>3</sub>S and Fe<sub>3</sub>S<sub>2</sub>, by using a single-source molecular precursor approach. Since these two stoichiometric NPs have been previously demonstrated to be intermediate phases and only able exist under extreme condition, the successful synthesis of these two types of NPs under regular laboratory conditions have important implications in a few different research fronts. For example, (1) our synthetic method is very general and can be extended to other stoichiometric iron-sulfur compounds with a tunable Fe/S ratio. This

provides an opportunity for systematical investigation of the evolution of structural and magnetic properties at the nanoscale; (2) both as-synthesized  $\text{Fe}_3\text{S}$  and  $\text{Fe}_3\text{S}_2$  NPs are amorphous magnetic nanostructures that are of considerable interest from both a fundamental and an application point of view. For example, they can offer the opportunity to understand the formation and behavior of spin-clusters, and they are expected to be more effective as catalysis than their nanocrystalline counterparts due to their isotropic disordered structure[146][147]. (3) Our current project represents the first synthesis of these iron-rich stoichiometric iron sulfide NPs under normal synthetic conditions. Availability of these two types of NPs should enable future study of such as phase diagram that otherwise cannot be available. These two iron sulfur NPs have sulfur atoms on their surface which can enable surface functionality better than an oxide surface.



# Chapter III: Modularity Control in Synthesis and Properties of Hybrid Nanooligomers Based on a General Approach

*The Way produced the One; the One produced two; two produced three; and three produced all things.*

*by Lao Tzu*

## *1. Existing Synthetic Schemes*

Several bottom-up schemes exist to achieve different nanooligomer structures of various sizes, quantities and qualities. These schemes make use of the chemical and physical properties of a single subunit to (a) self-organize or self-assemble into some useful conformation, or (b) rely on positional assembly. Such bottom-up schemes are capable of producing nanodevices that are comparable to top-down methods but at a reduced cost. However, the schemes could potentially be overwhelmed as the size and complexity of the desired assembly increases.

### 1.1 Processes based on Toposelective Surface Modification

A simple route to elaborate site-specific nanooligomers is to modify the surface of the precursor particles toposelectively. Such surface modification should be easily introduced and removed without altering the NPs. The modification can either be physical or chemical, for example, by embedding the first material as seeds half immersed in a

medium before laying down the second material, or by chemical modification with ligands to selectively mask portion of the seed's surface.

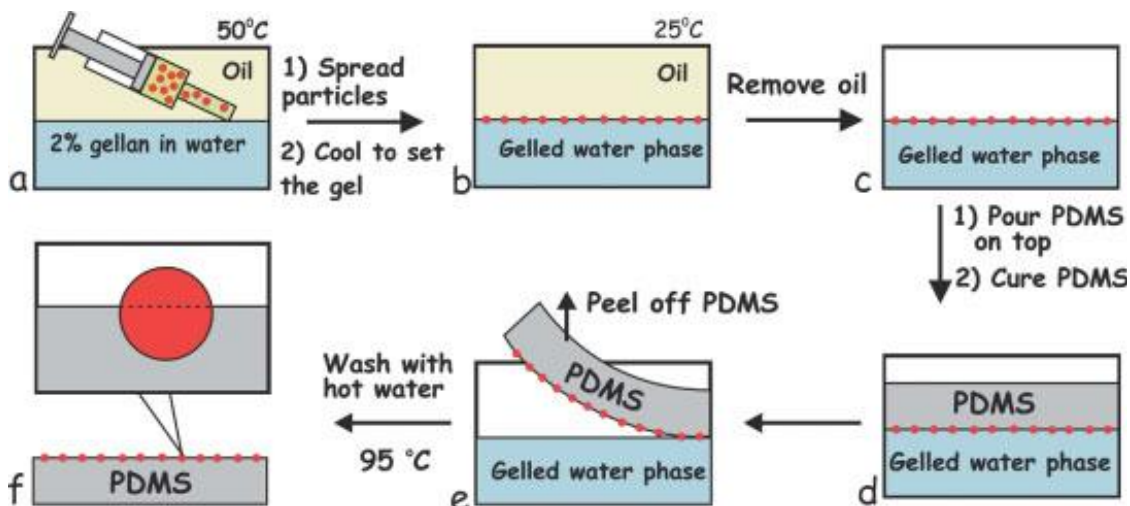


Fig 3.1. Schematics of the gel trapping technique for replicating microparticle monolayers at oil water and the air-water interfaces. Reprinted from Ref. [148].

We cite the experiment of Paunov's group as an example that illustrates this idea[148]. They deployed the gel trapping technique (GTT) to produce Au-Polystyrene (PS) dimers. A colloidal dispersion of PS particles was initially trapped at the interface between a hot aqueous phase and an organic decane phase. They accomplished the physical masking by replacing the organic phase with polydimethylsiloxane (PDMS) oil after solidifying the water solution at room temperature. In two days, they peeled the cured solid PDMS from the gel with the particle monolayer, which once trapped in the gel but was now absorbed onto the elastomer surface (Fig 3.1). They then sputtered Au onto the elastomer surface and mechanically removed the Au-capped PS particles from the substrate (Fig 3.2). Adjusting the surface tension by adding surfactants into the aqueous phase prior to templating with PDMS alters the exposure of PS surface and changes the final amount of Au coating. Paunoy's group claimed that GTT was capable

of acquiring dimers down to 100nm in diameter. However, its major drawback was that it was still far larger than the quantum-size confinement scale for many metal and semiconductor particles[149]. Meanwhile, the requirement of a 2D substrate severely limited the total yield of the product.

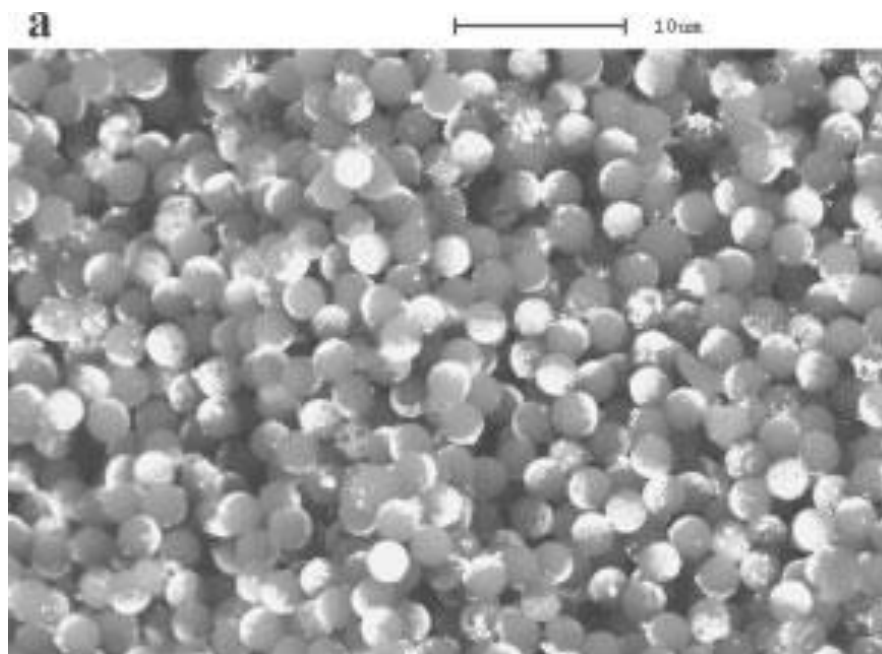


Fig 3.2. SEM images of heterodimer Au-PS NPs. They were fabricated by gold sputtering on a monolayer of 2.7 $\mu$ m sulfate PS latex particles embedded on the surface of PDMS. Reprinted from Ref.[148].

The emulsion-based route is typically used for chemical modification on the surface of precursor seeds. The synthesis of snowman-like nanodimers of Fe<sub>3</sub>O<sub>4</sub>-Ag (Fig 3.3) has been reported[150]. Before the addition of AgNO<sub>3</sub>, a precursor of Ag, the Fe<sub>3</sub>O<sub>4</sub> NPs were surrounded by fatty amine molecules that stabilized the NPs in the non-polar organic phase. Ultrasonic emulsification created a microemulsion environment where Fe<sub>3</sub>O<sub>4</sub> was outside the organic droplets, facing the aqueous phase with the capping ligands extending in the opposite direction. The initial Ag deposition occurred at the imperfect capping sites of

$\text{Fe}_3\text{O}_4$ , which further served as nucleation sites for subsequent anisotropic Ag growth. Though this method was more successful than the physical method in terms of the NP size, the growing complexity of the surface conditions at different domains makes this method unsuitable when dealing with an increase in the number of modules of nanooligomers.

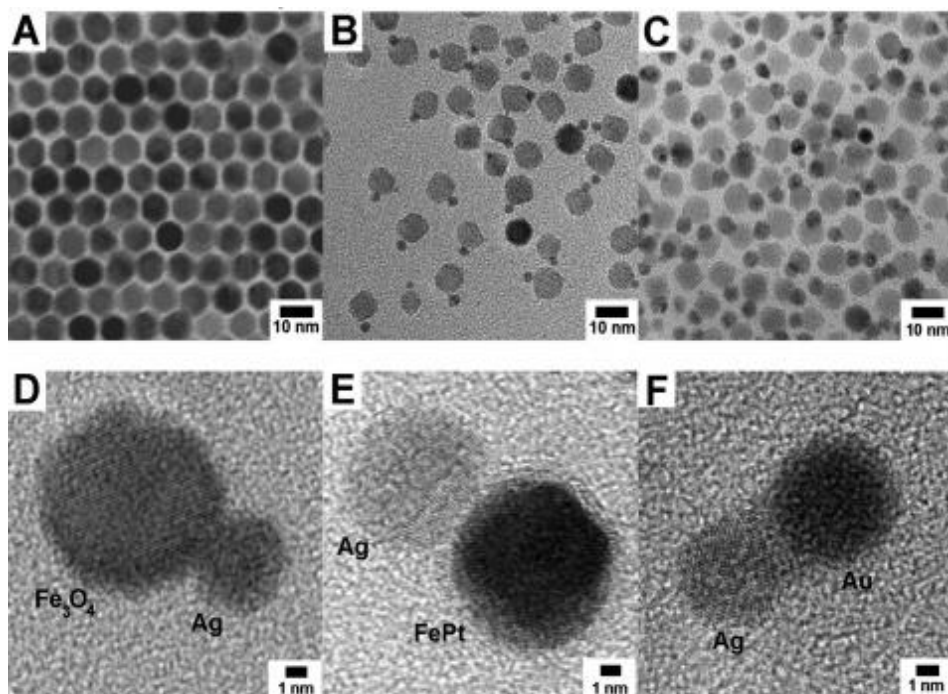


Fig 3.3. TEM images of different nanodimers acquired by the emulsion-based scheme. (A)/ (D)  $\text{Fe}_3\text{O}_4$  NPs; (B) /(E)  $\text{FePt-Ag}$  NPs; (C)/(F)  $\text{Ag-Au}$ . Reprinted from Ref.[150].

## 1.2 Processes Based on Controlled Phase Separation

The second method that has been extensively used yields nanooligomers with smaller size and good size distribution. The phase separation method does not aim for a hetero structure at the beginning but instead, aspires to an alternative medium, like an isotropic core-shell structure or a uniform alloy NP. Usually, the core-shell structure is not favorable when it comes to minimum energy because of the substantial strain that

develops at the boundary if neighboring materials do not have similar lattice constants[151] [152]. Excess energy, either from an exothermic chemical reaction or the thermal environment, forces one of the materials to undergo a dewetting process to reach a heterostructure. M. Giersig has demonstrated how to get AgI-Silica nanodimers by exposing the Ag-silica core-shell NPs to  $I_2$  (Fig 3.4) [153]. The diffusion of iodine atoms through the porous silica to combine with the Ag core occurred first, followed by the building of ion channels loaded with  $Ag^+$  and  $I^-$ . The chemical potential in this reaction further drove Ag atoms through these channels to the surface of the silica to react with  $I_2$ . When the Ag core was depleted, a nanodimer composed of an AgI domain and hollow silica emerged. Another example started with the Ag/Au alloy[154]. The oxidization of Ag occurred slowly when it was exposed to the atmosphere. A thin layer of  $Ag_xO$  first appeared and then gradually grew. Eventually, the  $Ag_xO$  evolved into a bulk, with a neck from the Ag/Au alloy due to Rayleigh instability[155]. The Rayleigh instability treated  $Ag_xO$  as liquid, by virtue of the surface tension, to minimize the surface area into a neck. The major problem with this method appears when we start from a core-shell structure of two materials with large size differences. A thin shell outside a thick core will segregate at different sites on the core, while a thick shell on a small core prevents phase separation from occurring because the small interface energy cannot match the large lattice energy of the shell alone. For the alloy alternative, the fact that few materials can form a miscible binary system hinders formation. Lastly, the loss of materials through material decomposition or stripping is a frequent occurrence during the delicate reaction[156].

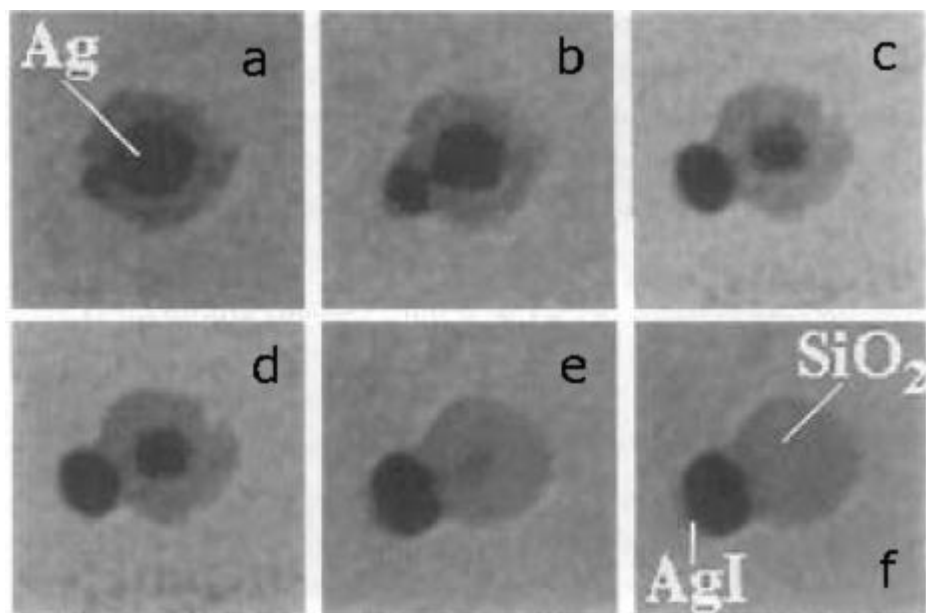


Fig 3.4. TEM images of evolution of a single Ag@SiO<sub>2</sub> core-shell NP to a AgI-SiO<sub>2</sub> nanodimer. (a) Ag@SiO<sub>2</sub> core-shell structure. (b)-(e) The evolution from a core-shell NP to a nanodimer when Ag@SiO<sub>2</sub> was exposed to I<sub>2</sub>. (f) Ag-SiO<sub>2</sub> nanodimer. Reprinted from Ref. [153].

### 1.3 Processes Based on Controlled Surface Nucleation

The most commonly exploited mechanism is the epitaxial growth of one material on the surface of another, a process dependent on the conditions of the nucleation and growth of the second material. The growth is facilitated by the intrinsic incompatibility of the crystal lattices of the two materials, which inhibits them from forming a stable core-shell structure. The conditions leading to homogeneous nucleation can be avoided by reducing the temperature at which the second material is nucleated, since homogenous nucleation may dominate at high temperatures.

When two materials join together, the lattices of both relax into an identical orientation[157] or they form a preferential orientation between themselves. One current

theory of the epitaxial growth is Coincidence-Site-Lattice theory (CSL) [158]. It explains the crystallographic relationships often found at grain boundaries, twins and the general interface between two different crystalline solids. “Coincidence Site Lattice” refers to a superstructure that, in specific orientations, some lattice points of one lattice coincide with lattice points of the other. It assumes a maximum coincidence between the lattice points of the two structures on the interface occurring at the lowest interfacial energy. This theory can further predict whether a second material with another type of lattice can grow with its relative orientation at the interfacial plane being the best fit among the lattice points of the two structures.

An example of a heterodimer that can be grown by this method is  $\text{Fe}_3\text{O}_4$  onto the Au NPs (Fig 3.5) [86]. Pre-made Au NPs were mixed with  $\text{Fe}(\text{CO})_5$  in a 1-octadecene (ODE) solvent in the presence of oleic acid (OA) and oleylamine(Oly) and heated to reflux in air. The fresh Fe domains were extremely sensitive to  $\text{O}_2$  and spontaneously oxidized to  $\text{Fe}_3\text{O}_4$ . The high- resolution images in Figure 3.5 reveal that the preferential orientation of  $\text{Fe}_3\text{O}_4$  to Au is almost 0 degrees between  $\{111\}$  facets of both. This is exactly what the CSL theory predicts, if we notice that the lattice constant of  $\{111\}$  from  $\text{Fe}_3\text{O}_4$  is almost the twice of that of Au’s  $\{111\}$ . In other words, every  $\text{Fe}_3\text{O}_4$  unit cell on the boundary has two corresponding Au cells.

The most rewarding aspect of this method is its potential to include more components [159]–[161]. Therefore, we found it to be the best candidate for producing nanooligomers. Scientists have developed three modules and more than four modules in this way. Nevertheless, this method does have significant limitations in the choice of

materials. Self-nucleation of the second material or nucleation on multiple sites on the seeds can often lead to problems[162].

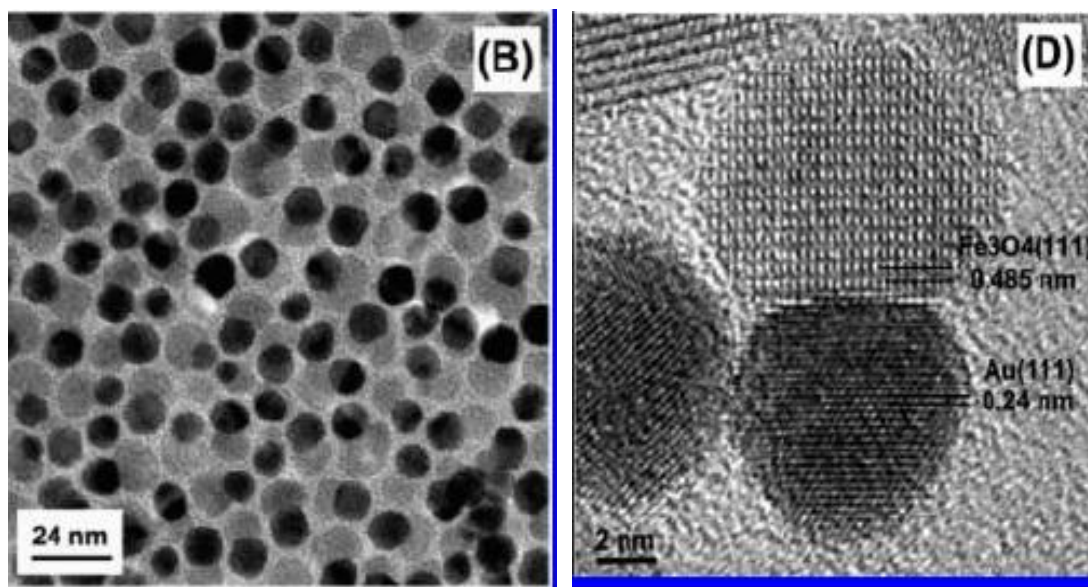


Fig 3.5. Dumbbell-like Au-Fe<sub>3</sub>O<sub>4</sub> NPs: (B) TEM images of the 8-14 nm Au-Fe<sub>3</sub>O<sub>4</sub> NP (D) A HRTEM image of one 8-12 nm Au-Fe<sub>3</sub>O<sub>4</sub> NP. Reprinted from Ref. [86].

## 2. Novel Chemical Synthetic Approach of Bottom-up Method

We chose a systematic bottom-up approach that achieved precise modularity control over the hybrid nanooligomers by depositing Ag on the seed NPs as the foundation for the modules. This approach requires arranging smaller modules into more complex assemblies. It is superior to top-down approaches, i.e., the conventional solid-state silicon method[163], in overall yield, flexibility in the choice of seed and the synthesis requirements. We based our choice of Ag on its well-known properties, including its ability to grow epitaxially onto a variety of materials[164], its galvanic replacement by the ions of other metals[165]–[167], and its reaction with chalcogens followed by cation exchange[168]. These are in addition to its properties in opto-electronic devices, chemical and biological sensing[169], and surface-enhanced Raman scattering (SERS)



detection[170]. Zhang published his pioneering work on the role of Ag in the nonepitaxial growth of hybrid isotropic core-shell nanostructures[171]. We have improved this method to create anisotropic modules in an organized structure regardless of whether or not the initial Ag growth on seed NPs is homogenous. Meanwhile, the lattice constants are not dependent on the structure of the seed NPs. Thus, we were able to circumvent the limitations imposed by epitaxial strategies. It enabled us to organize seeds and modules of semiconductors, catalysts, LSPR metals, and ferromagnetic materials into desired patterns. Monocrystalline features were also a concern. The absence of structure defects gives monocrystals unique optical and electrical properties. Our novel approach is illustrated in the flowchart in Figure 3.6 and outlined as follows:

- (1) Ag is deposited on seed NPs epitaxially via a colloid chemistry method, either isotropically or anisotropically.
- (2) Coated Ag can be partially replaced by metal ions via a galvanic reaction to form a metal/Ag alloy, or react with a chalcogen source to form silver chalcogenide, followed by a cation exchange process to obtain the desired semiconductor compound.
- (3) Additional Ag can be selectively deposited on the unoccupied surface of seed NPs to form the foundation for another module.

This approach maintains the advantages of controlled surface nucleation, mainly the tunability over the module size, while simultaneously avoiding the search for specific nucleation conditions for the different module materials on the seed NPs. It utilizes only one phase, eliminating ligand choice problems, which are common in the emulsion method.

The following sections focus on the Au-CdSe, Pt-CdS, Pt-CdS-CdSe, and Pt-Ag/Au-CdSe-Ag<sub>2</sub>Se examples and the details of the synthesis and characterization procedures.

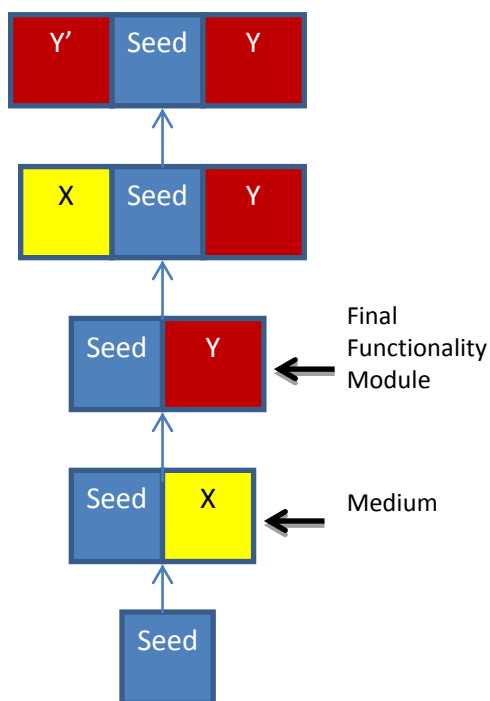


Fig 3.6. Flowchart of the bottom-up method to build a complex nanooligomers starting from a single seed.

### 3. Experimental Section

#### 3.1 Chemicals

Myristyltrimethylammonium bromide (TTAB,  $\text{CH}_3(\text{CH}_2)_{13}\text{N}(\text{Br})(\text{CH}_3)_3$ , 99+%), 1,2,3,4-Tetrahydronaphthalene (Tetralin,  $\text{C}_{10}\text{H}_{12}$ , anhydrous, 99+%), Borane-*tert*-butylamine complex ( $(\text{CH}_3)_3\text{CNH}_2 \cdot \text{BH}_3$ , 97%), Cadmium nitride tetrahydrate ( $\text{Cd}(\text{NO}_3)_2 \cdot 4\text{H}_2\text{O}$ , 99.999%), Silver nitrate ( $\text{AgNO}_3$ , 99+%), Gold(III) chloride trihydrate ( $\text{HAuCl}_4 \cdot 3\text{H}_2\text{O}$ , 99.9+%), Zinc nitrate hexahydrate ( $\text{Zn}(\text{NO}_3)_2 \cdot 6\text{H}_2\text{O}$ , 98%), Potassium hexachloro-platinate(IV) ( $\text{K}_2\text{PtCl}_6$ , 98+%), Lead(II) nitrate ( $\text{Pb}(\text{NO}_3)_2$ ,

99.0+%), Sulfur (S, reagent grade, -100 mesh particle size, powder), Selenium (Se, powder, -100 mesh, 99.5+%), Potassium cyanide (KCN, 97+%), Oleic acid (OA, technical grade, 90%), Tributylphosphine (TBP, 97%), Sodium borohydride (NaBH<sub>4</sub>, 99.99%), *L*-Ascorbic acid (AA, 99%), Toluene (anhydrous, 99.8%), Methanol (anhydrous, 99.8%), Ethanol (anhydrous, 99.5+%) were purchased from Sigma-Aldrich. Methylene Blue hydrate (MB, C<sub>16</sub>H<sub>18</sub>ClN<sub>3</sub>S•xH<sub>2</sub>O 96+%) and Oleylamine (OAm, C<sub>18</sub>H<sub>37</sub>N, approximate C<sub>18</sub> content 80-90%) were purchased from Acros.

All above chemicals were used as received without further processing. The preparation of S-precursor and Se-precursor mainly followed recipes provided in Zhang's publication[171]. Depending on specific reaction environment, for certain systems in current report a second type of Se-precursor was also used and prepared by the following procedure: 1mmol of Se powder was placed in a vial and a few drops of acetone were added. The mixture was dried naturally to form a solidified Se layer in the bottom of the vial. 1mmol of NaBH<sub>4</sub> was then carefully added to the top of Se layer, followed by a careful slow injection of 1.5ml icy deionized H<sub>2</sub>O. The vial was sealed by parafilm and a small hole was punched to release H<sub>2</sub> gas that was generated during the reaction. After 1hrs, the top clear solution was carefully transferred to 50ml of oxygen-free icy deionized H<sub>2</sub>O (by flow of N<sub>2</sub> gas) and mixed homogenously in a few seconds.

Deionized water (H<sub>2</sub>O) was obtained by using Barnstead NANOPure water purification system, having a resistivity of 18.3 MΩ-cm. All aqueous solutions were prepared in the deionized water.

## 3.2 Experimental Methods

### 3.2.1 Synthesis of Au nanoparticles with various sizes

Synthesis of Au NPs was modified from the published method[172]. In a typical synthesis of 7nm Au NPs, an orange precursor solution consisting of tetralin (10.00ml), oleylamine (10.00ml), and HAuCl<sub>4</sub> (0.1000g) was prepared in air at room temperature (~22 °C), and was stirred under N<sub>2</sub> gas flow for 10mins in a 50ml flask. A reducing solution containing 0.5000mmol of tert-butylamine-borane complex, 1.00ml of tetralin, and 1.00ml of oleylamine was mixed by sonication, pre-cooled by icy water and injected into the precursor solution at ~2°C. The solution color changed from yellow to dark purple within 5mins. The reaction lasted for 30mins before the temperature was raised back to the room temperature. The whole solution was mixed with 80ml acetone and was centrifuged at 8000rpm for 10mins. After being washed and centrifuged, the precipitate was dissolved in 40ml of hexane.

In a typical synthesis of 10nm Au nanoparticles, 28.0mg of HAuCl<sub>4</sub>, 0.70ml of oleylamine and 0.60ml of toluene were mixed and heated at 60°C for 12mins. Gradual color fading from initial orange color could be observed during this process. The solution was then injected into a boiling mixture of 1.50ml of oleylamine and 25.00ml of toluene at 130°C for 30mins without stirring. The final product was obtained by addition of ethanol (1:5 volume ratio), followed by centrifugation at 4000rpm for 20mins. The precipitate was re-dispersed in 5.00ml of toluene that could be used as Au NPs stock solution.

### 3.2.2 Synthesis of Au-Ag core-shell nanoparticles with various ratio of Au/Ag

In a typical synthesis, 0.50ml of 7nm Au stock solution in toluene was mixed with 6.50ml of toluene, 0.20ml of oleylamine and 1.00ml of AgNO<sub>3</sub> solution (10mg/ml in methanol) in an 8ml glass vial. The mixture was heated in an oil bath to 46°C and stayed at this temperature without stirring for a few hours to get different Au/Ag ratio (for example, 4hrs for 1:1 molar ratio of Au/Ag, and 8hrs for 1:2 molar ratio of Au/Ag). After the reaction the solution was mixed with ethanol with volume ratio of 1:7, followed by centrifugation at 4000rpm for 10mins. The precipitate was re-dissolved in 5ml of toluene.

### 3.2.3 Synthesis of Au-Ag<sub>2</sub>Se and Au-Ag<sub>2</sub>S heterodimers

In a typical synthesis of Au-Ag<sub>2</sub>Se heterodimers, 1ml of oleylamine was firstly added to 5.00ml of the Au-Ag core-shell nanoparticles (in toluene) in a 50ml flask. The solution was kept at 130°C in the air and 1.00ml of Se-precursor was swiftly added in 1min. The reaction lasted for 270s before the flask was removed from the oil bath and was cooled down to room temperature rapidly. Then methanol with 1:9 volume ratio was added and the whole solution was centrifuged at 3800 rpm for 20mins. The precipitate was re-dissolved in 5ml of toluene. Acetone with 1:9 volume ratio was further used and the solution was centrifuged again for the second time. The final product was dispersed in 5.00ml of toluene.

In a typical synthesis of Au-Ag<sub>2</sub>S heterodimers, 1.00ml of oleylamine was added to 5.00ml of Au-Ag core-shell stock solution (in toluene) in a 50ml flask. The solution was kept at 100°C in the air and 1.00ml of S-precursor was swiftly added in 1min. The reaction lasted for 180s before the flask was removed from the oil bath and was cooled

down to the room temperature rapidly. Methanol with 1:9 volume ratio was added, followed by centrifugation at 3800rpm for 20mins. The precipitate was dissolved in 5ml of toluene.

### 3.2.4 Synthesis of Au-CdSe, Au-CdS, Au-PbSe and Au-ZnS heterodimers

*Au-CdSe heterodimers:* 5ml of Au-Ag<sub>2</sub>Se solution in toluene was mixed with 0.20ml of oleylamine and 0.10ml of oleic acid. The mixture was degassed by N<sub>2</sub> gas flow in a three-neck flask for 30mins. Then 1.00ml of Cd(NO<sub>3</sub>)<sub>2</sub> solution in methanol (25.0mg/ml) was added into the mixture at 50°C, followed by addition of 0.012ml of TBP. The color changed rapidly from brown to purple within a few minutes. The reaction lasted for 1hr before the solution was cooled down to room temperature. The product was obtained by adding a 4:4 volume ratio of methanol/ethanol mixture, followed by centrifugation at 3500rpm for 10mins. The precipitate was dissolved in 5ml of toluene.

*Au-CdS heterodimers:* 5ml of Au-Ag<sub>2</sub>S solution in toluene was mixed with 0.20ml of oleylamine and 0.10ml of oleic acid. The mixture was degassed by N<sub>2</sub> gas flow in a three-neck flask for 30mins. Then 1.00ml of Cd(NO<sub>3</sub>)<sub>2</sub> solution in methanol (25.0mg/ml) was added at 50°C, followed by addition of 0.012ml of TBP. The reaction lasted for 1hr before the solution was cooled down to room temperature. The product was obtained by addition of a 4:4 volume ratio of methanol/ethanol mixture, followed by centrifugation at 3500rpm for 10mins. The precipitate was dissolved in 5ml of toluene.

*Au-PbSe heterodimers:* 5ml of Au-Ag<sub>2</sub>Se solution in toluene was mixed with 0.10ml of oleylamine and 0.05mL of oleic acid. The mixture was degassed by N<sub>2</sub> gas flow in a three-neck flask for 30mins. Then 1.00ml of saturated Pb(NO<sub>3</sub>)<sub>2</sub> solution in methanol was

added at room temperature, followed by injection of 0.02ml of TBP. The reaction lasted for 1hr. The product was obtained by addition of a 4:4 volume ratio of methanol/ethanol mixture, followed by centrifugation at 3500rpm for 10mins. The precipitate was dissolved in 5ml of toluene.

*Au-ZnS heterodimers:* 5.00ml of Au-Ag<sub>2</sub>S solution in toluene was mixed with 0.2ml of oleylamine and 0.1ml of oleic acid. The mixture was degassed by N<sub>2</sub> gas flow in a three-neck flask for 30mins. Then 1ml of Zn(NO<sub>3</sub>)<sub>2</sub> solution in methanol (25.00mg/ml) was added at 63°C, followed by addition of 0.02ml of TBP. The reaction lasted for 10hrs before the solution was cooled down to room temperature. The product was obtained by addition of 4:4 volume ratio of methanol/ethanol mixture, followed by centrifugation at 3500rpm for 10mins. The precipitate was dissolved in 5ml of toluene.

### 3.2.5 Synthesis of FePt-CdSe heterodimers

*FePt nanoparticles:* A formerly published method was followed to prepare FePt NPs that were dispersed in hexane[173]. In a typical synthesis, 0.500mmol of Pt(acac)<sub>2</sub>, 10.00ml of benzylether and 5.00ml of octadecene were mixed in a three-neck flask and stirred. The mixture was heated under a flow of nitrogen gas to 60°C to ensure dissolution of Pt(acac)<sub>2</sub>. The mixture solution was then heated to 120°C and the flask was kept under protection of nitrogen gas. 2.000mmol of Fe(CO)<sub>5</sub> and 5.00mmol of oleic acid were added, followed by addition of 5.00mmol of oleylamine after 5mins. The whole mixture solution was then heated to 205°C and incubated at this temperature for 2hrs. The black solution was then cooled down to room temperature. The FePt nanocubes were obtained and cleaned by centrifugation with addition of ethanol (1:2 volume ratio). The

product was re-dispersed in 20.00ml of hexane in the presence of a few drops of oleic acid and oleylamine.

*FePt-Ag dimers:* 0.50ml of FePt NPs in hexane was mixed with 1.00ml of AgNO<sub>3</sub> solution in methanol (5.00mg/ml), 7.00ml of toluene and 0.20ml of oleylamine at 52°C without stirring for 12hrs. The product was obtained by addition of 1:5 volume ratio of methanol:ethanol mixture, followed by centrifugation at 3000rpm for 10mins. The FePt-Ag core-shell nanoparticles could be dispersed in toluene.

*FePt-Ag<sub>2</sub>Se heterodimers:* 0.40ml of Se-precursor was injected into FePt-Ag core-shell nanoparticles in 10.00ml of toluene under stirring for 45mins. The product was obtained by addition of 5 times of ethanol (volume ratio), followed by centrifugation at 3500rpm for 10mins. The product was dispersed in toluene.

*FePt-CdSe heterodimers:* The FePt-Ag<sub>2</sub>Se heterodimers was mixed with 1.00ml of Cd(NO<sub>3</sub>)<sub>2</sub> solution in methanol (25.00mg/mL), 0.10ml of oleylamine and 0.05ml of oleic acid at 50°C, followed by injection of 0.02ml of TBP. The reaction lasted for 30mins. The product was obtained by addition of 1:4 volume ratio of methanol/ethanol mixture, followed by centrifugation at 3500rpm for 10mins. The product was dispersed in toluene.

### 3.2.6 Synthesis of Pt nanocubes

Synthetic procedure of Pt nanocubes was modified from the published method[174]. In a typical synthesis, 2.00ml of K<sub>2</sub>PtCl<sub>6</sub> aqueous solution (0.010M) was mixed with 0.672g of TTAB and 17.00ml of deionized H<sub>2</sub>O in a flask before the mixture was heated up to 50°C. Then 1.50ml of icy NaBH<sub>4</sub>/H<sub>2</sub>O solution (0.4M) was added into the mixture and the flask was sealed by a rubber stopper with a needle penetrated through to vent H<sub>2</sub>



gas that was generated during the reaction (the needle was removed after 10mins). The solution was then kept at 50°C for another 12hrs~16hrs. The solution was centrifuged at 8500rpm for 20mins. The precipitate was then re-dissolved in 10.00ml of deionized H<sub>2</sub>O. The solution was centrifuged again for the second time at 1000rpm for 10mins to get rid of some messy clusters/aggregation of Pt before the growth of Ag.

### 3.2.7 Synthesis of Pt-Ag dimers with controlled spatial arrangement

*One-sided Pt-Ag dimers:* Pt nanocubes in 10.00ml of deionized H<sub>2</sub>O was mixed with 13.00ml of deionized H<sub>2</sub>O, 1.00ml of TTAB aqueous solution (0.200M) and 1.00ml of AgNO<sub>3</sub> aqueous solution (0.010M) in a 50ml flask, and then was immersed in an oil bath at 70°C under magnetic stirring for 20mins before addition of 1.00ml of AA (0.800M). The solution showed whitish cloudy at the beginning due to the formation of Ag/TTAB complex but turned to a clear solution after 40mins. The reaction was stopped after 1hr with a reddish brown color. The solution was cooled down by icy water, followed by centrifugation at 8000rpm for 15mins. The top solution was carefully sipped out by pipette and the cloudy precipitate was dissolved in 10.00ml of deionized H<sub>2</sub>O.

*Two-sided Pt-Ag dimers:* Pt nanocubes in 10.00ml of deionized H<sub>2</sub>O was mixed with 13.00ml of H<sub>2</sub>O, 1.00ml of TTAB aqueous solution (0.200M) and 1.00ml of AgNO<sub>3</sub> aqueous solution (0.010M) in a 50mL flask, and then was immersed in an oil bath at 70°C under magnetic stirring for 20mins before addition of 1.00ml of AA (0.800M). The solution showed whitish cloudy at the beginning due to the formation of Ag/TTAB complex but turned into a clear solution after 40mins. The reaction was stopped after 150mins with a reddish brown color. The solution was cooled down by ice water,

followed by centrifugation at 8000rpm for 15mins. The top solution was carefully sipped out by pipette and the cloudy precipitate was dissolved in 10ml of deionized H<sub>2</sub>O.

*Three-sided Pt-Ag dimers:* Pt nanocubes in 10.00ml of deionized H<sub>2</sub>O was mixed with 13.00ml of deionized H<sub>2</sub>O, 1.00ml of TTAB aqueous solution (0.200M) and 1.00ml of AgNO<sub>3</sub> aqueous solution (0.010M) in a 50mL flask, and then was immersed in an oil bath at 70°C under magnetic stirring for 20mins before addition of 1.20ml of AA (0.800M). The solution showed whitish cloudy at the beginning due to the formation of Ag/TTAB complex but turned into a clear solution after 40mins. The reaction was stopped after 180mins with a reddish brown color. The solution was cooled down by icy water, followed by centrifugation at 8000rpm for 15mins. The top solution was carefully sipped out by pipette and the cloudy precipitate was dissolved in 10ml of deionized water.

### 3.2.8 Synthesis of Pt-Ag<sub>2</sub>S, Pt-PbS, Pt-ZnS and Pt-CdS heterodimers

*Pt-Ag<sub>2</sub>S heterodimers:* The Pt-Ag dimers in 5.00ml of deionized H<sub>2</sub>O was mixed with 10.00ml of acetone and 0.60ml of decanethiol in acetone (10%), followed by a fast injection of 4.00ml of S-precursor solution at 60°C. The reaction was kept under vigorous stirring for 2hrs before it was stopped. The solution was then sonicated for 40mins to help dispersion of Pt-Ag<sub>2</sub>S into the organic phase. The aqueous phase in the bottom was carefully sipped out by pipette, and the top organic solution was collected and centrifuged with 1:2 volume ratio of ethanol mixture at 3000rpm for 20mins. The precipitate was re-dispersed in 5.00ml of toluene.

*Pt-PbS heterodimers:* The Pt-Ag<sub>2</sub>S heterodimers in 5.00ml of toluene was mixed with 1ml of saturated Pb(NO<sub>3</sub>)<sub>2</sub> solution in methanol, 0.30ml of oleylamine and 0.15ml of oleic acid under N<sub>2</sub> gas flow at 50°C, followed by addition of 0.02ml of TBP. The cation exchange reaction lasted for 1hr. The product was obtained by addition of 5 times of methanol and 5 times of ethanol in volume, followed by centrifugation at 2000rpm for 10mins. The final product was dispersed in toluene.

*Pt-ZnS heterodimers:* The Pt-Ag<sub>2</sub>S heterodimers in 5ml of toluene was mixed with 1.00ml of Zn(NO<sub>3</sub>)<sub>2</sub> solution in methanol (25.00mg/ml), 0.20ml of oleylamine and 0.10ml of oleic acid under N<sub>2</sub> gas flow at 80°C, followed by addition of 0.02ml of TBP. The cation exchange reaction lasted for 10hrs. After the solution was cooled down to room temperature, it was cleaned by addition of 2 times of ethanol in volume, followed by centrifugation at 3000rpm for 10mins. The final product was re-dispersed in 5ml of toluene. The cation exchange reaction was carried out for the second time under the same condition except that the reaction time was extended to 20hrs. The final product was re-dispersed in toluene.

*Pt-CdS heterodimers:* The Pt-Ag<sub>2</sub>S dimers in 5ml of toluene was mixed with 1.00ml of Cd(NO<sub>3</sub>)<sub>2</sub> solution in methanol (25.00mg/ml), 0.20ml of oleylamine and 0.10ml of oleic acid under N<sub>2</sub> gas flow at 50°C, followed by addition of 0.02ml of TBP. The cation exchange reaction lasted for 1hr. After the solution was cooled down to room temperature, the product was obtained by addition of 5 times of methanol and 5 times of ethanol in volume, followed by centrifugation at 3000rpm for 10mins. The final product was re-dispersed in toluene.

### 3.2.9 Synthesis of Pt-Ag<sub>2</sub>Se heterodimers

Se-precursor prepared by the second method was applied here. Typically, the Pt-Ag dimers was diluted by 20.00ml of deionized H<sub>2</sub>O and 1.00ml of TTAB aqueous solution (0.200M) was added as extra capping ligand at 70°C under continuous stirring. 0.325ml of freshly prepared Se-precursor was added to the solution under N<sub>2</sub> gas protection for 20mins. The solution was cooled down rapidly, and was centrifuged at 7500rpm for 20mins. The final product was dispersed in 20.00ml of deionized H<sub>2</sub>O.

We noticed that unoccupied Pt facets might be contaminated due to the addition of Se precursor. Therefore, in order to expose fresh Pt facets for continual growth of subunits in a nanooligomer surface cleaning procedure could help. For example, the Pt-Ag<sub>2</sub>Se heterodimers solution was added into a mixture of 10.00ml of deionized H<sub>2</sub>O and 0.50ml of TTAB (0.200M), and was kept stirring for 5mins. A 0.064-0.080ml of KCN aqueous solution (0.050M) was added into the solution of Pt-Ag<sub>2</sub>Se. After 30hrs, the solution was centrifuged at 7000rpm for 15mins. The final product was re-dispersed in deionized H<sub>2</sub>O and should be ready for continual growth of subunits.

### 3.2.10 Synthesis of Pt-Au<sub>x</sub>Ag<sub>y</sub>-CdSe nanooligomers

Synthesis of this type of nanooligomers always started with the Pt-Ag<sub>2</sub>Se heterodimers in *Section 3.2.10* and followed the synthetic scheme illustrated in the Figure 3.12 in the main text.

*Pt-Ag-Ag<sub>2</sub>Se nanooligomers:* The Pt-Ag<sub>2</sub>Se heterodimers in 5.00ml of deionized H<sub>2</sub>O was mixed with 0.20ml of TTAB (0.200M) and 0.3ml of AgNO<sub>3</sub> aqueous solution (0.010M). The solution was kept at 70°C under stirring for 20mins before addition of

0.20ml of AA aqueous solution (0.800M). The reaction typically lasted for 2-10hrs, depending on the targeted size of Ag inter-medium NPs. The appearance of a dark brown color typically indicated successful growth of inter-medium Ag NPs onto the Pt-Ag<sub>2</sub>Se heterodimers. After reaction, the solution was diluted by 10.00ml of deionized H<sub>2</sub>O, and was then centrifuged at 7000rpm for 15mins. The top solution was discarded, and the precipitate was re-dispersed in 5.00ml of deionized H<sub>2</sub>O.

*Pt-Ag-CdSe nanooligomers:* The Pt-Ag-Ag<sub>2</sub>Se nanooligomers in 5.00ml of deionized H<sub>2</sub>O was mixed with 0.20 ml of TTAB aqueous solution (0.200M) and was degassed by N<sub>2</sub> gas flow in a three-neck flask for 30mins. 1.00ml of Cd(NO<sub>3</sub>)<sub>2</sub> solution in methanol (25.00mg/ml) was added at 60°C, followed by injection of 0.006ml of TBP. The reaction lasted for 15hrs before the solution was cooled down to room temperature. The product was obtained by addition of 10.00ml of deionized H<sub>2</sub>O, followed by centrifugation at 7000rpm for 15mins. The final product was re-dispersed in 5.00ml of deionized H<sub>2</sub>O.

*Pt-Au<sub>0.21</sub>Ag<sub>0.79</sub>-CdSe nanooligomers:* The Pt-Ag-Ag<sub>2</sub>Se nanooligomers (with Ag growth time of 7hrs) in 5.00ml of deionized H<sub>2</sub>O was mixed with 4.00ml of TTAB aqueous solution (0.200M) and 0.275ml of HAuCl<sub>4</sub> solution (1.00mg/ml). The reaction was kept at the room temperature for 6hrs under mild stirring. The product was cleaned by centrifugation at 7000rpm for 15mins. The top clear aqueous solution was removed as much as possible, and the residue was collected. 6.00ml of toluene and 2.00ml of acetone were added into the residue, followed by addition of 0.60ml of decanethiol solution in acetone (10%). With the assistance of sonication for 30mins the Pt-Au<sub>0.21</sub>Ag<sub>0.79</sub>-Ag<sub>2</sub>Se was dissolved to form a uniform phase. 0.30ml of oleylamine and 0.15ml of oleic acid were then added, followed by sonication for another 30mins. After that, ethanol was

added with volume ratio of 1:2, followed by centrifugation at 3000rpm for 20mins. The precipitate was re-dispersed in toluene.

With the assistance of sonication, the Pt-Au<sub>0.21</sub>Ag<sub>0.79</sub>-Ag<sub>2</sub>Se in 5.00ml of toluene was mixed with 0.20 ml of oleylamine and 0.10ml of oleic acid to form a homogenous solution before being transferred to a three-neck flask, followed by degassing with N<sub>2</sub> gas flow for 30mins. Then 1.00ml of Cd(NO<sub>3</sub>)<sub>2</sub> solution in methanol (25.00mg/ml) was added at 85°C, followed by injection of 0.018ml of TBP. The reaction lasted for 12hrs before the solution was cooled down to room temperature. The product was obtained by addition of 5 times of methanol and 5 times of ethanol in volume, followed by centrifugation at 4000rpm for 10mins. The precipitate was re-dispersed in toluene.

*Pt-Au<sub>x</sub>Ag<sub>y</sub>-CdSe nanooligomers (0.8 ≥ x ≥ 0.5):* The Pt-Ag-Ag<sub>2</sub>Se nanooligomers (with Ag growth time of 7hrs) in 5.00ml of deionized H<sub>2</sub>O was mixed with 4ml of TTAB aqueous solution (0.200M) and 0.600ml of HAuCl<sub>4</sub> (1.00mg/mL). The reaction was started by addition of 0.10ml of AA solution (0.800M) at the room temperature for 6hrs under mild stirring. The product was obtained by centrifugation at 7000rpm for 15mins. After centrifugation, water in the top needed to be removed as much as possible. 6.00ml of toluene and 2.00ml of acetone were then added into the residue, followed by addition of 0.60ml of decanethiol solution in acetone (10.0%). With the assistance of sonication for 30mins the Pt-Au<sub>x</sub>Ag<sub>y</sub>-Ag<sub>2</sub>Se was dissolved to form a uniform phase. 0.30ml of oleylamine and 0.15ml of oleic acid were added, followed by sonication for another 30mins. After that, two times of ethanol in volume was added, followed by centrifugation at 3000rpm for 20mins. The precipitate was dispersed in toluene.

With the assistance of sonication, the Pt-Au<sub>x</sub>Ag<sub>y</sub>-Ag<sub>2</sub>Se in 5.00ml of toluene was mixed with 0.20 ml of oleylamine and 0.10ml of oleic acid to form a homogenous solution before being transferred to a three-neck flask, followed by degassing with N<sub>2</sub> gas flow for 30mins. Then 1ml of Cd(NO<sub>3</sub>)<sub>2</sub> solution in methanol (25.00mg/mL) was added at 85°C, followed by injection of 0.018ml of TBP. The reaction lasted for 12hrs before the solution was cooled down to room temperature. The product was obtained by addition of 5 times of methanol and 5 times of ethanol in volume, followed by centrifugation at 4000rpm for 10mins. The precipitate was re-dispersed in toluene.

### 3.2.11 Synthesis of Pt-CdSe-CdS and Pt-HgSe-CdS nanooligomers

*Pt-CdSe-CdS nanooligomers:* The Pt-Ag-Ag<sub>2</sub>Se nanooligomers (with Ag growth time of 7hrs) in 5.00ml of deionized H<sub>2</sub>O was mixed with 0.20ml of TTAB aqueous solution (0.200M), followed by injection of 0.40ml of Na<sub>2</sub>S solution (0.100M) at 50°C. The reaction was stopped after 30mins. The product was obtained by centrifugation at 7000rpm for 15mins. The precipitate was dispersed in 5.00ml of deionized H<sub>2</sub>O with addition of 0.20 ml of TTAB aqueous solution (0.200M) and was degassed by N<sub>2</sub> gas flow in a three-neck flask for 30mins. Then 1.00ml of Cd(NO<sub>3</sub>)<sub>2</sub> solution in methanol (25.00mg/mL) was added at 60°C, followed by injection of 0.018ml of TBP. The reaction lasted for 12hrs before the solution was cooled down to room temperature. The product was obtained by addition of 10.00ml of deionized H<sub>2</sub>O, followed by centrifugation at 4000rpm for 10mins. The precipitate could be re-dispersed in 5ml of deionized H<sub>2</sub>O.

*Pt-HgSe-CdS nanooligomers:* With the assistance of sonication, the Pt-Ag-Ag<sub>2</sub>Se in 5ml of toluene solution was mixed with 0.20ml of oleylamine and 0.10ml of oleic acid to

form a homogenous solution before being transferred to a three-neck flask, followed by degassing with N<sub>2</sub> gas flow for 30mins. Then 1.00ml of Hg(NO<sub>3</sub>)<sub>2</sub> solution in methanol (3.00mg/mL) was added at 50°C, followed by injection of 0.012ml of TBP. The reaction lasted for 12hrs before the solution was cooled down to room temperature. The product was obtained by addition of 5 times of methanol and 5 times of ethanol in volume, followed by centrifugation at 4000rpm for 10mins. The precipitate could be dispersed in toluene.

With the assistance of sonication, the Pt-HgSe-Ag in 5.00ml of toluene solution was mixed with 0.20 ml of oleylamine and 0.10ml of oleic acid to form a homogenous solution before being transferred to a three-neck flask, followed by degassing with N<sub>2</sub> gas flow for 30mins. The S-precursor was then added to the solution to convert the Pt-HgSe-Ag to the Pt-HgSe-Ag<sub>2</sub>S. Then 1ml of Cd(NO<sub>3</sub>)<sub>2</sub> solution in methanol (25.00mg/ml) was added at 50°C, followed by injection of 0.018ml of TBP. The reaction lasted for 1hr before the solution was cooled down to room temperature. The product was obtained by addition of 5 times of methanol and 5 times of ethanol in volume, followed by centrifugation at 4000rpm for 10mins. The precipitate was dispersed in toluene.

### 3.2.12 Synthesis of Pt-Ag<sub>2</sub>Se-CdSe-AuAg nanooligomers

A typical synthesis started with the Pt-Ag<sub>2</sub>Se heterodimers in the *Section 3.2.9*. The Pt-Ag<sub>2</sub>Se heterodimers was diluted by 5.00ml of deionized H<sub>2</sub>O and 4ml of TTAB aqueous solution (0.200M). 0.15ml of HAuCl<sub>4</sub> aqueous solution (1.00mg/mL) was added sequentially every half an hour under stirring for twice. The product of Pt-AuSe was



obtained by centrifugation at 7000rpm for 15mins. The precipitate was dissolved in 5.00ml of deionized H<sub>2</sub>O, and was mixed with 0.20ml of TTAB solution (0.200M) and 0.30ml of AgNO<sub>3</sub> aqueous solution (0.010M). The reaction was started by addition of 0.20ml of AA (0.800M) at 70°C (oil bath) and lasted for 2hrs under mild stirring. The reaction was stopped when the solution color changed from light brown to dark yellow. The product (Pt-Ag<sub>2</sub>Se-AuAg) was obtained by centrifugation at 7000rpm for 15mins. The precipitate was dissolved in 5.00ml of deionized H<sub>2</sub>O and was mixed with 0.20ml of TTAB aqueous solution (0.200M). 0.20ml of Se-precursor was added into the solution at 70°C under N<sub>2</sub> gas protection. The reaction lasted for 15mins. The product of Pt-Ag<sub>2</sub>Se-AuAgSe was obtained by centrifugation at 7000rpm for 15mins. The precipitate was diluted by 10.0ml of deionized H<sub>2</sub>O and 0.50ml of 0.200M TTAB aqueous solution. 0.040ml of 0.05M KCN aqueous solution was added under stirring and the etching lasted for 16hrs. The etched product was obtained by centrifugation at 7000rpm for 15mins. The precipitate was dissolved in 5.00ml of deionized H<sub>2</sub>O, and was mixed with 0.20ml of 0.200M TTAB aqueous solution and 0.15ml of 0.010M AgNO<sub>3</sub> aqueous solution. The reaction was started by addition of another 0.20ml of AA solution (0.800M) at 70°C (oil bath), and lasted for 150mins under mild stirring. The product of Pt-Ag<sub>2</sub>Se-Ag<sub>2</sub>Se-AuAg was obtained by centrifugation at 7000rpm for 15mins. The precipitate was mixed with 6.00ml of toluene, 2.00ml of acetone and 0.60ml of decanethiol solution in acetone (10%). With the assistance of sonication for 30mins, the Pt-Ag<sub>2</sub>Se-Ag<sub>2</sub>Se-AuAg could be dissolved to form a uniform phase. 0.30ml of oleylamine and 0.15ml of oleic acid were added, followed by sonication for another 30mins. After that, two times of ethanol in volume was added, followed by centrifugation

at 3000rpm for 20mins. The precipitate could be dispersed in toluene. With the assistance of sonication, the Pt-Ag<sub>2</sub>Se-Ag<sub>2</sub>Se-AuAg was dissolved in 5.00ml of toluene solution, mixed with 0.20 ml of oleylamine and 0.10ml of oleic acid to form a homogenous solution before being transferred into a three-neck flask, followed by degassing with gas N<sub>2</sub> flow for 30mins. Then 1.00ml of Cd(NO<sub>3</sub>)<sub>2</sub> solution in methanol (25.00mg/mL) was added at 50°C, followed by injection of 0.018ml of TBP. The reaction lasted for 1hr before the solution was cooled down to room temperature. The final product of Pt-Ag<sub>2</sub>Se-CdSe-AuAg was obtained by addition of 5 times of methanol and 5times of ethanol in volume, followed by centrifugation at 4000rpm for 10mins. The final product could be dispersed in toluene.

## *4. Result*

### 4.1 Hybrid Dimer

The simplest nanooligomers, heterodimers, have emerged as a new type of colloid structure and have been the subject of extensive studies in recent years[175]. They provide a perfect platform for the study of quasiparticle interactions, such as the interaction between two plasmons[176], or between plasmons and spin[177].

#### 4.1.1 Au-CdSe Nanodimer

We prepared Au seed NPs dispersed in toluene solution by the published method and adjusted the sizes to 6.5nm and 10nm, respectively [172]. In a typical experiment, we found that the Ag coating occurred when seed NPs mixed with the AgNO<sub>3</sub>/methanol solution. Oleylamine served as both the capping ligand and a weaker reducing reagent as

compared to other inorganic reagents[178]. The nitrogen atom in the oleylamine shared the electron pair with the dangling d-orbit of Ag or Cd to solidify the capping[179]. Slow reduction allowed for fine control over Ag shell thickness[180]. By adjusting the reaction time and temperature, we achieved control over the size of Ag<sub>2</sub>Se, and then accomplished CdSe. In the following step, the Ag shell reacted with the Se-oleylamine-OA precursor to reshape into a bulky Ag<sub>2</sub>Se at 100C~130C and speed up phase separation. In the final stage, Cd<sup>2+</sup> replaced Ag<sup>+</sup> in the crystal lattice by cation exchange in the presence of TBP under ambient conditions.

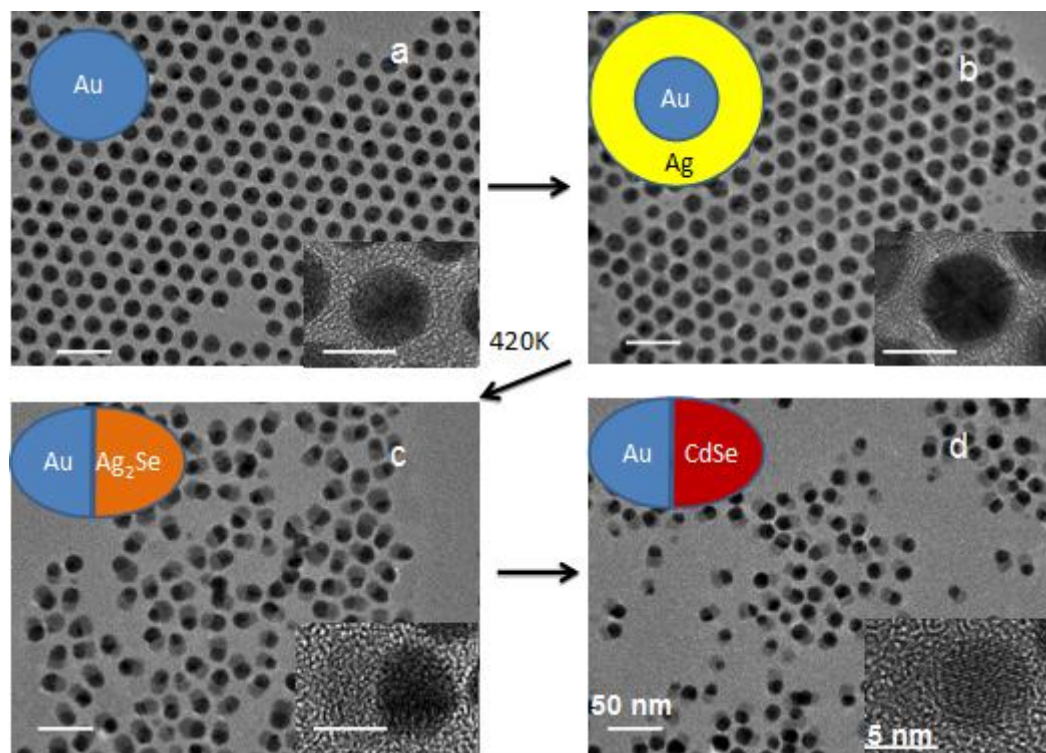


Fig 3.7. Series of high and low-resolution TEM images highlighting different synthetic stages of Au-CdSe growth. All scale bars have been normalized to the same scale as Figure 3.7d. (a) Ag NPs. (b) Au@Ag core-shell structure NPs. (c) Au-Ag<sub>2</sub>Se nanodimers. (d) Au-CdSe nanodimers.

In order to characterize NPs as synthesized and to gain insights on their structural properties, we employed transmission electron microscopy (TEM) in the bright field mode.

Figure 3.7 demonstrates our sequential controls over Au, Au@Ag, Au-Ag<sub>2</sub>Se and Au-CdSe. Figure 3.7a and Figure 3.7b exhibit low-resolution and high-resolution TEM images of Au and Au@Ag NPs with average diameters of 6.5±0.3nm and 7.3±0.4nm, respectively. Au-Ag<sub>2</sub>Se in Figure 3.7c maintained a good size distribution even after the vigorous exothermic reaction between Ag and Se. Phase separation played a key role in shaping the nanodimer, which became more sensitive to the temperature due to its reduced scale. Figure 3.7d shows that CdSe inherited its size and shape from Ag<sub>2</sub>Se. The similarity between the molar volume of Ag<sub>2</sub>Se and CdSe makes it easy to predict the final size of CdSe, and the immobility of Se<sup>2-</sup> framework during cation exchange led to a negligible change in the morphology of CdSe[168].

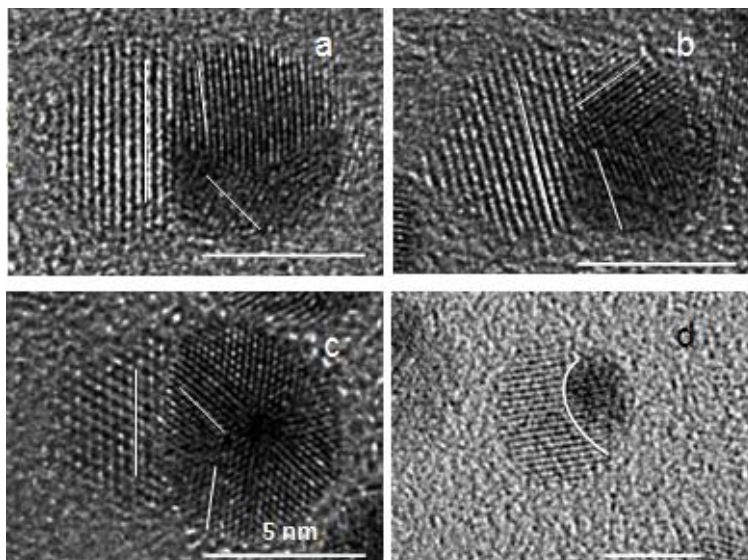


Fig 3.8. Orientations of different crystalline domains at the boundary of individual Au-CdSe NPs. Scale bar, 5nm.

We observed the non-epitaxial growth process of CdSe on Au. In Figure 3.8, we highlight the orientations of crystalline domains in both CdSe and Au. CdSe possesses an evident monocrystalline feature but the adjacent Au displayed twinning defects (Fig 3.8b and Fig 3.8c), multiple twinning defects (Fig 3.8a) or even a curved surface on the interface (Fig 3.8d). One CdSe facet faces multiple Au facets and we could not assume safely that a preferential orientation between CdSe and Au exists. Thus the growth should follow a non-epitaxial growth mechanism.

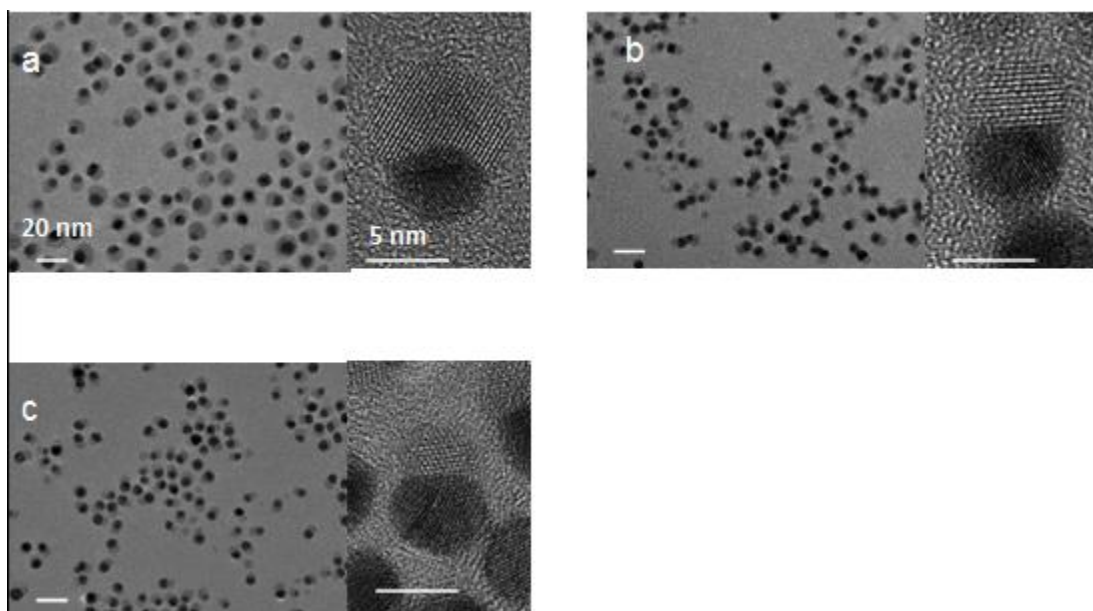


Fig 3.9. Tuning the size of CdSe part in Au-CdSe NPs. All scale bars have been normalized to the same scale as Figure 3.9a. (a) Au(5nm)-CdSe(7nm) nanodimers. (b) Au(5nm)-CdSe(5nm) nanodimers. (c) Au(5nm)-CdSe(4nm) nanodimers.

By varying the amount of Ag on Au, we also tuned the final size of CdSe. Three examples are shown in Figure 3.9 with CdSe sizes adjusted to 9nm, 7nm, and 5nm, respectively (Fig 3.9). It is necessary to point out that a long reaction time can cause Au to react with Se, which is not as stable at nanoscale as the bulk[181][182]. We carefully

chose the temperature and reaction time to assure that Au did not overreact with Se while during the complete reaction with Ag.

#### 4.1.2 Pt-CdS Nanodimer

Pt plays an important role in a wide variety of applications, mainly as the catalyst for CO/NO<sub>x</sub> oxidation in catalytic converters, refining of petroleum, and many other organic reactions such as hydrogenations[183]. Several reports have proposed a combination of semiconductors and Pt to apply the electron flowing from semiconductors to enhance Pt catalysis efficiency because Fermi levels of Pt lie below the conduction band of semiconductors[184]–[186]. Motivated by this recommendation, we grew and characterized Pt-CdS nanodimers. The synthesis of Pt-CdS followed a similar path to Au-CdSe. First, we acquired Pt nanocubes by following Yang's method with slight modifications[174]. We then dispersed the nanocubes in the aqueous phase and capped by TTAB, which has been used widely in controlling the shape of Ag and Au NPs[187]. We deposited Ag on Pt with the aid of AA at 70°C. There are many ways to vulcanize Ag, either by phase transferring Pt-Ag NPs into an organic solvent to react with a S-oleylamine-oleic acid molecular precursor or by directly applying alkaline sulfide into the water solution. We used the first method to be consistent with our previous Au-CdSe cases, although the other method reduces reaction time while keeping similar quality.

Once Pt-Ag<sub>2</sub>S was formed, we could obtain Pd-CdS by a single cation exchange step. Typically this reaction in the aqueous phase requires extended time, higher temperature and O<sub>2</sub>-free condition because the Ag<sup>+</sup> to Cd<sup>2+</sup> equilibrium is not favored in the aqueous phase, in which TBP has low solubility[188].

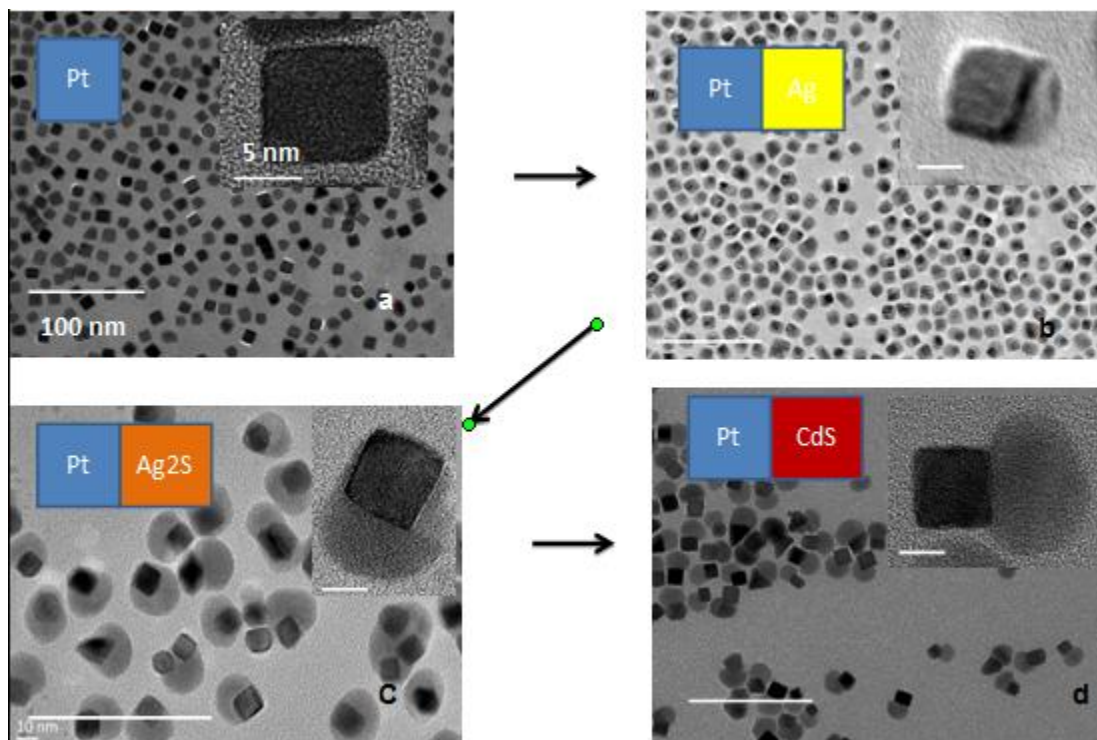


Fig 3.10. Sets of high and low-resolution TEM images demonstrating different synthetic stages of Pt-CdS growth: (a) Pt. (b) Pt-Ag. (c) Pt-Ag<sub>2</sub>S. (d) Pt-CdS. All the scale bars have been normalized to the same scale as Fig 3.10a.

Figure 3.10 shows our sequential controls over Pt, Pt-Ag, Pt-Ag<sub>2</sub>S, and Pt-CdS. It wasn't fully unexpected that the deposited Ag, when it was big enough, acquired a quasi-cubic feature (Fig 3.10b). The TTAB prohibited the growth of noble metals in any other direction except for the {100} facet[189]. Surprisingly, we found an inhomogeneous growth of Ag that saved our effort in the phase separation. A possible explanation for this is the low nucleation rate of Ag on the surface of noble metals, which Xia proposed when addressing a similar case in a Pd-Ag system[157]. The self-catalytic behavior of Ag with limited growth sites drives incoming Ag to grow preferentially on the previous Ag instead of on other sites on the Pt surface. Meanwhile, the equivalence among six {100}

facets of Pt nanocubes allowed us to perform another meaningful control over the number of facets occupied by CdS. This control can be used to adjust the interface area of semiconductor-metal interface to affect the total influx of the charge transfer at the interface[190], to modulate total active area for catalysis, or to determine the position for further Ag deposits. When we varied the quantity of Ag coated on Pt, the dewetting of  $\text{Ag}_2\text{S}$  during phase separation determined how many facets would be exposed. Judging from the TEM images (Fig 3.11), we achieved up to three-side occupied control. Unlike Au-CdSe, Pt-CdS only has two distinct monocrystalline domains. The mismatch of lattice constants on the interface between the Pt core and the monocrystalline CdS (Pt,  $a=3.920\text{\AA}$ ; zinc-blende CdS,  $a=6.050\text{\AA}$ ) led to specific non-parallel orientation as the CSL theory predicts, and we verified this by TEM (Fig 3.10).

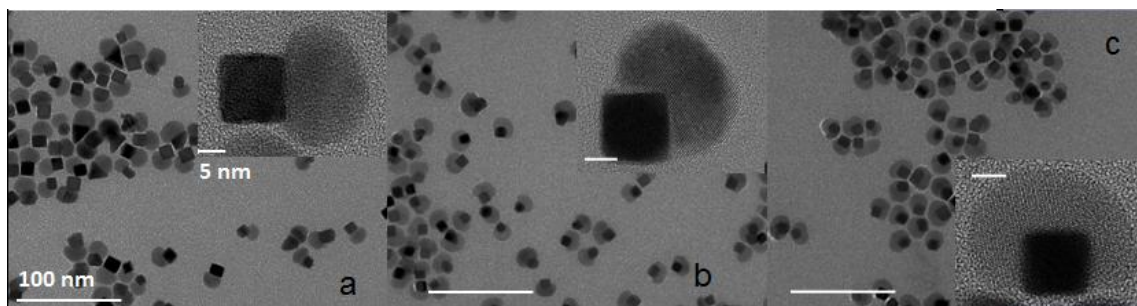


Fig 3.11. Control over the number of Pt facets occupied by CdS. (a) One-side control. (b) Two-side control (c) Three-side control. All the scale bars have been normalized to the same scale as Figure 3.11a.

#### 4.2 Hybrid Trimer and More Modules Incorporated in a Single NP

Thanks to this new scheme, we can explore more complicated nanooligomeric structure than dimers. Addition of one more modules allows for the association of new functionalities with this NP, but the synthesis becomes more challenging. We started the



synthesis from the Pt-Ag<sub>2</sub>Se. The high resolution TEM image of Pt-Ag<sub>2</sub>Se reveals that even with a dimer feature, the ‘clean’ surface of Pt was actually covered in thin layers of Ag<sub>2</sub>Se, which prevents further Ag coating. We introduced potassium cyanide (KCN) to remove the unwanted Ag<sub>2</sub>Se because it had previously proved to be a successful etching reagent for Au and Ag in nanotechnology[191].

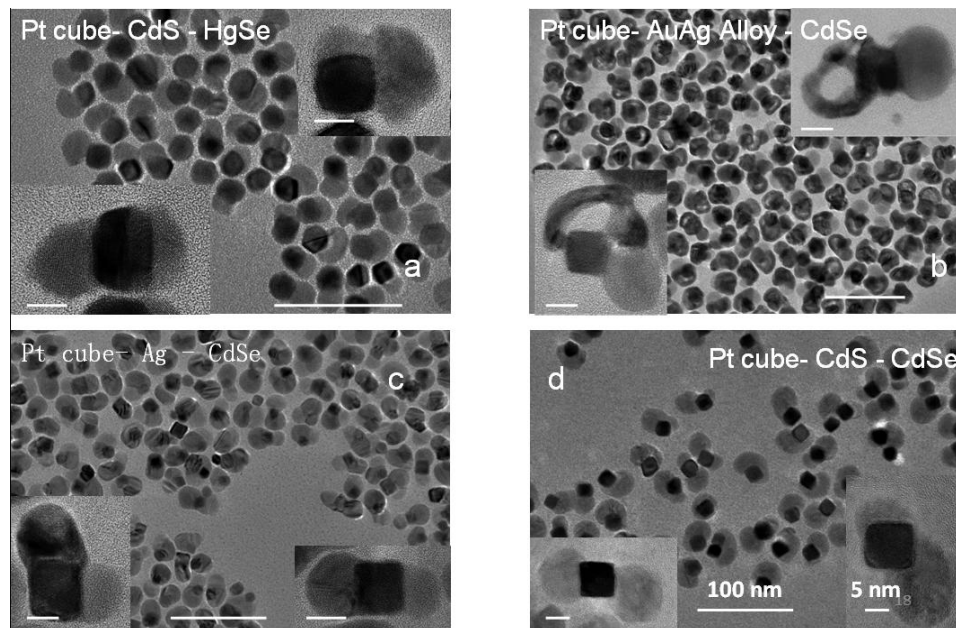


Fig 3.12. Different combinations of nanotrimers. Two high resolution images show the diagonal feature and the side-by-side feature, respectively. All the scale bars have been normalized to the same scale as Fig 3.12d. (a) Pt-CdS-HgSe. (b) Pt-Au/Ag-CdSe. (c) Pt-Ag-CdSe. (d) Pt-CdS-CdSe.

Assuming the etching speed of KCN was independent of the different facets of Ag<sub>2</sub>Se, the thinner layer cleared fast and followed by the shrinkage of Ag<sub>2</sub>Se. To get a suitable size of CdSe, we prepared larger Ag<sub>2</sub>Se. Meanwhile, adjusting the etching time proved to be a powerful tool in determining the final size of the semiconductor part of the NP.

The etching process as described above allowed for further Ag deposition and the use of a different anion, usually  $S^{2-}$ , to react with new Ag. There are a few reports that  $S^{2-}$  coexists with  $Se^{2-}$  in the lattice of  $Ag_2Se$  due to their similar chemical reactivity[192]. Thus, we detected trace amounts of  $S^{2-}$  in the  $Ag_2Se$  part by EDS since it had been surrounded by  $S^{2-}$  in the reaction while the  $Ag_2S$  part remained  $Se^{2-}$  free.

When  $Ag_2Se$  occupied any facet of Pt, we had two choices left for further coating, one being the four neighboring positions and the other was the diagonal position. If the initial  $Ag_2Se$  had no effect on determining the position of the following modules, we could conclude that the number of nanotrimers with CdSe and CdS side by side should be four times more likely than the number with the diagonal configuration, and low resolution TEM images (Fig 3.12d) partially confirms that indeed, the NPs with Pt-CdSe-CdS side by side NPs were more frequent than those with the diagonal configuration.

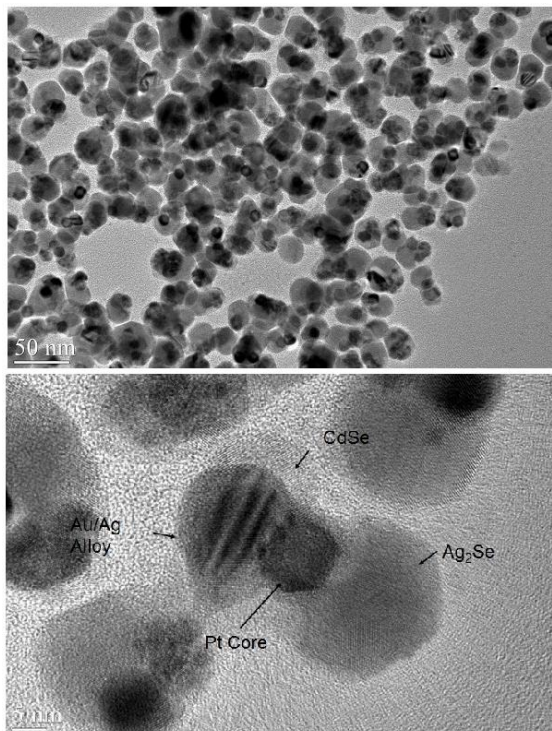
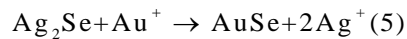


Fig 3.13. A nanooligomer consisting of four components: Pt core,  $Ag_2Se$ , CdSe, and Au/Ag alloy. Top: the low resolution TEM image. Bottom: the high resolution TEM image of a typical nanooligomer NP with every component labeled out.

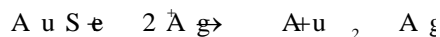
Further addition of three modules onto one Pt cube is shown in the case of Pt-Ag/Au-Ag<sub>2</sub>Se-CdSe (Fig 3.13), which contains an adjustable SPR module, two semiconductors with no overlapped absorption bands, and one catalyst core. There has been only one report on nanooligomers with more than four materials[161], but its author did not study the potential applications or perform property measurements.

We found an interesting phenomenon in Pt-Ag/Au-Ag<sub>2</sub>Se-CdSe. According to the theory of hard-soft acids and bases, Au<sup>+</sup> (though we used HAuCl<sub>4</sub>, Au<sup>3+</sup> was unstable in the presence of a reducing reagent and could be reduced to Au<sup>+</sup> easily) behaves as a stronger acid than Ag<sup>+</sup>. Consequently, Au<sup>+</sup> shares its d-orbitals and coordinates with soft bases, like the Se<sup>2-</sup> in our synthesis. The free energy of reaction ( $\Delta G$ ) is qualitatively determined by the coordination stability of these complexes and can further govern the equilibrium of reaction[193]. The large  $\Delta G$  in eq. (4) prohibits the reverse reaction from occurring without the aid of a catalyst. However, in our experiment, Ag<sup>+</sup> replaced Au<sup>+</sup> in the AuSe bulk readily in the presence of AA. We propose the above mechanism as follows:

The original balance between Au<sup>+</sup> and Ag<sup>+</sup> went towards the formation of AuSe,



After the introduction of AA, the Au<sup>+</sup>/Au pair has more positive potential (0.88V higher[194]) than Ag<sup>+</sup>/Ag, therefore Au<sup>+</sup> was more readily reduced by AA and was consumed in the process. The forward equilibrium in eq. (5) started to reverse as:



At the same time we found that though two modules started as Ag<sub>2</sub>Se, only the newly-made one could be converted into CdSe during the cation exchange while the

other remained answer.  $\text{Ag}_2\text{Se}$  has two phases and at  $130^\circ\text{C}$  the bulk  $\beta$ -phase  $\text{Ag}_2\text{Se}$  will turn into the  $\alpha$ -phase. The  $\text{Ag}_2\text{Se}$  formed from  $\text{AuSe}$  had gone through a long annealing process (Fig 3.14) at  $70^\circ\text{C}$ . It is possible that before cation exchange it had been converted into the  $\alpha$ -phase since the temperature for the phase transition at the nanoscale is greatly lowered[195], while the other  $\text{Ag}_2\text{Se}$  remained in the  $\beta$ -phase. The energy difference between two phases is as large as  $2.2\text{kcal/mol}$ , enough to cause the difference in the cation exchange[196].

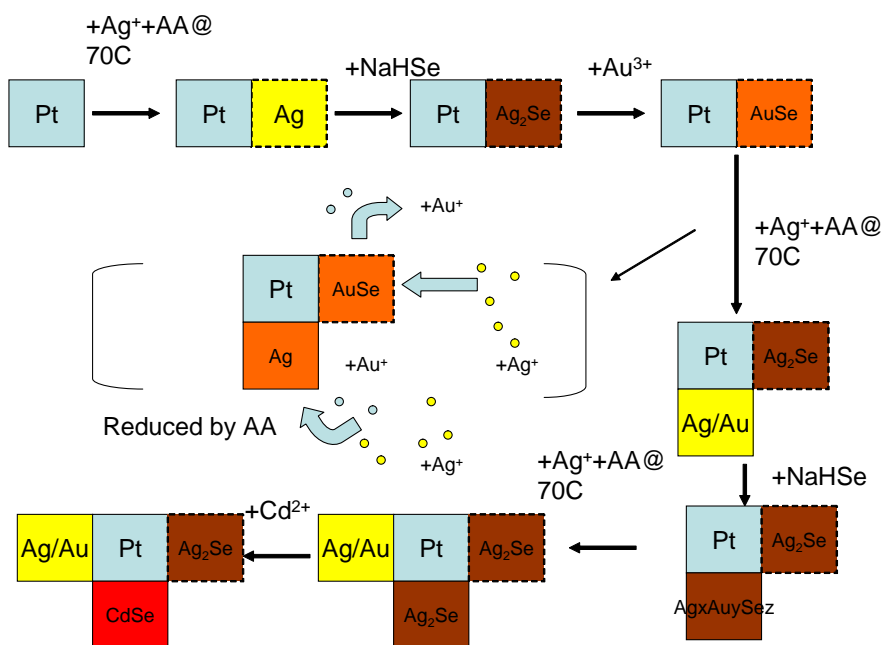


Fig 3.14. Schematic of the growing process for Pt-Ag/Au-Ag<sub>2</sub>Se-CdSe NP and a possible mechanism for Au<sup>+</sup>/Ag<sup>+</sup> substitution. During two reductions of Ag<sup>+</sup> by AA, the Ag<sub>2</sub>Se in dashed lines was annealed twice at 70°C, while the other Ag<sub>2</sub>Se in solid lines had only one annealing.

## 5. Properties and Measurements

To explore the interaction between plasmonic materials and semiconductors, we changed the sizes of Au and CdSe in Au-CdSe and acquired corresponding absorption spectra. Both Au and CdSe are materials that have been widely studied and reported on. With absorption in visible range, their major applications are in the optical and optoelectronic fields[197] as well as in biochemical and biomedical application[198]. Au's strong optical absorption is a result of the oscillation of conduction electrons under an external electromagnetic field[199]. In contrast, the optical absorption of CdSe, a II-VI semiconductor, relies on electrons to be excited from the valence to the conduction band.

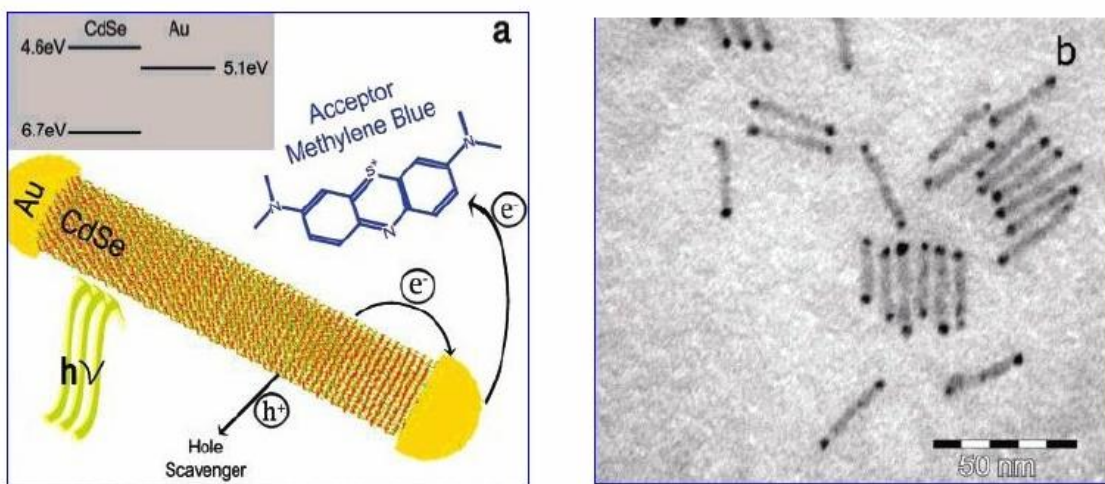


Fig 3.15. The nanodumbbells system of CdSe rods with Au tips on the both sides. (a) Scheme of a light-induced charge separation mechanism in a CdSe-Au nanodumbbell. (b) TEM image of CdSe-Au hybrid nanodumbbells. Reprinted from Ref. [200].

Banin's group has thoroughly investigated an Au-CdSe dumbbell system (Fig 3.15) [200]–[202]. They developed a systematic method for growing Au dots onto the tips of CdSe rods and examined Au-CdSe absorption spectra with an emphasis on its charge

separation. They claimed that the band offsets between Au and CdSe were caused by rapid electron transfer from the conduction band of CdSe to the Au tips, leading to charge separation.

Our work focused on Au-CdSe nanodimers. Compared to the rod, the CdSe dot had extra absorption energy sensitivity for its size. Routinely synthesized CdSe can be tuned to have an absorption peak around 450nm-600nm by varying its size to cover the usual SPR peak of Au NPs at 520nm[203].

The absorption strength of CdSe cannot match the SPR peak from Au at the same concentration (Fig 3.16). Even when it outnumbered Au by a 2:1 ratio, the CdSe exciton peak in the simple mixture of CdSe NPs and Au NPs is barely visible in the tail of the SPR peak. When we reduced the distance between Au and CdSe to zero in the nanodimer, the overall absorption feature was changed dramatically. If the SPR contributed to the major absorption, there was a 20nm~30nm redshift.

Others have observed this phenomenon in different combinations of noble metals and semiconductors and two dominant theories to explain the redshift have emerged. The first theory treats CdSe as a dielectric medium that forms an inner electric field when the external light field is applied[59]. It modulates the incoming light field and affects the charge distribution on the surface of Au. Because of its refractive index (~8.0) [204], the effect of CdSe on the SPR cannot be ignored. For a given geometry, it is possible to calculate the extinction coefficient quantitatively by following the Mie theory[205]. The second theory, however, is more complicated. When metal and semiconductor components interact, the energy barrier for electrons to transfer from semiconductor to metal becomes small enough to be susceptible to penetration by interdomain charge

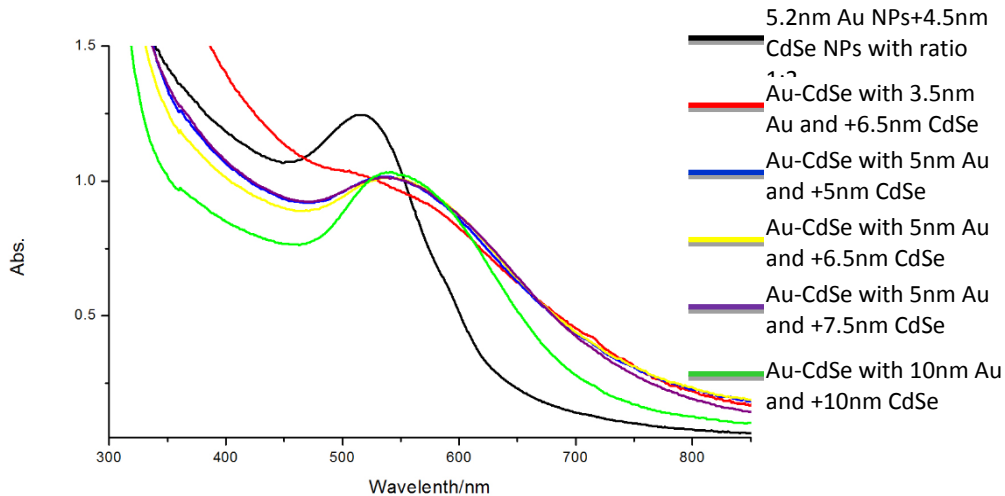


Fig 3.16. Comparison of normalized absorption spectra for different module sizes. The shoulder peak around 580nm for the black line is the absorption for 4.5nm CdSe NPs, if we assume that interactions do not happen between CdSe and Au NPs when the mixture concentration is low.

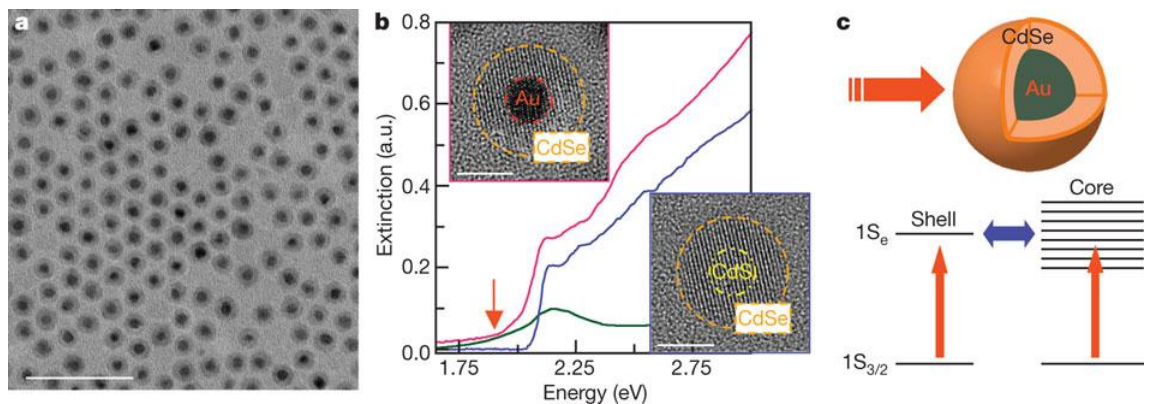


Fig 3.17. The optical property for Au@CdSe system. (a) Typical large scale TEM image for Au@CdSe. Scale bar, 50nm. (b) Typical linear optical absorption spectra of Au–CdSe (pink), CdS–CdSe (blue) and CdSe (Black) at 2K. (c) A schematic model showing transitions and resonant coupling (blue arrow) between core (continuum spectrum of plasmon) and shell (discrete interband exciton) in a hetero-core–shell configuration under laser excitation. Reprinted from Ref. [206].

transfer from adjacent domains[207]. The mixing of electronic states at the metal-semiconductor boundary is unavoidable. To better illustrate this idea, we cite Ouyang's work on the Au core and CdSe shell structure (Au@CdSe)[206]. Figure 3.16 clearly reveals a substantially red-shifted and broadened peak with a long absorption tail in Au-CdSe. Ouyang's group indentified the existence of hybrid excitons from the distinct optical features in Figure 3.17 and attributed hybrid excitons to the resonant coupling between discrete interband excitons in the semiconductor shell and surface plasmons having a continuous spectrum in the metal core, when the exciton energy is in the vicinity of plasmon peak. Restricting ourselves to the qualitative analysis, we reviewed Figure 3.16 to determine which explanation was more reasonable. When the size of the CdSe part increased while keeping the Au part constant (the blue, yellow and purple line), the peak remained at 530nm. This phenomenon contradicts the dielectric medium theory, which suggests an extreme sensitivity of the affected SPR peak to the size of dielectric medium. Therefore, we conclude that it should be the resonance between plasmon and exciton.

## 6. *Nanoscale Photocatalysis*<sup>1</sup>

### 6.1 Introduction

Nanoscale photocatalysis represents a promising route towards a harnessing electromagnetic process to convert solar power to chemical energies. A typical nanoscale system exclusively involves semiconductor nanostructures, in which photo-generated

---

1. This part was adapted from: Lin Weng, Hui Zhang, Alexander O. Govorov, and Min Ouyang, Hierarchical Synthesis of Hybrid Nanooligomers and Enabled Hot-Plasmon Driven Photocatalysis, *Science*, 2012, submitted.



electron-hole pairs in semiconductors can be rapidly separated at the semiconductor-catalyst interface to perform redox chemistry at the catalytically active sites [186][200][208]–[210]. One current major challenge of semiconductor-based photocatalysis is the low energy conversion efficiency due to a number of issues including fast carrier recombination and short carrier diffusion length because of the existence of defects, a low absorption coefficient, or reflection loss by high refractive index, among others. While some of these issues can be remedied by improving the sample quality (such as monocrystallinity of semiconductors), there are alternative methods. For example, there is significant evidence supporting a concept that involves integrating plasmonic effects to enhance photocatalytic efficiency[211].

Nevertheless, the real mechanism and reaction pathway following the optical excitation of plasmons remains ambiguous. A predictive model combined with elaborative material control is necessary in order to gain understanding of the upper limit of a plasmon-mediated enhancement to the design of highly efficient materials[209]. In order to evaluate the performance of Pt-Au<sub>x</sub>Ag<sub>y</sub>-CdSe nanooligomers, we applied a model system of methylene blue (MB) dye molecules, in which the MB molecules could be reduced to form colorless leucomethylene molecules upon addition of two electrons[186][200]. Under visible light illumination, in a regular photocatalytic system, such as Pt-CdSe heterodimers, a photo-induced electron-hole pair within CdSe nanoparticles can rapidly dissociate at the catalyst-semiconductor interface and the separated electrons thus migrate through the catalytic active site of Pt towards the MB molecules for photo-induced reduction (correspondingly, solvent molecules such as ethanol act as a hole scavenger for the CdSe subunits to complete a reaction) (Fig 3.23A).

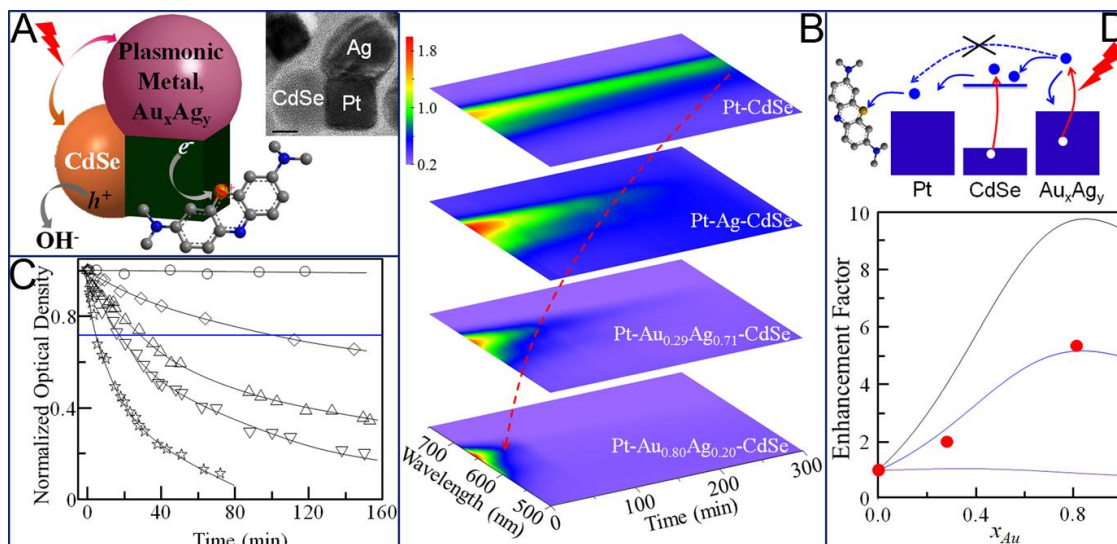


Fig 3.18. Hot-plasmon driven photocatalysis of the Pt-Au<sub>x</sub>Ag<sub>y</sub>-CdSe nanooligomers. (A) Schematics of photocatalytic reduction of the MB molecules by the Pt-Au<sub>x</sub>Ag<sub>y</sub>-CdSe nanooligomers under visible light illumination. (Inset) Typical HR-TEM image of a Pt-Ag-CdSe nanooligomer. Scale bar, 5nm; (B) Two-dimensional time evolution of optical absorption profile of the MB molecule enabled by the Pt-Au<sub>x</sub>Ag<sub>y</sub>-CdSe nanooligomers with various ratio of  $x/y$ . An arrowed red dashed curve highlights the tendency of photocatalytic reaction rate with the increase of  $x/y$  by comparing peak evolution at 677nm. (C) Time-dependent optical density of the MB molecules at 677nm with different photocatalysts. The optical density at different reaction time is normalized to the initial value before photocatalytic reaction starts. (O): physical mixture (1:1:1 molar ratio) of Pt, CdSe, Au nanoparticles; ( $\diamond$ ): Pt-CdSe; ( $\Delta$ ): Pt-Ag-CdSe; ( $\nabla$ ):Pt-Au<sub>0.21</sub>Ag<sub>0.79</sub>-CdSe; ( $\star$ ):Pt-Au<sub>0.80</sub>Ag<sub>0.20</sub>-CdSe. A blue line is drawn to highlight different time scale for reaching the same optical density of the MB molecules enabled by various photocatalysts. (D) (Top) Schematics of different transfer pathways of optically excited hot plasmonic electrons; (Bottom) Comparison of theoretical and experimental dependence of enhancement factor of photocatalytic reaction rate on the  $x_{Au}$  of a nanooligomer (17). (Black and blue curves): Hot plasmonic electron transfer mechanism following the route of Au<sub>x</sub>Ag<sub>y</sub>-to-Pt-to-MB and Au<sub>x</sub>Ag<sub>y</sub>-to-CdSe-to-Pt-to-MB, respectively. (Purple curve): Near-field enhancement mechanism; ( $\bullet$ ): Experimental values.

As a result, intensity of two characteristic absorption peaks of the MB molecules at 667nm and 609nm, respectively, decrease with time, and the decay constant represents the redox reaction rate (Fig 3.23B, C). It is important to note that when a plasmonic metal alloy subunit,  $Au_xAg_y$ , is coupled into the Pt-CdSe heterodimers, the redox reaction rate increases significantly under same light irradiation condition.

## 6.2 Photocatalysis Measurements

We carried out all photocatalysis experiments in a home-made apparatus, equipped with a Nikon super high pressure Mercury lamp (150W) and external lens pairs for the collimation and adjustment of beam size. We purchased a set of interference filters (FWHM~10nm) from the Newport Corp and the Thorlabs Inc and applied them to select illumination wavelengths. We used a variable metallic neutral density filter wheel to allow for the accurate adjustment of illumination intensity.

We adapted the experimental procedure from the published methods[186][200]. Then, we prepared the MB solution by dissolving MB powder in deionized  $H_2O$  with the optical density adjusted to be 1.5 at 667nm. Typically, we used 1.5ml of nanooligomers with the concentration adjusted to possess optical density of 0.5 at the illumination wavelength. We added 0.4ml of ethanol into the solution and set the solution's pH value to 7. Then, we transferred the mixture solution to a three-neck flask under vigorous stirring and  $N_2$  gas protection. We covered the whole flask with thick alumina foils to carry out our experiments under a dark condition, with only a small aperture open to allow for light illumination at a selective wavelength. We recorded the absorption spectra of the mixture solution with time, using a commercial spectrophotometer (UV-2501PC, Shimadzu).

We were able to evaluate the reaction rate,  $\gamma_{exp}$ , in a photocatalytic process by fitting the time trace of the absorption profile with a single exponential function. To normalize the reaction rate among different samples in order to determine the enhancement factor, we determined the molar concentration of nanooligomers based on an extinction coefficient of the Pt atom at 380nm[212]. For example, the reaction rate we extracted from the Figure 3.18C is summarized in Table 3.1.

Samples	Pt-CdSe	Pt-Ag-CdSe	Pt-Au <sub>0.29</sub> Ag <sub>0.71</sub> -CdSe	Pt-Au <sub>0.80</sub> Ag <sub>0.20</sub> -CdSe
$\gamma_{exp}(\text{min}^{-1})$	0.00366	0.0101	0.019	0.0542

Table 3.1. Reaction rate by fitting to data presented in the Figure 3.18C.

### 6.3 Theoretical Modeling of Energetic Hot Plasmonic Electrons Driven Photocatalysis by the Pt-Au<sub>x</sub>Ag<sub>y</sub>-CdSe Nanooligomers<sup>1</sup>

Figure 3.18D shows the model of electron transfer in the system. We derived this model from the following observations and reasoning (Fig 3.19). Both the Pt and Au-Pt systems did not show significant catalytic activity; in Figure 3.18C, the straight line in the normalized optical density shows that Pt alone does not create noticeable catalysis and we observed the same thing for Au-Pt (Fig 3.20). Therefore, the Au to Pt path for the transfer of optically generated carriers is not active and we did not include it in the picture. Then, the photo-generated carriers could only be transferred to Pt via CdSe. Therefore, we wrote down the following balance equations:

---

1. This part is the work of Hui Zhang and Alexander O. Govorov at Ohio University.

$$\begin{aligned}
\frac{dN_{Pt}}{dt} &= \gamma_{QD \rightarrow Pt} N_{QD} - \gamma_{Pt \rightarrow molecules} N_{Pt} \\
\frac{dN_{QD}}{dt} &= -(\gamma_{QD \rightarrow Pt} + \gamma_{QD \rightarrow MNP}) N_{QD} + \gamma_{MNP \rightarrow QD} N_{MNP} + \frac{\alpha_{QD} \cdot I_0}{h\omega_0} - \gamma_{rec,QD} N_{QD} \\
\frac{dN_{MNP}}{dt} &= -(\gamma_{relax,MNP} + \gamma_{MNP \rightarrow QD}) N_{MNP} + \gamma_{QD \rightarrow MNP} N_{QD} + \frac{\alpha_{MNP} \cdot I_0}{h\omega_0}
\end{aligned} \quad (7)$$

where we include the most relevant terms. The involved functions and parameters here are defined as follows:

$N_{MNP}$  - the number of hot plasmonic electrons in the metal nanoparticle (MNP);

$N_{QD}$  and  $N_{Pt}$  - the numbers of photo-generated electrons in the semiconducting quantum dot (QD) and the Pt nanoparticle, respectively;

$\gamma_{Pt \rightarrow molecules}$ ,  $\gamma_{QD \rightarrow Pt}$ ,  $\gamma_{QD \rightarrow MNP}$ ,  $\gamma_{MNP \rightarrow QD}$  - the electron transfer rates between the components;

$\gamma_{relax,MNP}$  - the relaxation rate of hot plasmonic electrons in the MNP;

$\gamma_{rec,QD}$  - the recombination rate in the QD;

$\alpha_{QD}$ ,  $\alpha_{MNP}$ ,  $I_0$  are the absorption cross sections of the QD and the MNP subunits and the incident intensity, respectively.

The above equations assume that the energy relaxation in Pt is fast and the electrons transferred to Pt from CdSe are trapped and do not move back. Simultaneously, we assume that the photo-generated electrons from CdSe can be transferred in both directions, to Pt and to MNP.

We achieved the stationary conditions of eq. (7) for the generation of carriers in MNP and QD quickly after switching on the illumination since all characteristic times in the equations for  $N_{QD}$  and  $N_{MNP}$  are very short. In addition, we assumed the steady-state transfer of electrons from the Pt to the reacting molecules ( $dN_{Pt}/dt = 0$ ). This condition

is satisfied if there is a large number of available molecules for the reaction that is certainly true at small times. We then calculated the rate of transfer of electrons from Pt to molecules:

$$\begin{aligned}
 Rate_{\text{catalysis}} &= \gamma_{Pt \rightarrow \text{molecules}} N_{Pt} = \gamma_{QD \rightarrow Pt} \gamma_{\text{eff1},MNP} \cdot \frac{\alpha_{MNP} \cdot I_0}{\hbar \omega_0} + \gamma_{QD \rightarrow Pt} \gamma_{\text{eff1},QD} \cdot \frac{\alpha_{QD} \cdot I_0}{\hbar \omega_0} \\
 \gamma_{\text{eff1},MNP} &= \frac{\gamma_{MNP \rightarrow QD}}{\left( \gamma_{\text{relax},MNP} + \gamma_{MNP \rightarrow QD} \right)} \left( \gamma_{QD \rightarrow Pt} + \gamma_{QD \rightarrow MNP} + \gamma_{\text{rec},QD} - \frac{\gamma_{MNP \rightarrow QD} \gamma_{QD \rightarrow MNP}}{\left( \gamma_{\text{relax},MNP} + \gamma_{MNP \rightarrow QD} \right)} \right) \quad (8) \\
 \gamma_{\text{eff1},QD} &= \frac{1}{\left( \gamma_{QD \rightarrow Pt} + \gamma_{QD \rightarrow MNP} + \gamma_{\text{rec},QD} - \frac{\gamma_{MNP \rightarrow QD} \gamma_{QD \rightarrow MNP}}{\left( \gamma_{\text{relax},MNP} + \gamma_{MNP \rightarrow QD} \right)} \right)}
 \end{aligned}$$

Specifically, we considered this rate as the rate of transfer of photo-excited electrons to molecules for the use in the catalytic reaction. Eq. (8) shows the important property of the system: The majority of hot carriers may come from the MNP since  $\alpha_{MNP} \gg \alpha_{QD}$ ; In addition, since the dynamics of the chemical reaction is slow ( $1/\gamma_{\text{exp}} \sim 20\text{mins}$ ), the population of Pt ( $N_{Pt}$ ) is a slow function of time.

The electron-transfer rates in eq. (7) are not known but can be assumed. The hot electron relaxation rate in MNP  $\gamma_{\text{relax},MNP} \sim 1\text{ps}$  and the recombination rate in QD is much slower,  $\gamma_{\text{rec},QD} \sim 10\text{ns}$ [213][214]. Then we calculated the absorption rates of the particles. For this, we used a model of a local dielectric function for both QD and MNP.  $Q_{\text{tot}}$ ,  $Q_{MNP}$ , and  $Q_{QD}$  are defined as the absorption rates of the whole NP, the plasmonic metal subunit and the semiconductor subunits. Then the absorption rates for the system become:

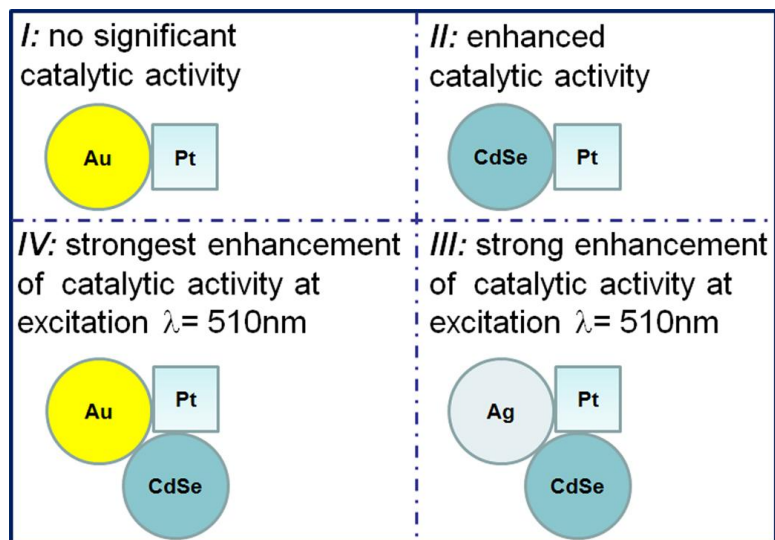


Fig 3.19. Summary of our model reasoning on the nanooligomers that have been tested out both in theory and experiment.

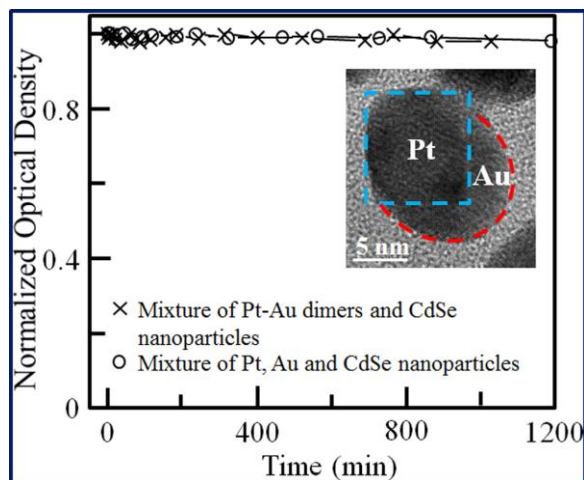


Fig 3.20. Photocatalysis measurement with physical mixture of Pt-Au heterodimers and CdSe nanoparticles (1:1 molar ratio). For comparison, result of physical mixture of Pt, Au and CdSe nanoparticles (1:1:1 molar ratio) is also presented. No noticeable photocatalytic activity was observed with Pt-Au heterodimers under light illumination at 510nm. This control experiment confirms that the path for the hot plasmonic electrons from the plasmonic  $\text{Au}_x\text{Ag}_y$  subunit directly to the Pt subunit is not active. Therefore we can safely exclude this reaction path in our model.

$$\begin{aligned}
Q_{tot} &= Q_{MNP} + Q_{QD} = \dot{\int} \langle j \cdot E \rangle_t, \\
Q_{MNP} &= \text{Im} \left( \epsilon_{metal} \right) \frac{W}{2\rho_{MNP}} \dot{\int} E_w^{in} E_w^{in*} dV, \quad (9) \\
Q_{QD} &= \text{Im} \left( \epsilon_{CdSe} \right) \frac{W}{2\rho_{QD}} \dot{\int} E_w^{in} E_w^{in*} dV,
\end{aligned}$$

where  $\epsilon_{metal}$  and  $\epsilon_{CdSe}$  are the local dielectric constants and  $E_w^{in}$  is the amplitude of electric field. The results reflect an average of all directions of incidence of the external electromagnetic wave. We took the dielectric functions of the pure metals (Au and Ag) from the tables[215]. To calculate the dielectric constant of the Au-Ag alloy of MNPs, we used the standard Maxwell-Garnett formula. In terms of the treatment of the semiconductor component, we neglected size-dependent energy level quantization of charge carriers in the CdSe QDs. We felt this choice was justified because the QDs are large in size (10nm). We discovered that the problem of absorption of two spherical nanocrystals should be solved numerically using the standard multi-pole expansion method[207].

Figure 3.21 shows the results. The absorption by MNP is typically an order of magnitude larger than that of the QD. Therefore, the hot plasmonic electrons generated in a MNP can dominate the photo-catalytic response. We supported this hypothesis by observing the strong increase in the reaction rate ( $\gamma_{exp}$ ) in our experiments (Fig 3.18). It is reasonable to assume that this rate is proportional to the number of available photo-generated electrons in Pt:  $\gamma_{exp} \propto N_{Pt}$ .

Eq.(8) allowed us to calculate the theoretical rate of electron transfer  $Rate_{catalysis}$ . If the transfer of electrons from the MNP and the QD to the Pt nanoparticles was fast, we assumed that all optically-generated electrons were able to reach the Pt nanoparticle and



$$Rate_{catalysis,max} = g_{Pt \rightarrow molecules} N_{Pt} \gg (a_{MNP} + a_{QD}) \frac{I_0}{h\nu_0} \mu(a_{MNP} + a_{QD}) \quad (10)$$

Therefore, the rate becomes proportional to the total absorption cross-section of the complex. This is the maximum rate of electron transfer for a catalytic reaction that our system can achieve. Below reflects how we used this simple result.

Our next step was to examine the influence of the composition of the Pt-Au<sub>x</sub>Ag<sub>y</sub>-CdSe nanostructure on the photocatalytic activity. First of all, we saw that the metal Au/Ag MNP of 10nm size was not able to strongly increase absorption by the QD (Fig 3.21). The calculated enhancement was only 25% for the smallest separation, whereas the experimentally observed enhancement of  $\gamma_{exp}$  was ~14.8. This can only be explained by involving the hot plasmonic electrons from a MNP. We transferred these plasmonic electrons, created by light hitting the plasmon resonance of Au-MNP, to CdSe and then to Pt to enhance the photo-catalysis. We should note that the importance of hot electrons created by the optical excitation of the localized surface plasmon resonance has been recently proven in the case of structures composed of a plasmonic structure and a semiconductor quantum well[216].

We discovered more evidence to support the importance of the plasmonic hot electrons. The increase of catalytic activity in the experiment  $\gamma_{exp, Pt-CdSe-Au}/\gamma_{exp, Pt-CdSe} \sim 14.8$  was in semi-quantitative agreement with the increase of the absorption cross section of the CdSe-Au complex compared with the CdSe QD:

$$\alpha_{QD+MNP}/\alpha_{QD} \approx (\alpha_{MNP,0} + 1.25 \cdot \alpha_{MNP,0})/\alpha_{QD,0} \sim 14 \quad (11)$$

where  $\alpha_{QD,0}$  and  $\alpha_{MNP,0}$  are the cross sections for the isolated QD and MNP nanoparticles, respectively. Figure 3.18 shows how we plotted the normalized rate constant,

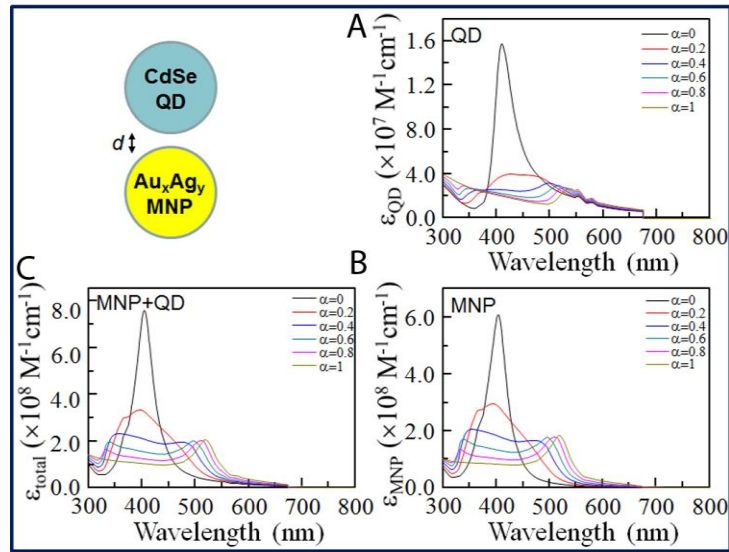


Fig 3.21 Calculated extinctions of the QD (A) and MNP (B) subunits inside the QD-MNP nanooligomers for various fractions  $\alpha = \chi_{Au} = V_{Au}/V_{tot}$ . (C) The total extinction of the QD-MNP nanooligomers. The inter-particle gap  $d=0.5\text{nm}$  and the NP sizes are equal to 10nm.

$\gamma_{exp,Au/Ag}/\gamma_{exp,Ag}$ , which we took from the experiment. Since  $\alpha_{QD+MNP} \gg \alpha_{QD}$ , we may assume in the first order approximation that the rate  $Rate_{catalysis}$  should be governed by the MNP cross-section  $\alpha_{MNP}$ , i.e.  $Rate_{catalysis} \propto \alpha_{MNP}$ . Since the excitation  $\lambda_0 = 510\text{nm}$  is in resonance with the Au-plasmon and off-resonant with the Ag-MNP, the relative rate  $Rate_{catalysis,Au/Ag}/Rate_{catalysis,Ag} \approx \alpha_{MNP,Au/Ag}/\alpha_{MNP,Ag}$  should be an increasing function of  $\chi_{Au}$ . We present our calculations in Figure 3.18. The increase in absorption was 10-fold as we moved from  $\chi_{Au}=0$  to  $\chi_{Au}=0.8$ . This is in semi-qualitative agreement with the observed 5-fold increase in the catalytic activity. We can attain a stronger agreement between the theory and the experiment if we assume that all electrons from the MNP and the QD are

transferred to the Pt. This would be the upper limit from the enhancement effect. Then,

$$Rate_{\text{catalysis}} \propto \alpha_{MNP+QD}$$

and  $Rate_{\text{catalysis,Au-CdSe}}/Rate_{\text{catalysis,Ag-CdSe}} = \alpha_{MNP+QD,Au-CdSe}/\alpha_{MNP+QD,Ag-CdSe} \sim 5$  at  $\lambda_0 = 510\text{nm}$ .

We see that the upper bound for the enhancement is in excellent agreement with the experiment. The above two arguments show that it is impossible to explain the increase in the catalytic activity without examining the transfer of hot plasmonic electrons from a MNP to Pt via a CdSe QD.

Figure 3.19 presents a summary of our observations that can only be explained by involving the electron transfer from a MNP to Pt via a semiconductor QD.

## 6.4 Result and Discussion

In comparison to the photocatalytic reaction rate of the Pt-CdSe, we observed a 14.8-fold enhancement in the Pt-Au<sub>0.80</sub>Ag<sub>0.20</sub>-CdSe nanooligomers (Fig 3.18C). Structural characterization of nanooligomers before and after photocatalytic reactions suggests that all nanooligomeric structures remained intact (Fig 3.24). We attribute the significant enhancement of the photocatalytic reaction rate of Pt-Au<sub>x</sub>Ag<sub>y</sub>-CdSe nanooligodimers to synergistic interaction between the localized surface plasmon resonance of the Au<sub>x</sub>Ag<sub>y</sub> and the Pt-CdSe subunits, according to the key control experiments summarized below: (1) the reaction rate increases as the ratio of  $x/y$  increases at the constant illumination wavelength of 510nm (Fig 3.18D, Fig 3.23A). This is consistent with our observation that localized surface plasmon resonance energy of alloyed Au<sub>x</sub>Ag<sub>y</sub> nanoparticles can be monotonically tuned by its ratio of  $x/y$  (Fig 3.22B) [217]; (2) wavelength dependence of the reaction rate for a nanooligomer shows excellent agreement with its plasmonic

resonance profile (Fig 3.25). We systematically carried out illumination wavelength dependent measurements for a nanooligomer with fixed x/y ratio, and the result suggested that our observation of the photocatalysis enhancement was related to the optical excitation of localized plasmon resonance of AuxAg<sub>y</sub> subunits; and (3) absence of synergistic coupling showed no enhancement of photocatalytic reaction rate.

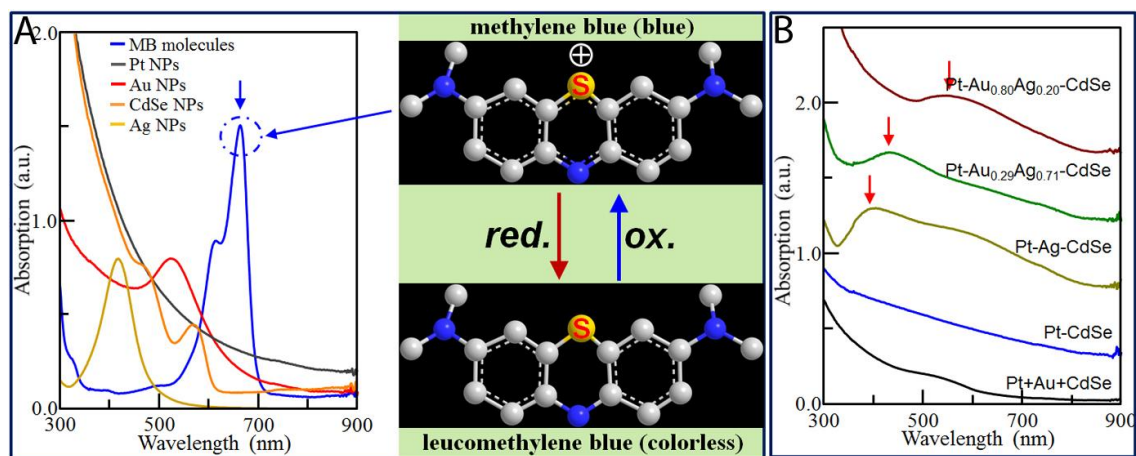


Fig 3.22. Plasmon-mediated photocatalytic reduction of the MB molecule. (A) Optical absorption spectra of the MB molecules in aqueous solution (blue), Pt nanocubes (dark gray), 7.0nm Au nanoparticles (red), 5.0nm CdSe nanoparticles (orange), and 10.0nm Ag nanoparticles (dark yellow). There are two characteristic absorption peaks of the MB molecules at 667nm and 609nm, respectively. Intensities of both peaks decrease once the MB molecules are reduced in solution, as schematically shown in the right. Particularly, in our current report the absorption peak intensity at 667nm (highlighted by dashed circle) is recorded with time and is used to monitor photocatalytic process of the MB molecules. (B) Optical absorption spectra of Pt-Au<sub>x</sub>Ag<sub>y</sub>-CdSe nanooligomers with different ratio of x/y. It can be seen that as the ratio of x/y increases the energy of plasmonic peak (highlighted by the red arrow) is shifted from that of pure Ag nanoparticles towards that of pure Au nanoparticles. For comparison, absorption spectra of both Pt-CdSe heterodimers and the physical mixture of Pt

nanoparticles, Au nanoparticles and CdSe nanoparticles with molar ratio of 1:1:1 are also shown.

We performed similar measurements with two physical mixtures of 1:1:1 molar ratio of Au, Pt and CdSe nanoparticles and 1:1 molar ratio of Au-Pt dimers and CdSe nanoparticles, but did not observe any enhancement of the photocatalytic reaction rate from either sample (Fig 3.19).

In order to elucidate the reaction pathway and an enhancement mechanism behind plasmon-mediated photocatalysis, we developed a plasmon-photocatalytic model by considering both electron transfer and near-field electromagnetic enhancement mechanisms (Fig 3.18A) [209]. To compare experimental observations, we normalized the reaction rate among samples with a different  $x/y$  ratio, and summarized the results in the Figure 3.18D. We first evaluated the non-radiative energy transfer from metal plasmons to semiconductor excitons caused by a localized intense electromagnetic field in close proximity to a photo-excited plasmonic nanostructure[209][218]. While this mechanism can indeed lead to a maximum  $\sim 1.6$  fold increase in the reaction rate as compared with that of Pt-CdSe heterodimers, it cannot explain the observed dependence of the enhancement factor on the ratio of  $x/y$  (Fig 3.18D), suggesting that this mechanism does not play the dominant role. Alternatively, we discovered that after the plasmon of  $\text{Au}_x\text{Ag}_y$  subunits is excited, it can quickly dissociate into hot electron and hole carriers in the Fermi sea before reaching a phonon-induced thermal equilibrium. Recent studies have shown that such energetic carriers are able to cross high-energy potential barriers[216]. If this mechanism is valid, then it immediately suggests that there are two possible hot plasmonic electron transfer routes based on the structural arrangement of

subunits within the nanooligomers. One route is from the plasmonic  $\text{Au}_x\text{Ag}_y$  subunit directly to the catalytic Pt subunit and then to the nearby MB molecules; and the other follows the path of the  $\text{Au}_x\text{Ag}_y$  subunit to the CdSe subunit to the Pt subunit, and then to the MB molecules. We evaluated both routes and results are presented in Figure 3.18D. It is clear that the second pathway agreed very well with our experimental results. The substantial disagreement between first pathway and experiment was also consistent with the experimental fact that we were unable to find evidence of photocatalytic enhancement in the Pt-Au heterodimers (Fig 3.19). This mechanism, driven by hot-plasmon, is further supported when comparing the non-plasmonic Pt-CdSe heterodimers. Our model predicted a 14-fold enhancement, taking into consideration the effect of the Au-CdSe subunits, which shows excellent agreement with our experimental observation of a 14.8-fold increase in the reaction rate. As compared with former systems, such as the Au-TiO<sub>2</sub>, whose explanations for the plasmonic effect in the photo-catalytic reactions remain controversial[218]–[220], our Pt-Au<sub>x</sub>Ag<sub>y</sub>-CdSe nanooligomers possessed well-defined plasmonic and semiconductor subunits, occupying adjacent facets of catalytic Pt nanocube with direct and efficient contact between the Au<sub>x</sub>Ag<sub>y</sub> and CdSe. This nanostructure provides explicit evidence that hot energetic electrons are required in order to achieve the strongly enhanced photocatalysis. The excellent agreement between our model and controlled experiments clearly revealed that the hot plasmonic electrons assisted the photocatalysis mechanism through the plasmonic-semiconducting-catalytic pathway.

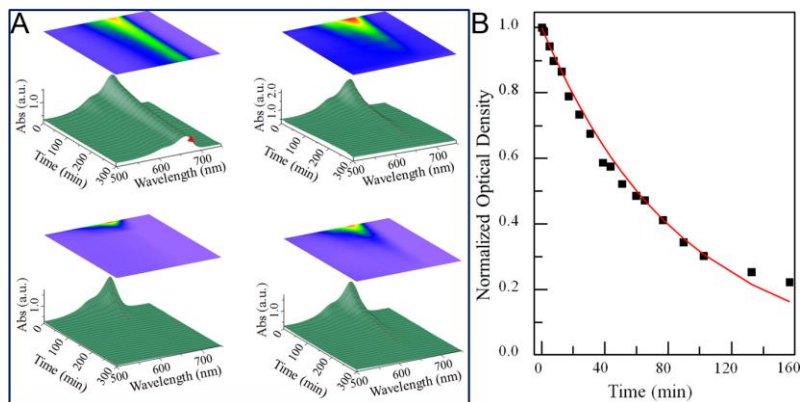


Fig 3.23. Optical characterization of photocatalytic reduction of the MB molecules by nanooligomers. (A) Normalized time-dependent optical absorption spectra of the MB molecules with (top left) Pt-CdSe heterodimers; (top right) Pt-Ag-CdSe nanooligomers; (bottom right) Pt-Au<sub>0.29</sub>Ag<sub>0.71</sub>-CdSe nanooligomers; and (bottom left) Pt-Au<sub>0.80</sub>Ag<sub>0.20</sub>-CdSe nanooligomers. A two-dimensional projection of time-dependent absorption spectra is also presented, and summarized in the Fig 3.20B. All data were obtained under monochromatic light illumination at 510nm. (B) A typical single exponential fit to the time evolution of optical density of the MB molecules at 667nm to extract photocatalytic reaction rate.

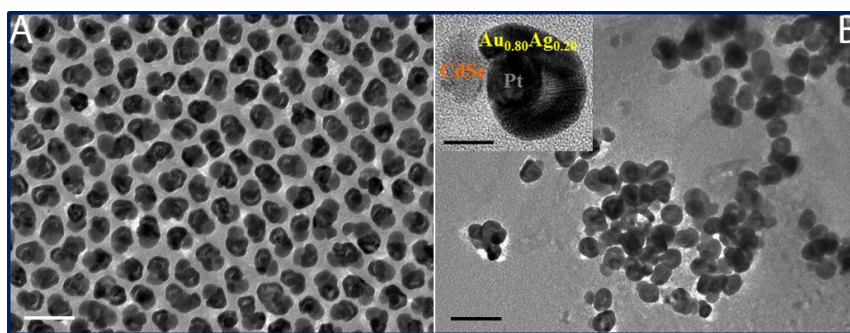


Fig 3.24. Low- and high-resolution TEM characterizations of Pt-Au<sub>0.80</sub>Ag<sub>0.20</sub>-CdSe nanooligomers before (A) and after (B) photocatalytic reactions. No change of structure and composition was detected after the photocatalytic reactions, and the nanooligomers remained intact during the reaction. Scale bar of low-resolution TEM images, 50nm. Scale bar of high-resolution TEM images, 10nm.

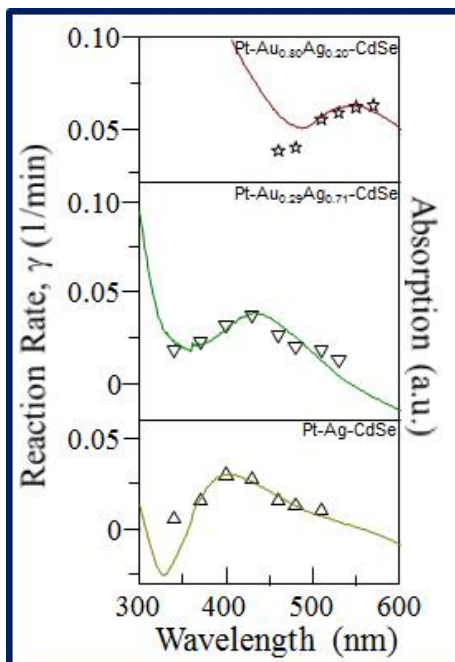


Fig 3.25. Excitation wavelength-dependent photocatalytic measurements of the Pt-Au<sub>x</sub>Ag<sub>y</sub>-CdSe nanooligomers. For each nanooligomer, corresponding absorption spectrum (color solid curve) is overlaid with the dependence of reaction rate (colored symbols) for comparison.

Our study immediately opens up exciting new opportunities, ranging from multifunctional nature-mimicking nanoscale oligomeric structures to a wide range of enabled applications. Our versatile synthetic methodology allows for the high quality and precise engineering of nanooligomers, including compositions, dimensions and structural arrangements, but also allows for the hierarchical growth of complex oligomeric nanostructures, thus offering novel synergistic functionality in a pre-designed structure for both fundamental understanding and technological applications. By combining a new type of plasmon-photocatalytic nanooligomers with theoretical modeling, we were able to demonstrate that energetic hot plasmonic electrons drive the photocatalytic process and play a key role in the catalytic enhancement. The confirmed transfer path of hot



plasmonic electrons via the semiconductor subunits revealed the requirement of a nanoscale design in which the plasmonic and semiconducting subunits have a common transparent interface. This allows a scientist to evaluate the possibility of an upper limit of a plasmon-assisted photocatalytic reaction and guide the design towards highly efficient structures, provided that synergistic interactions among different components in a nanooligomer can be properly tailored as demonstrated in our new synthetic approach.

## *7. Conclusion*

We have developed a new synthetic scheme for various combinations of nanooligomers, starting from Au and Pt seeds and performing a UV-vis absorption measurement on Au-CdSe. We also accomplished the control of additions to different modules. Furthermore, we were able to fully validate the hypothesis that hot plasmonic electrons induce catalytic enhancement. Based on controlled experiments, we excluded other possibilities and located the major transfer path of hot plasmonic electrons via semiconductor subunits. Our work provides a general method for constructing nanooligomers. Merging existing synthesis schemes enabled us to overcome their individual deficiencies, regardless of the different electronic interactions at the boundaries of various modules. Given the diversity of materials that are amenable to such reactions[221], this full-synthesis allows for the construction of nanooligomers with exceptional structural complexity for use in many fields.

# Chapter IV: Morphology Modulations on CdSe-Seeded CdS Nanorods, Nanospindles, and Nanobullets

*Hath not the potter power over the clay, to make one vessel unto honor, and another unto dishonor?*

*- The Bible, Romans*

## *1. Introduction*

Epitaxially grown core/shell semiconductor nanocrystals are an important class of hybrid nanostructures. While the shell can protect the core material from external influences such as etching from the solvent or oxidation[222], it also has other effects on the core, depending on the bandgaps and the relative position of electronic energy levels of the involved semiconductors[223].

Three cases have been proposed as type-I, reverse type-I, and type-II band alignment. In the two type-I cases, the bandgap of the shell material is either larger or smaller than that of the core, and both electrons and holes are confined in the core or in the shell. In the latter, either the valence-band edge or the conduction band edge of the shell material was located in the bandgap of the core, which led to a spatial separation of the hole and the electron to different regions of the nanostructure upon excitation.

CdSe/CdS rodlike core/shell structure has type-I band alignment (Fig 4.1). In CdSe/CdS nanostructure, the conduction band offset of 0.2 eV and small effective mass is not sufficient to confine the electron to the CdSe core, but instead delocalize it through

the entire system[224], [225], which can be a 1-D character in a 1-D rodlike shell. In contrast, the hole is mainly confined to the CdSe core because of its high effective mass and the large valence band offset of 0.55 eV. It usually gains 0-D character because of the spherical CdSe.

Consequently, the shell improved the optical properties of the CdSe/CdS nanostructure[225]–[227]. Such core/shell nanocrystals typically show brighter photoluminescence and electroluminescence. The efficiency of this unusual photoluminescence of CdSe-seeded CdS nanorods can be as high as 76% [228], and it is more than 50% for CdSe-seeded CdS tetrapods[229].

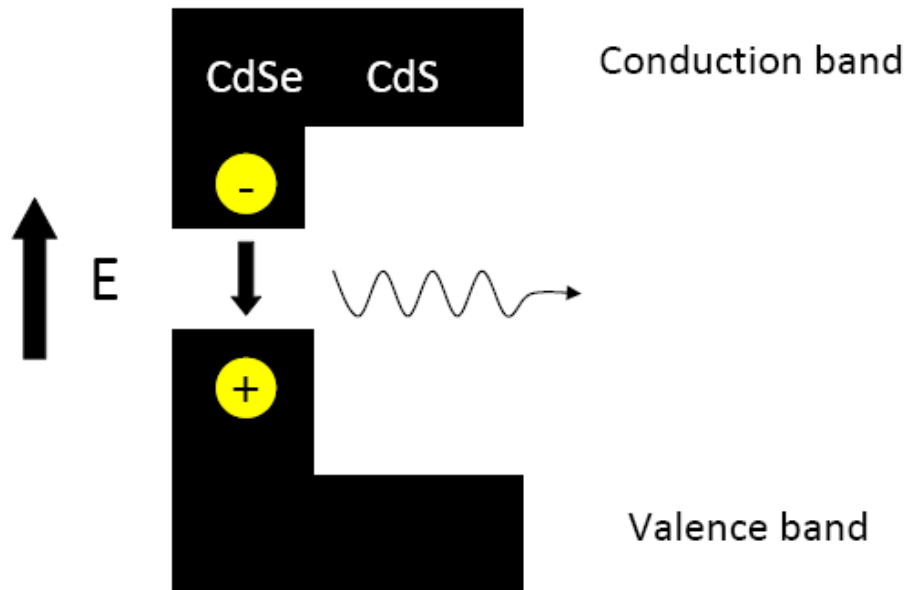


Fig 4.1. Schematic representation of energy-level alignment in the core-shell CdSe/CdS nanostructure. The upper edge of the lower ‘L’ shape corresponds to the positions of the valence-band edge of the core (center) and shell materials; the lower edge of the upper ‘L’ shape corresponds to the positions of the conduction-band edge of the core (center) and shell materials.

The phase of the CdSe seeds is the key factor in determining the morphology of CdSe/CdS nanostructures. People used Wurtzite(W)-CdSe NPs to promote epitaxial growth of CdS along their unique c-axis, producing a rod shape[228]. On the other hand, zinc blended(ZB)-CdSe NPs can function as the seed for growing CdS tetrapods because they possess a higher order of symmetry[230].

Scientists have developed various methods to deposit Au nanocrystals onto the tips of CdS nanorods and tetrapods in order to gain a better understanding of the interface between metals and semiconductors[231]–[234]. These methods have also been applied to CdSe/CdS nanostructures in an effort to partially reduce the fluorescence quenching that occurs at the interface between Au and semiconductors[234], during which it also has been observed that the Au deposition was extremely sensitive to the crystal index of the deposition site on CdS tips[231].

We have developed a new, seed-type growth approach to fabricating colloidal nanospindles and nanobullets (Fig 4.2b, c) in addition to common nanorods (Fig 4.2a). These nanostructures have totally different symmetries, considering the shape of the CdS shell and the position of the CdSe core.

We successfully deposited Au on every CdSe/CdS nanostructure synthesized. We examined their optical properties and TEM images before and after the deposition of Au. We were able to use this data to locate the position of the CdSe core in the nanostructure, which was too tiny for us to identify by EDS mapping.

## 2. Experimental Techniques

### 2.1 The Synthesis of CdS/CdSe Nanorods

W-CdSe seeds were synthesized based on a modified route from the published literature [235]. All conditions were followed though we replaced cadmium myristate with cadmium oleate as the Cd precursor. The diameter of CdSe NPs was confirmed by the absorption spectra to be  $3.4 \pm 0.3\text{nm}$ .

The CdSe core/CdS nanorod (Fig 4.2a) was synthesized following Carbone's work [228]. In a typical synthesis of CdSe/CdS nanorods *via* seeded growth, 0.057g cadmium oxide (CdO) was mixed in a 50mL three-neck flask together with 3.000g tri-n-octylphosphine oxide (TOPO), 0.290g octadecylphosphonic acid (ODPA) and 0.080g hexylphosphonic acid (HPA). The mixture melted at 60°C to form a transparent solution under the blow of N<sub>2</sub>. After keep degassing with N<sub>2</sub> for 1 hour at 150°C, the solution was heated to 350°C. At this step 1.500 g of tri-n-octylphosphine (TOP) was injected, after which the temperature recovered to 350°C for the injection of the solution, which contained 0.120g dissolved in 1.500g TOP and 200 μl (always  $8 \times 10^{-8}$  mol CdSe quantum dots in total). The resulting solution was quickly injected in the flask. After injection, the temperature dropped to 270-300°C and it soon recovered within 2 minutes to the pre-injection temperature. The nanocrystals were allowed to grow for about 8 minutes after the injection, after which the heating mantle is removed. The CdSe/CdS nanorods in the solution were mixed with 1:5 volume ratio of methanol to precipitate the nanorods, which were collected by the centrifuging at 4000rpm/20min.

## 2.2 The Synthesis of CdS/CdSe Nanospindles/Nanobullets

CdSe/CdS nanospindles (Fig 4.2b) were synthesized by growing CdS on W-CdSe seeds[236]. In a 50ml three-neck flask, 0.207g CdO, 1.08g ODPa, 0.075g ethylphosphonic acid (EPA), and 3.350g TOPO were degassed at 120°C for 1h. The mixture turned into clear solution when it was heated to 280°C under N<sub>2</sub>, after which the solution was cooled to 120°C and degassed for 2h. Then the reaction mixture was heated to 300°C for the synthesis of nanospindles. 1.500g TOP was injected into the solution when temperature reached 300°C. 0.650g TOPS (1.61mmol S) was injected into the solution, followed after 40s by the injection of seeds (2mg W-CdSe NPs) in 0.500g TOP. The reaction temperature was slowly increased to 315°C (~1°C /min) and kept at 315°C for 20 min before cooling down to room temperature. CdSe/CdS nanobullets (Fig 4.2c) were acquired at 265 °C for 20 min instead of 315 °C.

## 2.3 The Growth of Au tips on CdSe/CdS

The growth of Au on CdSe/CdS nanorods, nanospindles and nanobullets was based on a modified route from the published literature [234]. For the preparation of the Au precursor, Au stock solution was prepared by dissolving KAuCl<sub>4</sub> (60 mg) in water (5 mL), yielding a homogenous clear yellow solution. Dodecylamine (DDA) stock solution was prepared by dissolving 280 mg of DDA in 10 mL ethanol. DDA acted as the ligand to transfer Au<sup>3+</sup> from water to the organic phase.

In an open top vial, Au (40 µL) stock solution was mixed with DDA (1 mL) stock solution at 60°C. After 3 min of continuous stirring, a mixture containing 5 µM CdSe/CdS nanostructures in toluene (1 mL) and ODPa (6 mg) was added. The vial then

was degassed by N<sub>2</sub>. The mixture was allowed to react for a fixed amount of time, typically for 30 hours, and then was quenched by 1:5 volume ratio of methanol. The product was collected by centrifuging, which can be dispersed into 1mL toluene as seeds. If necessary, second deposition of Au helped it to reach a desirable size.

### *3. Result and Discussion*

We did not acquire sufficient CdSe/CdS tetrapods. Instead, the majority of the product was nanospindles mixed with a few T-shaped CdSe/CdS (Fig 4.2b) or nanobullets at a lower temperature (Fig 4.2c), all of which have different arm lengths. Temperature and reaction time were the main factors that caused this problem. Generally speaking, a higher temperature extends the arm length, not only by providing CdS monomers with more thermal energy to overcome the energy barrier, but also by driving ligand molecules off the surface of formed CdS to allow incoming monomers to deposit more efficiently. We found that the growing speed of CdS was slow even at a high temperature, judging from the late appearance of a typical orange fluorescence from CdSe/CdSe, which indicated that the system stayed in the growth stage most of the time, instead of in self-focusing or Ostwald ripening.

Discrepancies in the morphologies were apparent. Figure 4.2a shows typical CdSe/CdS nanorods with CdSe cores which we characterized to be located at 1/3 or 1/4 the length of the nanorods, by both geometric phase analysis and EDS mapping[228][229][237]. This was due to a higher reactivity of the {001} facet of W-CdSe to support faster CdS growth compared to the  $\{00\bar{1}\}$  facet, as one unreconstructed {001} surface is purely cadmium finished, whereas the  $\{00\bar{1}\}$  is pure selenium[238]. We also observed the

sequential impact of this difference from the deposition of Au onto CdSe/CdS nanorods (Fig 4.3a, b). Ninety-two percent of CdSe/CdS nanorods ended up with a single Au nucleation site on one tip and two on the other. This can readily be explained as CdS nanorods inherited the difference between the  $\{001\}$  and the  $\{00\bar{1}\}$  of W-CdSe during their epitaxial growth. If one facet was finished with the sulfur layer, it showed a strong affinity with Au[239]. Symmetrical CdS shells were also deformed during the Au deposition. One tip evolved into a bullet shape due to the etching of DDA and water[233], which also suggested the inequity between the two tips.

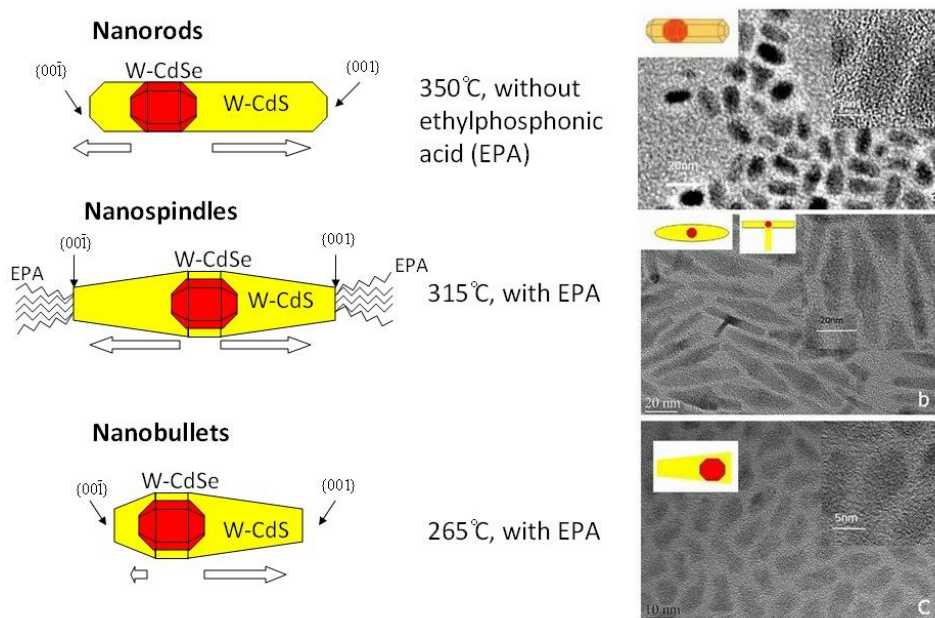


Fig 4.2. TEM images of synthesized CdSe/CdS nanostructures under different conditions, with schematic demonstrations of location of the CdSe core. (a) CdSe/CdS nanorods with an average length of  $19 \pm 2$  nm and an aspect ratio of 2.5:1(c:a). The average diameter of the CdSe/CdS nanorods is 7 nm. (b) CdSe/CdS nanospindles with an average length of  $55 \pm 5$  nm. 15% of total nanostructures are tetrapods, and 3% are T-shaped. (c) CdSe/CdS nanobullets with an average length of  $15 \pm 3$  nm.



For the nanospindle, we assumed the CdSe core to be in the center. We observed an increase in diameter of the CdSe core (Fig 4.2b) around the middle, which was a result of the slower growth rate of CdS on the other facets of CdSe, except for the  $\{001\}$  and the  $\{00\bar{1}\}$ , which in turn revealed the position of the CdSe core. The similar lengths of the two arms suggested a certain chemical equality between them and a different growth mechanism than the CdSe/CdS nanorod. We ruled out the possibility that the CdSe core was ZB type, because while the arms were parallel, the ZB-CdSe belongs to isometric hextetrahedral class that favors the growth of four equivalent arms. Thus, the CdSe core remained as W-CdSe, and EPA was not able to facilitate a full phase transition of W-CdSe to ZB-CdSe in the synthesis. (About 15% of W-CdSe annealed into ZB-CdSe, judging by the percentage of tetrapods.) Meanwhile, the  $\{001\}$  and  $\{00\bar{1}\}$  facets of W-CdS were related to the  $\{111\}$  facet of ZB-CdSe by a stacking fault. Thus, instead of binding to the  $\{111\}$  facet of ZB-CdSe at the high temperature to lower its surface energy to speed up the phase transition of W-CdSe to ZB-CdSe[236], EPA, in fact, attached to the  $\{001\}$  facet of CdS when the layer consisted of cadmium atoms[74]. During CdS growth, although the two arms started from different facets of W-CdSe, they experienced the same iteration of one atom layer replacing the other, when EPA had the same chance to bind to them to slow down their growth. Eventually, these two arms grew to a similar length.

The deposition of Au on the nanospindle also supported this assumption, as we found no major difference in the size of Au between the two tips (Fig 4.3e). The asymmetry around the center was because EPA is only effective on particular facets of the tip, and it cannot eliminate the growth difference on the side. The occasional T-shaped (Fig 4.2b)

nanostructures were the result of extra arms growing on the {100} facet of W-CdSe, as slower-growing facets eventually replaced the fastest growing facets[240].

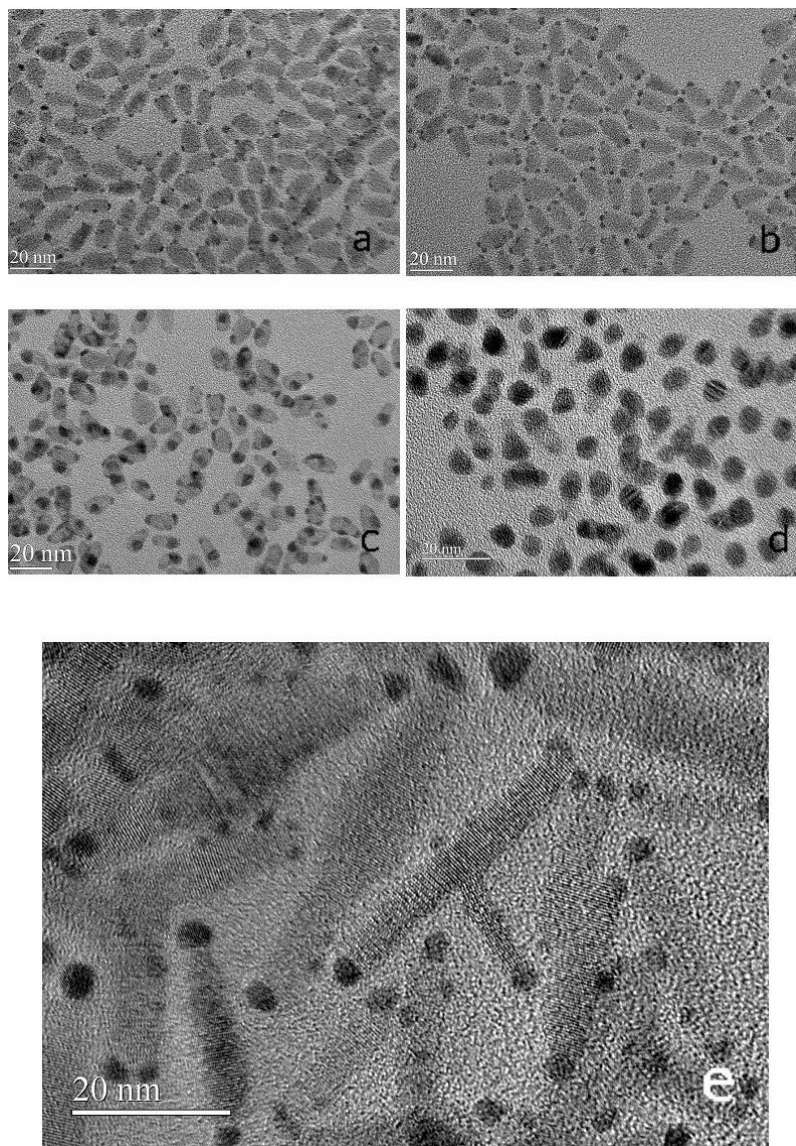


Fig. 4.3. The deposition of Au on the tips of CdSe/CdS nanostructures. (a)/(b) First Au deposition on CdSe/CdS nanorods with 1x/2x ODPAs as the capping ligand. (c) Second Au deposition on CdSe/CdS nanorods. Au dots in the middle of the nanorods were on defects caused by the etching of DDA and water. (d) Second Au deposition on CdSe/CdS nanobullets. For most of the nanobullets, Au dots were only on one side. (e) Second Au deposition on CdSe/CdS nanospindles.

We located the CdSe core for the nanobullet shape on the side (Fig 4.2c), based on a few facts. The CdSe core still remained as W-CdSe, as EPA only functions at a high temperature, and 265°C cannot guarantee a more complete phase transition than 315°C can. The low temperature actually did not drive EPA to bind to the {001} facet of CdS selectively, but it deepened the discrepancy of the growth speed between the {001} and facets of W-CdSe. As a result, it left the core more at the edge of the nanostructure. Additional evidence came from the Au deposition and the absorption spectra (Fig 4.3d, Fig 4.4), which further solidifies our claim. Figure 4.3d shows that large Au dots were present solely on one side of the nanobullets, which is evidence of the inequivalent chemical environments between the two tips. Meanwhile, the absorption spectra in Figure 4.4 present an interesting picture. Compared to the well-sheltered CdSe in nanospindles and nanorods, the CdSe absorption peak from nanobullets had the least amount of red-shift. This indicates a lack of semiconductor materials around CdSe[241], which suggests that CdSe was either shallowly embedded in CdS or partially exposed.

Interesting physics can also be found on the absorption spectra from the Au-tipped CdSe-CdS nanorods. Figure 4.5 shows that when Au is tiny, the weak plasmon does not affect the whole profile of the absorption. We did not see any major difference between the pure CdSe/CdS nanorods and CdSe/CdS-Au in Figure 4.3a and Figure 4.3b. When the deposited Au reached a size comparable to that of Fig 3.9, its plasmons started to overlap partially with the band gap of 3.4nm CdSe cores, which resulted in a slight blue-shift of the CdSe absorption peak (blue line in Fig 4.5), although the shift was not comparable to the scale of the red-shift in Figure 3.16, because holes were constrained in the CdSe core to support a limited plasmon–exciton coupling.

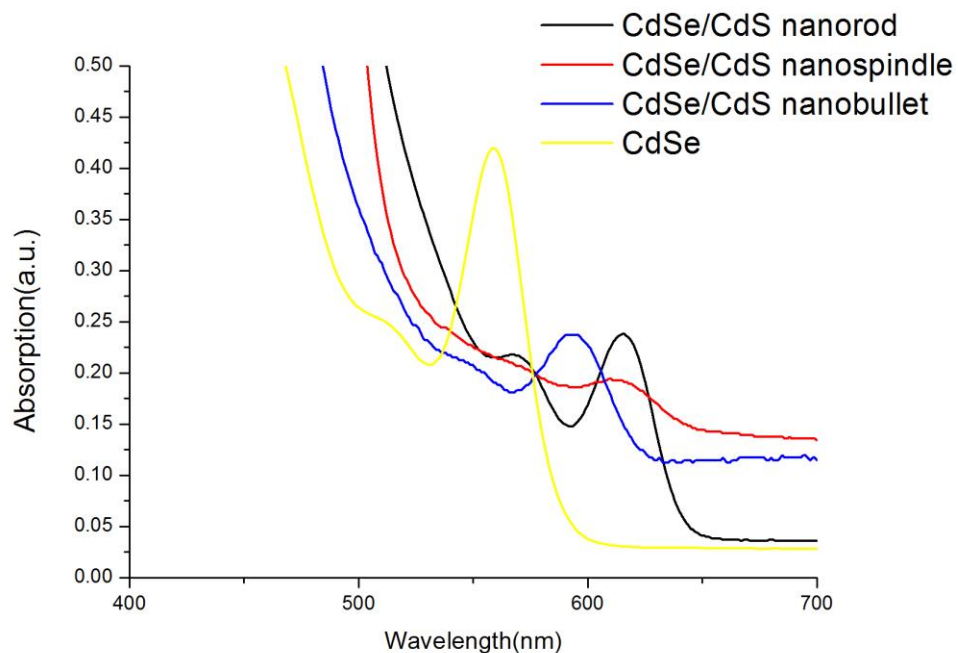


Fig 4.4. Comparison of absorption spectra between CdSe/CdS nanostructures with same-size CdSe cores. The data have been normalized.

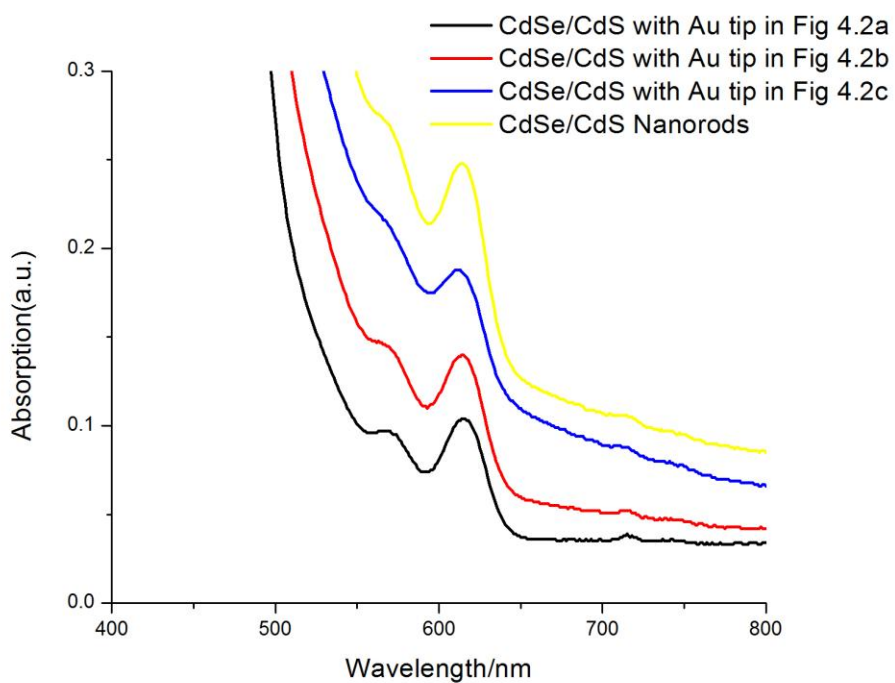


Fig 4.5. Absorption spectra for Au-tipped CdSe-CdS nanorods.

#### *4. Conclusion*

We have demonstrated the control of morphologies of a CdSe/CdS system to acquire at least three types of nanostructures by tuning conditions in the synthesis, which came from different growth mechanisms. Nanospindles may lead to a linear CdSe/CdS nanostructure with mirror symmetry to maintain a similar chemical property for both arms and to allow for ordered assemblies that tetrapods cannot form. One of the predictable applications is to deposit Au of the same size on the CdS tips.

## Chapter V: Summary and Future Work

The composition, component and morphology of various nanostructures determine their properties. The human capacity to manipulate materials at nanoscale can provide answers to the emerging energy, resource, and pollution problems that we face today. The tunability of properties and functionalities of noble metal, magnetic, and semiconductor nanostructures, as well as the interactions between them offer invaluable opportunities to investigate fundamentals of science and to explore exciting applications.

In our single-source molecular precursor approach, we were able to acquire two stoichiometric iron-rich iron sulfide NPs,  $\text{Fe}_3\text{S}$ , and  $\text{Fe}_3\text{S}_2$ , which normally exist only under extreme conditions. Our approach enriched our knowledge of two materials unavailable under regular laboratory conditions, and has important implications for research on the formation of planets and their magnetic fields. On the other hand, our synthetic method is very general and can be extended to other stoichiometric syntheses to acquire new compounds with specific ratios of elements. We also found that both as-synthesized  $\text{Fe}_3\text{S}$  and  $\text{Fe}_3\text{S}_2$  NPs are made of amorphous magnetic nanostructures, a finding that considerably interesting from both fundamental and application viewpoints.

We have demonstrated how versatile and powerful our new synthetic scheme is in Chapter III, both by the number of combinations of nanooligomers we fabricated and the perfect quality of their monocrystalline features. The data from UV-vis absorption spectra of Au-CdSe suggested a coupling between excitons and plasmons, which provided us with abundant information about the interface between Au and CdSe. We proposed the hypothesis of hot plasmonic electron-induced catalytic enhancement verified it through theoretical calculations and controlled experiments. This full-synthesis framework has the

potential to construct nanooligomers with exceptional structural complexity for applications in many fields. One potentially useful nanooligomer we considered is the Pt-CdSe-Au. Based on the proposed mechanism, we should be able to see a maximum enhancement of catalytic capabilities from this nanostructure, which has no interface between Pt and Au. Such a structure will generate a unidirectional energy flow, from Au to CdSe and then to Pt, to yield the best result.

In Chapter IV, knowledge of the crystal structure helped us to understand a few unusual CdSe/CdS core shell structures and the growth mechanism behind them. They were the result of competing growth kinetics of CdS on different facets of CdSe, which showed us that with a stronger ligand to bind to both the  $\{001\}$  and  $\{00\bar{1}\}$  facets of CdS, we could acquire symmetric linear CdSe/CdS nanorods, which are a good supplement to the current asymmetric synthesis of CdSe/CdS nanorods.

## References

- [1] Richard P. Feynman, "There's Plenty of Room at the Bottom," *Engineering and Science*, pp. 22–36, Feb. 1960.
- [2] J. Hu, T. W. Odom, and C. M. Lieber, "Chemistry and Physics in One Dimension: Synthesis and Properties of Nanowires and Nanotubes," *Accounts of Chemical Research*, vol. 32, no. 5, pp. 435–445, May 1999.
- [3] C. Q. Sun, Y. Wang, B. K. Tay, S. Li, H. Huang, and Y. B. Zhang, "Correlation between the Melting Point of a Nanosolid and the Cohesive Energy of a Surface Atom," *The Journal of Physical Chemistry B*, vol. 106, no. 41, pp. 10701–10705, Oct. 2002.
- [4] Chao Wang, Hideo Daimon, and Shouheng Sun, "Dumbbell-like Pt–Fe<sub>3</sub>O<sub>4</sub> Nanoparticles and Their Enhanced Catalysis for Oxygen Reduction Reaction," *Nano Lett.*, vol. 9, pp. 1493–1496, 2009.
- [5] P. Chen, X. Wu, X. Sun, J. Lin, W. Ji, and K. L. Tan, "Electronic structure and optical limiting behavior of carbon nanotubes," *Physical review letters*, vol. 82, no. 12, pp. 2548–2551, 1999.
- [6] Andrew D. Maynard, "Nanotechnology: The next big thing, or much ado about nothing?," *Ann. Occup. Hyg.*, vol. 51, pp. 1–12, 2007.
- [7] X. Wang, L. Zhi, and K. Müllen, "Transparent, Conductive Graphene Electrodes for Dye-Sensitized Solar Cells," *Nano Letters*, vol. 8, no. 1, pp. 323–327, Jan. 2008.
- [8] M. M. J. Treacy, T. W. Ebbesen, and J. M. Gibson, "Exceptionally high Young's modulus observed for individual carbon nanotubes," *Nature*, vol. 381, pp. 678–680, Jun. 1996.
- [9] S. Moein Moghimi, A. Christy Hunter, and J. Clifford Murray, "Nanomedicine: current status and future prospects," *The FASEB Journal*, vol. 19, pp. 311–330, Mar. 2005.
- [10] Laszlo B Kish, "End of Moore's law: thermal (noise) death of integration in micro and nano electronics," *Physics Letters A*, vol. 305, no. 3–4, pp. 144–149, Dec. 2002.
- [11] I. Freestone, N. Meeks, M. Sax, and C. Higgitt, "The lycurgus cup—a roman nanotechnology," *Gold Bulletin*, vol. 40, no. 4, pp. 270–277, 2007.
- [12] S. K. Ghosh and T. Pal, "Interparticle Coupling Effect on the Surface Plasmon Resonance of Gold Nanoparticles: From Theory to Applications," *Chemical Reviews*, vol. 107, pp. 4797–4862, Nov. 2007.
- [13] Norio Taniguchi, "On the basic concept of nanotechnology," *Proc. Intl. Conf. Prod. Eng. Tokyo, Part II, Japan Society of Precision Engineering*, 1974.
- [14] H.W. Kroto, J.R. Heath, S. C. O'Brien, R. F. Curl, and R. E. Smalley, "C<sub>60</sub>: Buckminsterfullerene," *Nature*, vol. 318, pp. 162–163, 1985.
- [15] Sumio Iijima and Toshinari Ichihashi, "Single-shell carbon nanotubes of 1-nm diameter," *Nature*, vol. 363, pp. 603–605, 1993.
- [16] K. S. Novoselov, A. K. Geim, S. V. Morozov, D. Jiang, M. I. Katsnelson, I. V. Grigorieva, S. V. Dubonos, and A. A. Firsov, "Two-dimensional gas of massless Dirac fermions in graphene," *Nature*, vol. 438, no. 7065, pp. 197–200, Nov. 2005.



- [17] M. G. Bawendi, M. L. Steigerwald, and L. E. Brus, "The quantum mechanics of larger semiconductor clusters ('quantum dots')," *Annual Review of Physical Chemistry*, vol. 41, no. 1, pp. 477–496, 1990.
- [18] Victor I. Klimov, *Semiconductor and Metal Nanocrystals: Synthesis, Electronic, and Optical Properties*. CRC Press, 2004.
- [19] T. Ohtsuka, J. Kawamata, Z. Zhu, and T. Yao, "p-type CdSe grown by molecular beam epitaxy using a nitrogen plasma source," *Applied Physics Letters*, vol. 65, no. 4, p. 466, 1994.
- [20] W. Guo, J. J. Li, Y. A. Wang, and X. Peng, "Luminescent CdSe/CdS Core/Shell Nanocrystals in Dendron Boxes: Superior Chemical, Photochemical and Thermal Stability," *Journal of the American Chemical Society*, vol. 125, no. 13, pp. 3901–3909, Apr. 2003.
- [21] X. Gao, Y. Cui, R. M. Levenson, L. W. K. Chung, and S. Nie, "In vivo cancer targeting and imaging with semiconductor quantum dots," *Nature biotechnology*, vol. 22, no. 8, pp. 969–976, 2004.
- [22] Alex Zunger and Alberto Franceschetti, "Direct carrier multiplication due to inverse Auger scattering in CdSe quantum dots," *Applied Physics Letters*, vol. 84, no. 13, pp. 2409–2411, Mar. 2004.
- [23] R. D. Schaller, M. A. Petruska, and V. I. Klimov, "Effect of electronic structure on carrier multiplication efficiency: Comparative study of PbSe and CdSe nanocrystals," *Applied Physics Letters*, vol. 87, no. 25, p. 253102, 2005.
- [24] V. L. Colvin, M. C. Schlamp, and A. P. Alivisatos, "Light-emitting diodes made from cadmium selenide nanocrystals and a semiconducting polymer," *Nature*, vol. 370, pp. 354–357, 1994.
- [25] Warren C.W. Chan and Shuming Nie, "Quantum Dot Bioconjugates for Ultrasensitive Nonisotopic Detection," *Science*, vol. 281, pp. 2016–2018.
- [26] Tianyou Zhai, Xiaosheng Fang, Meiyong Liao, Xijin Xu, Haibo Zeng, Bando Yoshio, and Dmitri Golberg, "Comprehensive Review of One-Dimensional Metal-Oxide Nanostructure Photodetectors," *Sensors*, vol. 9, pp. 6504–6529, 2009.
- [27] S. Zhu, J. D. Budai, H. R. Chandrasekhar, P. F. Miceli, H. W. White, and Y. R. Ryu, "Optical and structural properties of ZnO films deposited on GaAs by pulsed laser deposition," *Journal of Applied Physics*, vol. 88, no. 1, pp. 201–204, Jul. 2000.
- [28] P. Davide Cozzoli, et al., "Role of Metal Nanoparticles in TiO<sub>2</sub>/Ag Nanocomposite-Based Microheterogeneous Photocatalysis," *Journal of Physical Chemistry B*, vol. 108, no. 28, pp. 9623–9630, 2004.
- [29] S. Pradhan, D. Ghosh, and S. Chen, "Janus Nanostructures Based on Au–TiO<sub>2</sub> Heterodimers and Their Photocatalytic Activity in the Oxidation of Methanol," *ACS Applied Materials & Interfaces*, vol. 1, no. 9, pp. 2060–2065, Sep. 2009.
- [30] O. I. Mičić, S. P. Ahrenkiel, and A. J. Nozik, "Synthesis of extremely small InP quantum dots and electronic coupling in their disordered solid films," *Applied Physics Letters*, vol. 78, no. 25, p. 4022, 2001.
- [31] D. C. Ralph, C. T. Black, and M. Tinkham, "Nano-particle transistors and energy-level spectroscopy in metals," *Superlattices and microstructures*, vol. 20, no. 3, pp. 389–394, 1996.

- [32] G. Cassano, R. Rossi, M. Alvisi, A. Rizzo, M. A. Signore, Th. Dikonimos, E. Serra, and R. Giorgi, "Enhancement of sensitivity in gas chemiresistors based on carbon nanotube surface functionalized with noble metal (Au, Pt) nanoclusters," *Applied Physics Letters*, vol. 90, no. 17, pp. 173123 – 173123–3, Apr. 2007.
- [33] P. K. Jain, X. Huang, I. H. El-Sayed, and M. A. El-Sayed, "Noble Metals on the Nanoscale: Optical and Photothermal Properties and Some Applications in Imaging, Sensing, Biology, and Medicine," *Accounts of Chemical Research*, vol. 41, no. 12, pp. 1578–1586, Dec. 2008.
- [34] D. Wang and Y. Li, "One-Pot Protocol for Au-Based Hybrid Magnetic Nanostructures via a Noble-Metal-Induced Reduction Process," *Journal of the American Chemical Society*, vol. 132, no. 18, pp. 6280–6281, May 2010.
- [35] Susie Eustis and Mostafa A. El-Sayed, "Why gold nanoparticles are more precious than pretty gold: Noble metal surface plasmon resonance and its enhancement of the radiative and nonradiative properties of nanocrystals of different shapes," *Chem.Soc.Rev.*, vol. 35, pp. 209–217, 2006.
- [36] M. C. Daniel, D. Astruc, and others, "Gold nanoparticles: assembly, supramolecular chemistry, quantum-size-related properties, and applications toward biology, catalysis, and nanotechnology," *Chemical Reviews-Columbus*, vol. 104, no. 1, p. 293, 2004.
- [37] Catherine J. Murphy, Tapan K. Sau, Anand M. Gole, Christopher J. Orendorff, Jinxin Gao, Linfeng Gou, Simona E. Hunyadi, and Tan Li, "Anisotropic Metal Nanoparticles: Synthesis, Assembly, and Optical Applications," *J. Phys. Chem. B*, vol. 109, no. 29, pp. 13857–13870, Jun. 2005.
- [38] Na Tian, Zhi-You Zhou, Shi-Gang Sun, Yong Ding, and Zhong Lin Wang, "Synthesis of Tetrahedral Platinum Nanocrystals with High-Index Facets and High Electro-Oxidation Activity," *Science*, vol. 316, no. 5825, pp. 732–735, May 2007.
- [39] Liang Wang and Yusuke Yamauchi, "Block Copolymer Mediated Synthesis of Dendritic Platinum Nanoparticles," *J. Am. Chem. Soc.*, vol. 131, no. 26, pp. 9152–9153, Jun. 2009.
- [40] Hangxun Xu and Kenneth S. Suslick, "Water-Soluble Fluorescent Silver Nanoclusters - Xu - 2010 - Advanced Materials," *Adv. Mater.*, vol. 22, pp. 1078–1082, 2010.
- [41] C. N. R. Rao and A. K. Cheetham, "Science and technology of nanomaterials: current status and future prospects," *Journal of Materials Chemistry*, vol. 11, no. 12, pp. 2887–2894, 2001.
- [42] L. Wang, H.-Y. Park, S. I.-I. Lim, M. J. Schadt, D. Mott, J. Luo, X. Wang, and C.-J. Zhong, "Core@shell nanomaterials: gold-coated magnetic oxide nanoparticles," *Journal of Materials Chemistry*, vol. 18, no. 23, p. 2629, 2008.
- [43] Ajay Kumar Gupta, Rohan R Naregalkar, Vikas Deep Vaidya, and Mona Gupta, "Recent advances on surface engineering of magnetic iron oxide nanoparticles and their biomedical applications," *Nanomedicine*, vol. 2, pp. 23–39, 2007.
- [44] L. Zhang and T. J. Webster, "Nanotechnology and nanomaterials: Promises for improved tissue regeneration," *Nano Today*, vol. 4, no. 1, pp. 66–80, Feb. 2009.

- [45] Sharon C. Glotzer and Michael J. Solomon, "Anisotropy of building blocks and their assembly into complex structures," *Nature Materials*, vol. 6, pp. 557–562, 2007.
- [46] M. AlHajDarwish, H. Kurt, S. Urazhdin, A. Fert, R. Loloee, W. Pratt, and J. Bass, "Controlled Normal and Inverse Current-Induced Magnetization Switching and Magnetoresistance in Magnetic Nanopillars," *Physical Review Letters*, vol. 93, no. 15, Oct. 2004.
- [47] Shouheng Sun, C. B. Murray, Dieter Weller, Liesl Folks, and Andreas Moser, "Monodisperse FePt Nanoparticles and Ferromagnetic FePt Nanocrystal Superlattices," *Science*, vol. 287(5460), pp. 1989–1992, Mar. 2000.
- [48] K. Inomata, T. Sawa, and S. Hashimoto, "Effect of large boron additions to magnetically hard Fe-Pt alloys," *J. Appl. Phys.*, vol. 64, no. 5, pp. 2537–2540, 1988.
- [49] Dieter Weller and Andreas Moser, "Thermal Effect Limits in Ultrahigh-Density Magnetic Recording," *IEEE Transactions on Magnetics*, vol. 35, pp. 4423–4439, Nov. 1999.
- [50] Vassil Skumryev, Stoyan Stoyanov, Yong Zhang, George Hadjipanayis, Dominique Givord, and Josep Nogues, "Beating the superparamagnetic limit with exchange bias," *Nature*, vol. 423, no. 6942, pp. 850–853, Jun. 2003.
- [51] S. Guo and E. Wang, "Noble metal nanomaterials: Controllable synthesis and application in fuel cells and analytical sensors," *Nano Today*, vol. 6, no. 3, pp. 240–264, Jun. 2011.
- [52] Younan Xia, Yujie Xiong, Byungkwon Lim, and Sara E. Skrabalak, "Shape-Controlled Synthesis of Metal Nanocrystals: Simple Chemistry Meets Complex Physics?," *Angew. Chem. Int. Ed.*, vol. 48, pp. 60–103, 2009.
- [53] M. Sastry, K. Mayya, V. Patil, D. Paranjape, and S. Hegde, "Langmuir-Blodgett films of carboxylic acid derivatized silver colloidal particles: role of subphase pH on degree of cluster incorporation," *The Journal of Physical Chemistry B*, vol. 101, no. 25, pp. 4954–4958, 1997.
- [54] R. W. Murray, "Nanoelectrochemistry: Metal Nanoparticles, Nanoelectrodes, and Nanopores," *Chemical Reviews*, vol. 108, no. 7, pp. 2688–2720, Jul. 2008.
- [55] L. E. Brus, "Electron–electron and electron-hole interactions in small semiconductor crystallites: The size dependence of the lowest excited electronic state," *The Journal of Chemical Physics*, vol. 80, no. 9, p. 4403, 1984.
- [56] L. E. Brus, "A simple model for the ionization potential, electron affinity, and aqueous redox potentials of small semiconductor crystallites," *The Journal of Chemical Physics*, vol. 79, no. 11, p. 5566, 1983.
- [57] C. B. Murray, D. J. Norris, and M. G. Bawendi, "Synthesis and characterization of nearly monodisperse CdE (E= sulfur, selenium, tellurium) semiconductor nanocrystallites," *Journal of the American Chemical Society*, vol. 115, no. 19, pp. 8706–8715, 1993.
- [58] Peter N. Njoki, I-Im S. Lim, Derrick Mott, Hey-Young Park, Bilal Khan, Suprav Mishra, Ravishanker Sujakumar, Jin Luo, and Chuan-Jian Zhong, "Size Correlation of Optical and Spectroscopic Properties for Gold Nanoparticles," *J. Phys. Chem. C*, vol. 111, no. 40, pp. 14664–14669, Sep. 2007.

- [59] T. Ung, L. M. Liz-Marzán, and P. Mulvaney, "Optical Properties of Thin Films of Au@SiO<sub>2</sub> Particles," *The Journal of Physical Chemistry B*, vol. 105, no. 17, pp. 3441–3452, May 2001.
- [60] L. Vayssieres, A. Hagfeldt, and S. E. Lindquist, "Purpose-built metal oxide nanomaterials. The emergence of a new generation of smart materials," *Pure and applied chemistry*, vol. 72, no. 1/2, pp. 47–52, 2000.
- [61] I-Im S. Lim and Chuan-Jian Zhong, "Molecular-Mediated Assembly of Gold Nanoparticles," *Gold Bulletin*, vol. 40, no. 1, pp. 59–66.
- [62] O. V. Cherstiouk, P. A. Simonov, and E. R. Savinova, "Model approach to evaluate particle size effects in electrocatalysis: preparation and properties of Pt nanoparticles supported on GC and HOPG," *Electrochimica Acta*, vol. 48, no. 25–26, pp. 3851–3860, Nov. 2003.
- [63] F. Maillard, E. R. Savinova, P. A. Simonov, V. I. Zaikovskii, and U. Stimming, "Infrared Spectroscopic Study of CO Adsorption and Electro-oxidation on Carbon-Supported Pt Nanoparticles: Interparticle versus Intraparticle Heterogeneity," *The Journal of Physical Chemistry B*, vol. 108, no. 46, pp. 17893–17904, Nov. 2004.
- [64] B. Hammer and J.K. Norskov, "Theoretical surface science and catalysis-calculations and concepts," *Advances in Catalysis*, vol. 45, pp. 71–129, 2000.
- [65] Sanjeev Mukerjee and James McBreen, "Effect of particle size on the electrocatalysis by carbon-supported Pt electrocatalysts: an in situ XAS investigation," *Journal of Electroanalytical Chemistry*, vol. 448, no. 2, pp. 163–171, May 1998.
- [66] Sung Jong Yoo, Tae-Yael Jeon, Kug-Seung Lee, Kyung-Won Park, and Yung-Eun Sung, "Effects of particle size on surface electronic and electrocatalytic properties of Pt/TiO<sub>2</sub> nanocatalysts," *Chem. Commun.*, vol. 46, pp. 794–796, 2010.
- [67] C. R. Henry, "Surface studies of supported model catalysts," *Surface Science Reports*, vol. 31, no. 7, pp. 231–325, 1998.
- [68] X. Batlle and A. Labarta, "Finite-size effects in fine particles: magnetic and transport properties," *Journal of Physics D: Applied Physics*, vol. 35, no. 6, p. R15, 2002.
- [69] Zijlstra H, *Ferromagnetic Materials*, vol. 3. Wohlfarth (Amsterdam: North-Holland).
- [70] D Givord, Q Lu, and M. F. Rosignol, *Science and Technology of Nanostructured Materials*, New York: Plenum Press. Hadjipanayis and G A Prinz, 1991.
- [71] David C. Jiles, *Introduction to magnetism and magnetic materials*, 2nd ed. CRC Press: Boca Raton, 1998.
- [72] W. U. Huynh, "Hybrid Nanorod-Polymer Solar Cells," *Science*, vol. 295, no. 5564, pp. 2425–2427, Mar. 2002.
- [73] X. Feng, L. Feng, M. Jin, J. Zhai, L. Jiang, and D. Zhu, "Reversible Super-hydrophobicity to Super-hydrophilicity Transition of Aligned ZnO Nanorod Films," *Journal of the American Chemical Society*, vol. 126, no. 1, pp. 62–63, Jan. 2004.
- [74] L. Manna, E. C. Scher, and A. P. Alivisatos, "Synthesis of soluble and processable rod-, arrow-, teardrop-, and tetrapod-shaped CdSe nanocrystals,"

- Journal of the American Chemical Society*, vol. 122, no. 51, pp. 12700–12706, 2000.
- [75] X. Peng, L. Manna, W. Yang, J. Wickham, E. Scher, A. Kadavanich, and A. P. Alivisatos, “Shape control of CdSe nanocrystals,” *Nature*, vol. 404, no. 6773, pp. 59–61, 2000.
- [76] L. Li, J. Hu, W. Yang, and A. P. Alivisatos, “Band Gap Variation of Size- and Shape-Controlled Colloidal CdSe Quantum Rods,” *Nano Letters*, vol. 1, no. 7, pp. 349–351, Jul. 2001.
- [77] J. Hu, “Linearly Polarized Emission from Colloidal Semiconductor Quantum Rods,” *Science*, vol. 292, no. 5524, pp. 2060–2063, May 2001.
- [78] M. J. Mulvihill, X. Y. Ling, J. Henzie, and P. Yang, “Anisotropic Etching of Silver Nanoparticles for Plasmonic Structures Capable of Single-Particle SERS,” *Journal of the American Chemical Society*, vol. 132, no. 1, pp. 268–274, Jan. 2010.
- [79] Y. Y. Yu, S. S. Chang, C. L. Lee, and C. R. C. Wang, “Gold nanorods: electrochemical synthesis and optical properties,” *The Journal of Physical Chemistry B*, vol. 101, no. 34, pp. 6661–6664, 1997.
- [80] N. Lopez and J. K. Nørskov, “Catalytic CO Oxidation by a Gold Nanoparticle: A Density Functional Study,” *Journal of the American Chemical Society*, vol. 124, no. 38, pp. 11262–11263, Sep. 2002.
- [81] L. M. Falicov and G. A. Somorjai, “Correlation between catalytic activity and bonding and coordination number of atoms and molecules on transition metal surfaces: Theory and experimental evidence,” *Proc. Natl. Acad. Sci. USA*, vol. 82, pp. 2207–2211, Apr. 1985.
- [82] Q. Song and Z. J. Zhang, “Shape Control and Associated Magnetic Properties of Spinel Cobalt Ferrite Nanocrystals,” *Journal of the American Chemical Society*, vol. 126, no. 19, pp. 6164–6168, May 2004.
- [83] A. Walther and A. H. E. Müller, “Janus particles,” *Soft Matter*, vol. 4, no. 4, p. 663, 2008.
- [84] A. Perro, S. Reculosa, S. Ravaine, E. Bourgeat-Lami, and E. Duguet, “Design and synthesis of Janus micro- and nanoparticles,” *J. Mater. Chem.*, vol. 15, no. 35–36, p. 3745, 2005.
- [85] S. Hwang, D. W. Lim, G. Wang, C. Uher, J. Lahann, and K.-H. Roh, “Anisotropic hybrid particles based on electrohydrodynamic co-jetting of nanoparticle suspensions,” *Physical Chemistry Chemical Physics*, vol. 12, no. 38, p. 11894, 2010.
- [86] Heng Yu, Min Chen, Philip M. Rice, Shan X. Wang, R. L. White, Shouheng Sun, “Dumbbell-like Bifunctional Au–Fe<sub>3</sub>O<sub>4</sub> Nanoparticles,” *Nano Letters*, vol. 5, no. 2, pp. 379–382, 2005.
- [87] S. Reculosa, C. Poncet-Legrand, A. Perro, E. Duguet, E. Bourgeat-Lami, C. Mingotaud, and S. Ravaine, “Hybrid Dissymmetrical Colloidal Particles,” *Chemistry of Materials*, vol. 17, no. 13, pp. 3338–3344, Jun. 2005.
- [88] Anuradha Misra and Marek W. Urban, “Acorn-Shape Polymeric Nano-Colloids: Synthesis and Self-Assembled Films,” *Macromolecular Rapid Communications*, vol. 31, no. 2, pp. 119–127, Jan. 2012.
- [89] H. Gu, R. Zheng, X. X. Zhang, and B. Xu, “Facile one-pot synthesis of bifunctional heterodimers of nanoparticles: a conjugate of quantum dot and

- magnetic nanoparticles,” *Journal of the American Chemical Society*, vol. 126, no. 18, pp. 5664–5665, 2004.
- [90] S. He, H. Zhang, S. Delikanli, Y. Qin, M. T. Swihart, and H. Zeng, “Bifunctional Magneto-Optical FePt–CdS Hybrid Nanoparticles,” *The Journal of Physical Chemistry C*, vol. 113, no. 1, pp. 87–90, Jan. 2009.
- [91] B. T. Jonker, Y. D. Park, B. R. Bennett, H. D. Cheong, G. Kioseoglou, and A. Petrou, “Robust electrical spin injection into a semiconductor heterostructure,” *Physical Review B*, vol. 62, no. 12, p. 8180, 2000.
- [92] A. Sahu, M. S. Kang, A. Kompch, C. Notthoff, A. W. Wills, D. Deng, M. Winterer, C. D. Frisbie, and D. J. Norris, “Electronic Impurity Doping in CdSe Nanocrystals,” *Nano Letters*, vol. 12, no. 5, pp. 2587–2594, May 2012.
- [93] S. C. Erwin, L. Zu, M. I. Haftel, A. L. Efros, T. A. Kennedy, and D. J. Norris, “Doping semiconductor nanocrystals,” *Nature*, vol. 436(7047), pp. 91–94, Jul. 2005.
- [94] P. I. Archer, S. A. Santangelo, and D. R. Gamelin, “Direct Observation of sp–d Exchange Interactions in Colloidal Mn<sup>2+</sup> - and Co<sup>2+</sup>-Doped CdSe Quantum Dots,” *Nano Letters*, vol. 7, no. 4, pp. 1037–1043, Apr. 2007.
- [95] M. P. Mallin and C. J. Murphy, “Solution-Phase Synthesis of Sub-10 nm Au–Ag Alloy Nanoparticles,” *Nano Letters*, vol. 2, no. 11, pp. 1235–1237, Nov. 2002.
- [96] Shouheng Sun, Eric E. Fullerton, Dieter Weller, and C. B. Murray, “Compositionally Controlled FePt Nanoparticle Materials,” *IEEE Transactions on Magnetics*, vol. 37, pp. 1239–1244, Jul. 2001.
- [97] N. Kometani, M. Tsubonishi, T. Fujita, K. Asami, and Y. Yonezawa, “Preparation and Optical Absorption Spectra of Dye-Coated Au, Ag, and Au/Ag Colloidal Nanoparticles in Aqueous Solutions and in Alternate Assemblies,” *Langmuir*, vol. 17, no. 3, pp. 578–580, Feb. 2001.
- [98] Sheng Peng, Jaemin Kim, and Shouheng Sun, “Chemical synthesis, self-assembly and applications of magnetic nanoparticles,” *Annu. Rev. Nano Res*, vol. 3, pp. 275–316, 2010.
- [99] J. Gao, H. Gu, and B. Xu, “Multifunctional Magnetic Nanoparticles: Design, Synthesis, and Biomedical Applications,” *Accounts of Chemical Research*, vol. 42, no. 8, pp. 1097–1107, Aug. 2009.
- [100] Y. Jun, J. Seo, and J. Cheon, “Nanoscaling Laws of Magnetic Nanoparticles and Their Applicabilities in Biomedical Sciences,” *Accounts of Chemical Research*, vol. 41, no. 2, pp. 179–189, Feb. 2008.
- [101] A. H. Latham and M. E. Williams, “Controlling Transport and Chemical Functionality of Magnetic Nanoparticles,” *Accounts of Chemical Research*, vol. 41, no. 3, pp. 411–420, Mar. 2008.
- [102] An-Hui Lu, E. L. Salabas, and Ferdi Schu<sub>th</sub>, “Magnetic Nanoparticles: Synthesis, Protection, Functionalization, and Application,” *Angew. Chem. Int. Ed.*, vol. 46, pp. 1222–1244, 2007.
- [103] Chao Wang and Shouheng Sun, “Chemical Synthesis of Monodisperse Magnetic Nanoparticles,” in *Handbook of Magnetism and Advanced Magnetic Materials*, 2007.
- [104] R.C. Sharma and Y.A. Chang, “Thermodynamics and phase relationships of transition metal-sulfur systems: Part III. Thermodynamic properties of the Fe-S

- liquid phase and the calculation of the Fe-S phase diagram,” *Metallurgical Transactions B*, vol. 10, no. 1, pp. 103–108.
- [105] A. J. Stewart, M. W. Schmidt, W. van Westrenen, and C. Liebske, “Mars: A New Core-Crystallization Regime,” *Science*, vol. 316, no. 5829, pp. 1323–1325, Jun. 2007.
- [106] A. G. Ritchie, P. G. Bowles, and D. P. Scattergood, “Lithium-ion/iron sulphide rechargeable batteries,” *Journal of Power Sources*, vol. 136, no. 2, pp. 276–280, Oct. 2004.
- [107] A. Ennaoui and H. Tributsch, “Iron sulphide solar cells,” *Solar Cells*, vol. 13, pp. 197–200, 1984.
- [108] A. Ennaoui, S. Fiechter, H. Goslowsky, and H. Tributsch, “Photoactive Synthetic Polycrystalline Pyrite ( FeS<sub>2</sub> ),” *J. Electrochem. Soc.*, vol. 132, no. 7, pp. 1579–1582, 1985.
- [109] A. Ennaoui, S. Fiechter, W. Jaegermann, and H. Tributsch, “Photoelectrochemistry of Highly Quantum Efficient Single- Crystalline n- FeS<sub>2</sub> (Pyrite),” *J. Electrochem. Soc.*, vol. 133, no. 1, pp. 97–106, 1986.
- [110] A. S. Barnard and S. P. Russo, “Morphological Stability of Pyrite FeS<sub>2</sub> Nanocrystals in Water,” *The Journal of Physical Chemistry C*, vol. 113, no. 14, pp. 5376–5380, Apr. 2009.
- [111] A. A. Bharde, R. Y. Parikh, M. Baidakova, S. Jouen, B. Hannoyer, T. Enoki, B. L. V. Prasad, Y. S. Shouche, S. Ogale, and M. Sastry, “Bacteria-Mediated Precursor-Dependent Biosynthesis of Superparamagnetic Iron Oxide and Iron Sulfide Nanoparticles,” *Langmuir*, vol. 24, no. 11, pp. 5787–5794, Jun. 2008.
- [112] J. M. Soon, L. Y. Goh, K. P. Loh, Y. L. Foo, L. Ming, and J. Ding, “Highly textured, magnetic Fe(1+x)S nanorods grown on silicon,” *Appl. Phys. Lett.*, vol. 91, no. 8, p. 084105, 2007.
- [113] Manashi Nath, Amitava Choudhury, Asish Kundu, and C. N. R. Rao, “Synthesis and Characterization of Magnetic Iron Sulfide Nanowires,” *Adv. Mater.*, vol. 15, pp. 2098–2111, Dec. 2003.
- [114] S. Kamada, H. Terasaki, E. Ohtani, T. Sakai, T. Kikegawa, Y. Ohishi, N. Hirao, N. Sata, and T. Kondo, “Phase relationships of the Fe–FeS system in conditions up to the Earth’s outer core,” *Earth and Planetary Science Letters*, vol. 294, no. 1–2, pp. 94–100, May 2010.
- [115] Y. Fei, C. M. Bertka, and L. W. Finger, “High-pressure iron-sulfur compound, Fe<sub>3</sub>S<sub>2</sub>, and melting relations in the Fe–FeS system,” *Science*, vol. 275, no. 5306, pp. 1621–1623, 1997.
- [116] C. T. Seagle, A. J. Campbell, D. L. Heinz, G. Shen, and V. B. Prakapenka, “Thermal equation of state of Fe<sub>3</sub>S and implications for sulfur in Earth’s core,” *Journal of Geophysical Research*, vol. 111, no. B6, 2006.
- [117] YingWei Fei, Jie Li, Constance M. Bertka, and Charles T. Prewitt, “Structure type and bulk modulus of Fe<sub>3</sub>S, a new iron-sulfur compound,” *American Mineralogist*, vol. 85.
- [118] J.-F. Lin, Y. Fei, W. Sturhahn, J. Zhao, H. Mao, and R. J. Hemley, “Magnetic transition and sound velocities of Fe<sub>3</sub>S at high pressure: implications for Earth and

- planetary cores,” *Earth and Planetary Science Letters*, vol. 226, no. 1–2, pp. 33–40, Sep. 2004.
- [119] B. Ryzhenko and G. C. Kennedy, “The effect of pressure on the eutectic in the system Fe-FeS,” *Am. J. Sci*, vol. 273, pp. 803–810, 1973.
- [120] Thomas M. Usselman, “Experimental approach to the state of the core; Part I, The liquidus relations of the Fe-rich portion of the Fe-Ni-S system from 30 to 100 kb,” *Am. J. Sci*, vol. 275, pp. 278–290, Mar. 1975.
- [121] R. Brett and P. M. Bell, “Melting relations in the Fe-rich portion of the system Fe&z. sbnd; FeS at 30 kb pressure,” *Earth and Planetary Science Letters*, vol. 6, no. 6, pp. 479–482, 1969.
- [122] D. M. Sherman, “Stability of possible Fe-FeS and Fe-FeO alloy phases at high pressure and the composition of the Earth’s core,” *Earth and Planetary Science Letters*, vol. 132, no. 1, pp. 87–98, 1995.
- [123] Bin Chen, Lili Gao, Ken-ichi Funakoshi, and Jie Li, “Thermal expansion of iron-rich alloys and implications for the Earth’s core,” *PNAS*, vol. 104, pp. 9162–9167, May 2007.
- [124] Y. Zhang, Y. Tang, K. Lee, and M. Ouyang, “Catalytic and Catalyst-free Synthesis of CdSe Nanostructures with Single-Source Molecular Precursor and Related Device Application,” *Nano Letters*, vol. 9, no. 1, pp. 437–441, Jan. 2009.
- [125] P. V. Radovanovic, C. J. Barrelet, S. Gradecak, F. Qian, and C. M. Lieber, “General Synthesis of Manganese-Doped II–VI and III–V Semiconductor Nanowires,” *Nano Letters*, vol. 5, no. 7, pp. 1407–1411, Jul. 2005.
- [126] M. Afzaal, D. J. Crouch, P. O’Brien, J. Raftery, P. J. Skabara, A. J. P. White, and D. J. Williams, “The synthesis, X-ray structures and CVD studies of some group 11 complexes of iminobis(diisopropylphosphine selenides) and their use in the deposition of I/III/VI photovoltaic materials,” *Journal of Materials Chemistry*, vol. 14, no. 2, p. 233, 2004.
- [127] C. J. Barrelet, Y. Wu, D. C. Bell, and C. M. Lieber, “Synthesis of CdS and ZnS Nanowires Using Single-Source Molecular Precursors,” *Journal of the American Chemical Society*, vol. 125, no. 38, pp. 11498–11499, Sep. 2003.
- [128] S. L. Cumberland, K. M. Hanif, A. Javier, G. A. Khitrov, G. F. Strouse, S. M. Woessner, and C. S. Yun, “Inorganic Clusters as Single-Source Precursors for Preparation of CdSe, ZnSe, and CdSe/ZnS Nanomaterials,” *Chemistry of Materials*, vol. 14, no. 4, pp. 1576–1584, Apr. 2002.
- [129] Hiroshi Ogino, Shinji Inomata, and Hiromi Tobita, “Abiological Iron–Sulfur Clusters,” *Chem. Rev.*, vol. 98, pp. 2093–2122, 1998.
- [130] P. V. Rao and R. H. Holm, “Synthetic analogues of the active sites of iron-sulfur proteins,” *Chemical reviews*, vol. 104, no. 2, pp. 527–560, 2004.
- [131] J. Z. Wen, C. F. Goldsmith, R. W. Ashcraft, and W. H. Green, “Detailed Kinetic Modeling of Iron Nanoparticle Synthesis from the Decomposition of Fe(CO)<sub>5</sub>,” *Journal of Physical Chemistry C*, vol. 111, no. 15, pp. 5677–5688, Apr. 2007.
- [132] L. S. Sunderlin, D. Wang, and R. R. Squires, “Metal (iron and nickel) carbonyl bond strengths in Fe (CO)<sub>n</sub>-and Ni (CO)<sub>n</sub>,” *Journal of the American Chemical Society*, vol. 114, no. 8, pp. 2788–2796, 1992.
- [133] B. Xia, H. Cheng, V. Bandarian, G. H. Reed, and J. L. Markley, “Human ferredoxin: overproduction in *Escherichia coli*, reconstitution in vitro, and



- spectroscopic studies of iron-sulfur cluster ligand cysteine-to-serine mutants,” *Biochemistry*, vol. 35, no. 29, pp. 9488–9495, 1996.
- [134] A. Cabot, V. F. Puentes, E. Shevchenko, Y. Yin, L. Balcells, M. A. Marcus, S. M. Hughes, and A. P. Alivisatos, “Vacancy Coalescence during Oxidation of Iron Nanoparticles,” *Journal of the American Chemical Society*, vol. 129, no. 34, pp. 10358–10360, Aug. 2007.
- [135] S. Peng, C. Wang, J. Xie, and S. Sun, “Synthesis and Stabilization of Monodisperse Fe Nanoparticles,” *Journal of the American Chemical Society*, vol. 128, no. 33, pp. 10676–10677, Aug. 2006.
- [136] D. Farrell, S. A. Majetich, and J. P. Wilcoxon, “Preparation and Characterization of Monodisperse Fe Nanoparticles,” *The Journal of Physical Chemistry B*, vol. 107, no. 40, pp. 11022–11030, Oct. 2003.
- [137] E. V. Shevchenko, D. V. Talapin, A. L. Rogach, A. Kornowski, M. Haase, and H. Weller, “Colloidal Synthesis and Self-Assembly of CoPt<sub>3</sub> Nanocrystals,” *Journal of the American Chemical Society*, vol. 124, no. 38, pp. 11480–11485, Sep. 2002.
- [138] R. D. Adams, J. E. Babin, P. Mathur, K. Natarajan, and J. G. Wang, “Cluster synthesis. 25. Synthesis and characterization of new mixed-metal cluster complexes by metal-metal exchange. Reactions of the sulfido cluster complexes M<sub>3</sub>(CO)<sub>9</sub>(u<sub>3</sub>-CO)(u<sub>3</sub>-S)(M=Fe, Ru and Os) with W(CO)<sub>5</sub>L (L= CO or PMe<sub>2</sub>Ph),” *Inorganic Chemistry*, vol. 28, no. 8, pp. 1440–1445, 1989.
- [139] R. B. King, “Organosulfur Derivatives of Metal Carbonyls. II. The Reaction between Triiron Dodecacarbonyl and Certain Episulfide Derivatives,” *Inorganic Chemistry*, vol. 2, no. 2, pp. 326–327, 1963.
- [140] E. C. Stoner and E. P. Wohlfarth, “A Mechanism of Magnetic Hysteresis in Heterogeneous Alloy,” *Philosophical Transactions of the Royal Society of London. Series A, Mathematical and Physical Sciences*, vol. 240, pp. 599–642, May 1948.
- [141] J. García and G. Subías, “The Verwey transition—a new perspective,” *Journal of Physics: Condensed Matter*, vol. 16, no. 7, p. R145, 2004.
- [142] S. Lee, A. Fursina, J. T. Mayo, C. T. Yavuz, V. L. Colvin, R. G. Sumesh Sofin, I. V. Shvets, and D. Natelson, “Electrically driven phase transition in magnetite nanostructures,” *Nature Materials*, vol. 7, no. 2, pp. 130–133, Dec. 2007.
- [143] V. V. Shchennikov and S. V. Ovsyannikov, “Is the Verwey transition in Fe<sub>3</sub>O<sub>4</sub> magnetite driven by a Peierls distortion?,” *Journal of Physics: Condensed Matter*, vol. 21, no. 27, p. 271001, Jul. 2009.
- [144] J. B. Yang, “Magnetic and structural studies of the Verwey transition in Fe(3- $\delta$ )O<sub>4</sub> nanoparticles,” *Journal of Applied Physics*, vol. 95, no. 11, p. 7540, 2004.
- [145] T. J. Daou, G. Pourroy, S. Bégin-Colin, J. M. Grenèche, C. Ulhaq-Bouillet, P. Legaré, P. Bernhardt, C. Leuvrey, and G. Rogez, “Hydrothermal Synthesis of Monodisperse Magnetite Nanoparticles,” *Chemistry of Materials*, vol. 18, no. 18, pp. 4399–4404, Sep. 2006.
- [146] V. V. Hoang, “Molecular dynamics simulation of liquid and amorphous Fe nanoparticles,” *Nanotechnology*, vol. 20, no. 29, p. 295703, Jul. 2009.
- [147] S. M. Yusuf, M. D. Mukadam, J. M. De Teresa, M. R. Ibarra, J. Kohlbrecher, A. Heinemann, and A. Wiedenmann, “Structural and magnetic properties of

- amorphous iron oxide,” *Physica B: Condensed Matter*, vol. 405, no. 4, pp. 1202–1206, Feb. 2010.
- [148] Vesselin N. Paunov and Olivier J. Cayre, “Supraparticles and ‘Janus’ Particles Fabricated by Replication of Particle Monolayers at Liquid Surfaces Using a Gel Trapping Technique,” *Advanced Materials*, vol. 16, no. 9–10, p. 788, May 17.
- [149] A. P. Alivisatos, “Semiconductor Clusters, Nanocrystals, and Quantum Dots,” *Science*, vol. 271, pp. 933–937, Feb. 1996.
- [150] H. Gu, Z. Yang, J. Gao, C. K. Chang, and B. Xu, “Heterodimers of nanoparticles: Formation at a liquid-liquid interface and particle-specific surface modification by functional molecules,” *Journal of the American Chemical Society*, vol. 127, no. 1, pp. 34–35, 2005.
- [151] A S Shirinyan and M Wautelet, “Phase separation in nanoparticles,” *Nanotechnology*, vol. 15, pp. 1720–1931, 2004.
- [152] Andrew M. Smith, Aaron M. Mohs, and Shuming Nie, “Tuning the optical and electronic properties of colloidal nanocrystals by lattice strain,” *Nature Nanotechnology*, vol. 4, pp. 56–63, 2009.
- [153] Michael Giersig, Thearith Ung, Luis M. Liz-Marzahn, Paul Mulvaney, “Direct observation of chemical reactions in silica-coated gold and silver nanoparticles,” *Advanced Materials*, vol. 9, no. 7, pp. 570–575, 1997.
- [154] D. Belic, R. L. Chantry, Z. Y. Li, and S. A. Brown, “Ag-Au nanoclusters: Structure and phase segregation | Browse,” *Applied Physics Letters*, vol. 99, no. 17, pp. 171912–171914, 2011.
- [155] Yong Qin, Seung-Mo Lee, Anlian Pan, Ulrich Gösele, and Mato Knez, “Rayleigh-Instability-Induced Metal Nanoparticle Chains Encapsulated in Nanotubes Produced by Atomic Layer Deposition,” *Nano Letters*, vol. 8, no. 1, pp. 114–118, 2008.
- [156] M. Zanella, A. Falqui, S. Kudera, L. Manna, M. F. Casula, and W. J. Parak, “Growth of colloidal nanoparticles of group II–VI and IV–VI semiconductors on top of magnetic iron–platinum nanocrystals,” *Journal of Materials Chemistry*, vol. 18, no. 36, p. 4311, 2008.
- [157] Jie Zeng, Cun Zhu, Jing Tao, Mingshang Jin, Hui Zhang, Zhi-Yuan Li, Yimei Zhu, Younan Xia, “Controlling the Nucleation and Growth of Silver on Palladium Nanocubes by Manipulating the Reaction Kinetics,” *Angew. Chem. Int. Ed.*, vol. 51, pp. 2354–2358, 2012.
- [158] D. H. Warrington, “The coincidence site lattice(CSL) and grain boundary(DSC) dislocation for the hexagonal lattice,” *Le Journal de Physique Colloques*, vol. 36, no. C4, pp. C4–87–C4–95, Oct. 1975.
- [159] W. Shi, H. Zeng, Y. Sahoo, T. Y. Ohulchanskyy, Y. Ding, Z. L. Wang, M. Swihart, and P. N. Prasad, “A General Approach to Binary and Ternary Hybrid Nanocrystals,” *Nano Letters*, vol. 6, no. 4, pp. 875–881, Apr. 2006.
- [160] W. Shi, Y. Sahoo, H. Zeng, Y. Ding, M. T. Swihart, and P. N. Prasad, “Anisotropic Growth of PbSe Nanocrystals on Au–Fe<sub>3</sub>O<sub>4</sub> Hybrid Nanoparticles,” *Adv. Mater.*, vol. 18, no. 14, pp. 1889–1894, Jul. 2006.
- [161] Matthew R. Buck, James F. Bondi, and Raymond E. Schaak, “A total-synthesis framework for the construction of high-order colloidal hybrid nanoparticles,” *Nature Chemistry*, vol. 4, pp. 37–44, Nov. 2011.

- [162] Chang Young Kim and Sung-Chul Yi, "Synthesis and characterization of silver-silica heterogeneous nanocomposite particles by an alcohol reducing method," *Journal of Ceramic Processing Research*, vol. 10, no. 4, pp. 462–468, 2006.
- [163] Hubert Kaeslin, *Digital Integrated Circuit Design - From VLSI Architectures to CMOS Fabrication*. Cambridge University Press, 2008.
- [164] Q. Zhang, W. Li, C. Moran, J. Zeng, J. Chen, L. P. Wen, and Y. Xia, "Seed-Mediated Synthesis of Ag Nanocubes with Controllable Edge Lengths in the Range of 30- 200 nm and Comparison of Their Optical Properties," *Journal of the American Chemical Society*, 2010.
- [165] K. K. Caswell, C. M. Bender, and C. J. Murphy, "Seedless, Surfactantless Wet Chemical Synthesis of Silver Nanowires," *Nano Letters*, vol. 3, no. 5, pp. 667–669, May 2003.
- [166] J. Chen, F. Saeki, B. J. Wiley, H. Cang, M. J. Cobb, Z.-Y. Li, L. Au, H. Zhang, M. B. Kimmey, Li, and Y. Xia, "Gold Nanocages: Bioconjugation and Their Potential Use as Optical Imaging Contrast Agents," *Nano Letters*, vol. 5, no. 3, pp. 473–477, Mar. 2005.
- [167] H. Jia, W. Hou, L. Wei, B. Xu, and X. Liu, "The structures and antibacterial properties of nano-SiO<sub>2</sub> supported silver/zinc-silver materials," *Dental Materials*, vol. 24, no. 2, pp. 244–249, 2008.
- [168] D. H. Son, "Cation Exchange Reactions in Ionic Nanocrystals," *Science*, vol. 306, no. 5698, pp. 1009–1012, Nov. 2004.
- [169] Amanda J. Haes and Richard P. Van Duyne, "A Nanoscale Optical Biosensor: Sensitivity and Selectivity of an Approach Based on the Localized Surface Plasmon Resonance Spectroscopy of Triangular Silver Nanoparticles," *Journal of the American Chemical Society*, vol. 124, no. 35, pp. 10596–10604, 2002.
- [170] Yu Lu, Gang L. Liu, and Luke P. Lee, "High-Density Silver Nanoparticle Film with Temperature-Controllable Interparticle Spacing for a Tunable Surface Enhanced Raman Scattering Substrate," *Nano Letters*, vol. 5, pp. 5–9, 2005.
- [171] J. Zhang, Y. Tang, K. Lee, and M. Ouyang, "Nonepitaxial Growth of Hybrid Core-Shell Nanostructures with Large Lattice Mismatches," *Science*, vol. 327, no. 5973, pp. 1634–1638, Mar. 2010.
- [172] S. Peng, Y. Lee, C. Wang, H. Yin, S. Dai, and S. Sun, "A facile synthesis of monodisperse Au nanoparticles and their catalysis of CO oxidation," *Nano Research*, vol. 1, no. 3, pp. 229–234, Sep. 2008.
- [173] M. Chen, J. P. Liu, and S. Sun, "One-Step Synthesis of FePt Nanoparticles with Tunable Size," *Journal of the American Chemical Society*, vol. 126, no. 27, pp. 8394–8395, Jul. 2004.
- [174] Hyunjoo Lee, Susan E. Habas, Sasha Kweskin, Derek Butcher, Gabor A. Somorjai, and Peidong Yang\*, "Morphological Control of Catalytically Active Platinum Nanocrystals," *Angew. Chem. Int. Ed.*, vol. 45, pp. 7824–7828.
- [175] M. Lattuada and T. A. Hatton, "Synthesis, properties and applications of Janus nanoparticles," *Nano Today*, vol. 6, pp. 286–308, 2011.
- [176] L. V. Brown, H. Sobhani, J. B. Lassiter, P. Nordlander, and N. J. Halas, "Heterodimers: plasmonic properties of mismatched nanoparticle pairs," *ACS nano*, vol. 4, no. 2, pp. 819–832, 2010.

- [177] Jiang Jiang, Hongwei Gu, Huilin Shao, Eamonn Devlin, Georgia C. Papaefthymiou, Jackie Y. Ying, “Bifunctional Fe<sub>3</sub>O<sub>4</sub>–Ag Heterodimer Nanoparticles for Two-Photon Fluorescence Imaging and Magnetic Manipulation,” *Advanced Materials*, vol. 20, pp. 4403–4407, 2008.
- [178] H. Hiramatsu and F. E. Osterloh, “A Simple Large-Scale Synthesis of Nearly Monodisperse Gold and Silver Nanoparticles with Adjustable Sizes and with Exchangeable Surfactants,” *Chemistry of Materials*, vol. 16, no. 13, pp. 2509–2511, Jun. 2004.
- [179] Gary L. Miessler and Donald A. Tarr, *Inorganic Chemistry*, 2nd ed. Prentice Hall College Div, 1998.
- [180] Yun Tang and Min Ouyang, “Tailoring properties and functionalities of metal nanoparticles through crystallinity engineering,” *Nature Materials*, vol. 6, pp. 754–759.
- [181] Jingru Shao, Hoda Mirafzal, Jared R. Petker, Janice Lianne S. Cosio, David F. Kelley, Tao Ye, “Nanoscale Organization of GaSe Quantum Dots on a Gold Surface,” *The Journal of Physical Chemistry C*, vol. 113, pp. 19102–19106, 2009.
- [182] Sudip Nath, Sujit Kumar, and Tarasankar Pal, “Solution phase evolution of AuSe nanoalloys in Triton X-100 under UV-photoactivation,” *Chem. Commun.*, pp. 966–967, 2004.
- [183] R. Narayanan and M. A. El-Sayed, “Changing catalytic activity during colloidal platinum nanocatalysis due to shape changes: electron-transfer reaction,” *Journal of the American Chemical Society*, vol. 126, no. 23, pp. 7194–7195, 2004.
- [184] A. Wood, M. Giersig, and P. Mulvaney, “Fermi Level Equilibration in Quantum Dot–Metal Nanojunctions,” *The Journal of Physical Chemistry B*, vol. 105, no. 37, pp. 8810–8815, Sep. 2001.
- [185] N. Bao, L. Shen, T. Takata, and K. Domen, “Self-Templated Synthesis of Nanoporous CdS Nanostructures for Highly Efficient Photocatalytic Hydrogen Production under Visible Light,” *Chemistry of Materials*, vol. 20, no. 1, pp. 110–117, Jan. 2008.
- [186] Einat Elmalem, Aaron E. Saunders, Ronny Costi, Asaf Salant, and Uri Banin, “Growth of Photocatalytic CdSe–Pt Nanorods and Nanonets,” *Advanced Materials*, vol. 20, pp. 4312–4317, 2008.
- [187] H. Chen, X. Kou, Z. Yang, W. Ni, and J. Wang, “Shape- and Size-Dependent Refractive Index Sensitivity of Gold Nanoparticles,” *Langmuir*, vol. 24, no. 10, pp. 5233–5237, May 2008.
- [188] Unyong Jeong, Jong-Uk Kim, and Younan Xia, “Monodispersed Spherical Colloids of Se@CdSe: Synthesis and Use as Building Blocks in Fabricating Photonic Crystals,” *Nano Letters*, vol. 5, pp. 937–942, 2005.
- [189] J. Gao, C. M. Bender, and C. J. Murphy, “Dependence of the Gold Nanorod Aspect Ratio on the Nature of the Directing Surfactant in Aqueous Solution,” *Langmuir*, vol. 19, no. 21, pp. 9065–9070, Oct. 2003.
- [190] N. S. Lewis, “An analysis of charge transfer rate constants for semiconductor/liquid interfaces,” *Annual review of physical chemistry*, vol. 42, no. 1, pp. 543–580, 1991.

- [191] R. A. van Delden, M. K. J. ter Wiel, M. M. Pollard, J. Vicario, N. Koumura, and B. L. Feringa, "Unidirectional molecular motor on a gold surface," *Nature*, vol. 437, no. 7063, pp. 1337–1340, Oct. 2005.
- [192] Chong Xiao, Jie Xu, Kun Li, Jun Feng, Jinlong Yang, and Yi Xie, "Superionic Phase Transition in Silver Chalcogenide Nanocrystals Realizing Optimized Thermoelectric Performance," *Journal of the American Chemical Society*, vol. 134, no. 9, pp. 4287–4293, Feb. 2012.
- [193] R. G. Pearson, "Hard and soft acids and bases," *Journal of the American Chemical Society*, vol. 85, no. 22, pp. 3533–3539, 1963.
- [194] J G Speight and Norbert Adolph Lange, *Lange's Handbook of chemistry*, 16th ed. McGraw-Hill Professional, 2004.
- [195] A. P. Alivisatos, "Melting in Semiconductor Nanocrystals," *Science*, vol. 256, no. 6, pp. 1425–1427, 1992.
- [196] Mario D. Banus, "Pressure Dependence of the Alpha-Beta Transition Temperature in Silver Selenide," *Science*, vol. 147, pp. 732–733.
- [197] C. Sönnichsen, T. Franzl, T. Wilk, G. Von Plessen, and J. Feldmann, "Plasmon resonances in large noble-metal clusters," *New Journal of Physics*, vol. 4, p. 93, 2002.
- [198] L. R. Hirsch, R. J. Stafford, J. A. Bankson, S. R. Sershen, B. Rivera, R. E. Price, J. D. Hazle, and N. J. Halas, "Nanoshell-mediated near-infrared thermal therapy of tumors under magnetic resonance guidance," *PNAS*, vol. 100, pp. 13549–13554, Nov. 2003.
- [199] S. Link and M. A. El-Sayed, "Spectral Properties and Relaxation Dynamics of Surface Plasmon Electronic Oscillations in Gold and Silver Nanodots and Nanorods," *The Journal of Physical Chemistry B*, vol. 103, no. 40, pp. 8410–8426, Oct. 1999.
- [200] R. Costi, A. E. Saunders, E. Elmalem, A. Salant, and U. Banin, "Visible Light-Induced Charge Retention and Photocatalysis with Hybrid CdSe–Au Nanodumbbells," *Nano Letters*, vol. 8, no. 2, pp. 637–641, Feb. 2008.
- [201] T. Mokari, "Selective Growth of Metal Tips onto Semiconductor Quantum Rods and Tetrapods," *Science*, vol. 304, no. 5678, pp. 1787–1790, Jun. 2004.
- [202] R. Costi, G. Cohen, A. Salant, E. Rabani, and U. Banin, "Electrostatic Force Microscopy Study of Single Au–CdSe Hybrid Nanodumbbells: Evidence for Light-Induced Charge Separation," *Nano Letters*, vol. 9, no. 5, pp. 2031–2039, May 2009.
- [203] Z. A. Peng and X. Peng, "Formation of High-Quality CdTe, CdSe, and CdS Nanocrystals Using CdO as Precursor," *Journal of the American Chemical Society*, vol. 123, no. 1, pp. 183–184, Jan. 2001.
- [204] T. D. Krauss and L. E. Brus, "Charge, polarizability, and photoionization of single semiconductor nanocrystals," *Physical Review Letters*, vol. 83, no. 23, pp. 4840–4843, 1999.
- [205] A. L. Aden and M. Kerker, "Scattering of Electromagnetic Waves from Two Concentric Spheres," *Journal of Applied Physics*, vol. 22, no. 10, p. 1242, 1951.
- [206] Jiatao Zhang, Yun Tang, Kwan Lee, and Min Ouyang, "Tailoring light-matter-spin interactions in colloidal hetero-nanostructures," *Nature*, vol. 466, pp. 91–95.

- [207] A. O. Govorov, G. W. Bryant, W. Zhang, T. Skeini, J. Lee, N. A. Kotov, J. M. Slocik, and R. R. Naik, "Exciton-Plasmon Interaction and Hybrid Excitons in Semiconductor-Metal Nanoparticle Assemblies," *Nano Letters*, vol. 6, pp. 984-994, May 2006.
- [208] Ronny Costi, Aaron E. Saunders, and Uri Banin, "Colloidal Hybrid Nanostructures: A New Type of Functional Materials," *Angew. Chem. Int. Ed.*, vol. 49, pp. 4878-4897, 2010.
- [209] S. Linic, P. Christopher, and D. B. Ingram, "Plasmonic-metal nanostructures for efficient conversion of solar to chemical energy," *Nature Materials*, vol. 10, no. 12, pp. 911-921, Nov. 2011.
- [210] V. Subramanian, E. E. Wolf, and P. V. Kamat, "Catalysis with TiO<sub>2</sub>/Gold Nanocomposites. Effect of Metal Particle Size on the Fermi Level Equilibration," *Journal of the American Chemical Society*, vol. 126, no. 15, pp. 4943-4950, Apr. 2004.
- [211] S. C. Warren and E. Thimsen, "Plasmonic solar water splitting," *Energy & Environmental Science*, vol. 5, no. 1, p. 5133, 2012.
- [212] A. Henglein, B. G. Ershov, and M. Malow, "Absorption spectrum and some chemical reactions of colloidal platinum in aqueous solution," *The Journal of Physical Chemistry*, vol. 99, no. 38, pp. 14129-14136, 1995.
- [213] P. K. Jain, W. Qian, and M. A. El-Sayed, "Ultrafast electron relaxation dynamics in coupled metal nanoparticles in aggregates," *The Journal of Physical Chemistry B*, vol. 110, no. 1, pp. 136-142, 2006.
- [214] J. S. Melinger, V. D. Kleiman, D. McMorrow, F. Gröhn, B. J. Bauer, and E. Amis, "Ultrafast dynamics of gold-based nanocomposite materials," *The Journal of Physical Chemistry A*, vol. 107, no. 18, pp. 3424-3431, 2003.
- [215] E. D. Palik, *Handbook of Optical Constants of Solids*. Academic Press, New York, 1985.
- [216] Mark W. Knight, Heidar Sobhani, Peter Nordlander, and Naomi J. Halas, "Photodetection with Active Optical Antennas," *Science*, vol. 332, pp. 702-704, May 2011.
- [217] Chao Wang, Sheng Peng, Ryan Chan, and Shouheng Sun, "Synthesis of AuAg Alloy Nanoparticles from Core/Shell-Structured Ag/Au," *Small*, vol. 5, pp. 567-570, 2009.
- [218] Zhi Wei Seh, Shuhua Liu, Michelle Low, Shuang-Yuan Zhang, Zhaolin Liu, Adnen Mlayah, and Ming-Yong Han, "Janus Au-TiO<sub>2</sub> Photocatalysts with Strong Localization of Plasmonic Near-Fields for Efficient Visible-Light Hydrogen Generation," *Adv. Mater.*, vol. 24, pp. 2310-2314, 2012.
- [219] A. Primo, A. Corma, and H. García, "Titania supported gold nanoparticles as photocatalyst," *Physical Chemistry Chemical Physics*, vol. 13, no. 3, p. 886, 2011.
- [220] Y. Tian and T. Tatsuma, "Mechanisms and Applications of Plasmon-Induced Charge Separation at TiO<sub>2</sub> Films Loaded with Gold Nanoparticles," *Journal of the American Chemical Society*, vol. 127, no. 20, pp. 7632-7637, May 2005.
- [221] L. Carbone and P. D. Cozzoli, "Colloidal heterostructured nanocrystals: Synthesis and growth mechanisms," *Nano Today*, vol. 5, no. 5, pp. 449-493, 2010.

- [222] A. Burns, H. Ow, and U. Wiesner, "Fluorescent core-shell silica nanoparticles: towards 'Lab on a Particle' architectures for nanobiotechnology," *Chem. Soc. Rev.*, vol. 35, no. 11, pp. 1028–1042, 2006.
- [223] Peter Reiss, Myriam Protiere, and Liang Li, "Core/Shell Semiconductor Nanocrystals," *Small*, vol. 5, pp. 154–168, 2009.
- [224] K. F. Jensen and M. G. Bawendi, "(CdSe)ZnS Core-Shell Quantum Dots: Synthesis and Characterization of a Size Series of Highly Luminescent Nanocrystallites," *J. Phys. Chem. B*, vol. 101, pp. 9463–9475, 1997.
- [225] X. Peng, M. C. Schlamp, A. V. Kadavanich, and A. P. Alivisatos, "Epitaxial growth of highly luminescent CdSe/CdS core/shell nanocrystals with photostability and electronic accessibility," *Journal of the American Chemical Society*, vol. 119, no. 30, pp. 7019–7029, 1997.
- [226] W. U. Huynh, "Hybrid Nanorod-Polymer Solar Cells," *Science*, vol. 295, no. 5564, pp. 2425–2427, Mar. 2002.
- [227] X. Blase, A. Rubio, S. G. Louie, and M. L. Cohen, "Stability and band gap constancy of boron nitride nanotubes," *EPL (Europhysics Letters)*, vol. 28, no. 5, p. 335, 2007.
- [228] L. Carbone, C. Nobile, M. De Giorgi, F. D. Sala, G. Morello, P. Pompa, M. Hytch, E. Snoeck, A. Fiore, I. R. Franchini, M. Nadasan, A. F. Silvestre, L. Chiodo, S. Kudera, R. Cingolani, R. Krahne, and L. Manna, "Synthesis and Micrometer-Scale Assembly of Colloidal CdSe/CdS Nanorods Prepared by a Seeded Growth Approach," *Nano Letters*, vol. 7, no. 10, pp. 2942–2950, Oct. 2007.
- [229] D. V. Talapin, J. H. Nelson, E. V. Shevchenko, S. Aloni, B. Sadtler, and A. P. Alivisatos, "Seeded Growth of Highly Luminescent CdSe/CdS Nanoheterostructures with Rod and Tetrapod Morphologies," *Nano Letters*, vol. 7, no. 10, pp. 2951–2959, Oct. 2007.
- [230] Delia J. Milliron, Steven M. Hughes, Yi Cui, Liberato Manna, Jingbo Li, Lin-Wang Wang, and A. Paul Alivisatos, "Colloidal Nanocrystal heterostructures with linear and branched topology," *Nature*, vol. 430, no. 6996, pp. 190–195, Jul. 2004.
- [231] X. Li, J. Lian, M. Lin, and Y. Chan, "Light-Induced Selective Deposition of Metals on Gold-Tipped CdSe-Seeded CdS Nanorods," *Journal of the American Chemical Society*, vol. 133, no. 4, pp. 672–675, Feb. 2011.
- [232] Gabi Menagen, Janet E. Macdonald, Yossi Shemesh, Inna Popov, and Uri Banin, "Au Growth on Semiconductor Nanorods: Photoinduced versus Thermal Growth Mechanisms," *JACS.*, vol. 131, no. 47, pp. 17406–17411, 2009.
- [233] A. E. Saunders, I. Popov, and U. Banin, "Synthesis of Hybrid CdS–Au Colloidal Nanostructures," *The Journal of Physical Chemistry B*, vol. 110, no. 50, pp. 25421–25429, Dec. 2006.
- [234] Sabyasachi Chakraborty, Guichuan Xing, Yang Xu, Song Wee Ngiam, Nimai Mishra, Tze Chien Sum, Yinthai Chan, Guichuan Xing, Yang Xu, Song Wee Ngiam, Nimai Mishra, Tze Chien Sum, and Yinthai Chan, "Engineering Fluorescence in Au-Tipped, CdSe-Seeded CdS Nanoheterostructures," *Small*, vol. 7, pp. 2847–2852, 2011.

- [235] Ou Chen, Xian Chen, Yongan Yang, Jared Lynch, Huimeng Wu, Jiaqi Zhuang, and Y Charles Cao, "Synthesis of Metal–Selenide Nanocrystals Using Selenium Dioxide as the Selenium Precursor," *Angew. Chem. Int. Ed.*, vol. 120, no. 45, pp. 8766–8769, Oct. 2008.
- [236] J. Huang, M. V. Kovalenko, and D. V. Talapin, "Alkyl Chains of Surface Ligands Affect Polytypism of CdSe Nanocrystals and Play an Important Role in the Synthesis of Anisotropic Nanoheterostructures," *Journal of the American Chemical Society*, vol. 132, no. 45, pp. 15866–15868, Nov. 2010.
- [237] D. V. Talapin, R. Koeppel, S. Götzinger, A. Kornowski, J. M. Lupton, A. L. Rogach, O. Benson, J. Feldmann, and H. Weller, "Highly Emissive Colloidal CdSe/CdS Heterostructures of Mixed Dimensionality," *Nano Letters*, vol. 3, no. 12, pp. 1677–1681, Dec. 2003.
- [238] J. J. Shiang, A. V. Kadavanich, R. K. Grubbs, and A. P. Alivisatos, "Symmetry of annealed wurtzite CdSe nanocrystals: assignment to the C<sub>3v</sub> point group," *The Journal of Physical Chemistry*, vol. 99, no. 48, pp. 17417–17422, 1995.
- [239] B. K. Min, A. R. Alemozafar, M. M. Biener, J. Biener, and C. M. Friend, "Reaction of Au(111) with Sulfur and Oxygen: Scanning Tunneling Microscopic Study," *Topics in Catalysis*, vol. 36, no. 1–4, pp. 77–90, Aug. 2005.
- [240] J. C. Brice, *The Growth of Crystals from Liquids*. North-Holland Pub. Co.: Amsterdam, 1973.
- [241] G. Bastard, "Superlattice band structure in the envelope-function approximation," *Physical Review B*, vol. 24, no. 10, p. 5693, 1981.